# Surface Morphology of Epitaxially Grown 2D Van der Waals Heterostructures

James Wrigley

Thesis submitted to the University of Nottingham for the degree of Doctor of Philosophy

March 2022

# Abstract

The incorporation of few-layer Van der Waals structures into optical and electronic devices has been of considerable interest to the production of microelectronic devices. In this thesis the epitaxial growth of hexagonal boron nitride (hBN) and graphene, on graphite and hBN substrates respectively, was investigated with molecular beam epitaxy. In the first experimental section the morphologies of hBN depositions on highly-oriented pyrolytic graphite (HOPG) were analysed with atomic force microscopy (AFM). The thicknesses and shapes of deposited domains were found to depend upon the growth temperature and deposition time, with an optimally identified temperature for the minimising of BN aggregates at 1390$^{o}$C. Additionally, the preferred growth edges of the forming hBN domains were found to transition between zigzag and armchair with increased substrate growth temperatures from 1080$^{O}$C to 1390$^{O}$C.

Graphene material, deposited onto hBN flakes on sapphire substrates using a new carbon source that sublimates the precursor material through e-beam heating, was compared with similar material produced with other carbon sources. AFM imaging of the graphene revealed strained graphene domains formed during growth, identified by hexagonal moiré patterns with periods greater than 13.9 nm. Large graphene terraces on the order of several microns were found to have formed largely free of free-standing aggregates. Raman spectroscopy of the graphene formed on the hBN flakes shows that aggregates accumulated around the edges of the graphene terraces exhibit spectra consistent with a graphitic, as opposed to amorphous, composition. The e-beam source was found to reliably deposit complete graphene monolayers, and this source has been preferred for future study.

Lateral heterostructures of graphene and hBN deposited via successive depositions of carbon and boron/nitrogen, were analysed with AFM. The similarities of the two lattices have been described as allowing for the formation of connected domains with minimal defect formation along the heterojunction. All deposited material not accumulated into aggregates was found to have nucleated

from the edges of domains formed from the previous growth cycle. No aggregate formation was found to have occurred atop the lateral heterojunctions, implying minimal defect formation and dangling bonds at the interface. Future studies of these heterostructures may consider the formation of these heterostructures on other insulating substrates to allow for investigation of optical properties.

Finally, the formation of CA.M/PTCDI heterostructures deposited onto HOPG and hBN/HOPG was investigated. The integration of organic molecular networks into van der Waals heterostructures could potentially provide a means to form complex devices simply and cheaply with nanometre thicknesses. Needle-like PTCDI islands were found to be orientationally templated by the presence of an adjacent CA.M layer, with some PTCDI islands lying atop the CA.M layer and some lying directly upon the substrate. The CA.M layer was also observed to be necessary for the formation of organised PTCDI islands on the hBN/HOPG substrate, allowing for the formation of the needle-like islands on the partial hBN monolayers. Photoluminescence spectroscopy of the deposited samples identified a reduction in the HOPG-induced quenching for the PTCDI separated from the HOPG by the hBN monolayer. The observed 0-0 fluorescence peaks of the PTCDI were positioned at 2.212 eV, consistent with that obtained for PTCDI islands deposited onto hBN substrates. Increasing the thickness of the hBN spacer layer might be expected to allow for tuning the quenching of the PTCDI fluorescence spectrum.

# Acknowledgements

Firstly, I would like to thank my supervisor, Professor Peter Beton. It was his support and patience that saw me through, even with the unforeseen events that arose during this period. I will look back on these years with fondness. I would also like to thank those others that took the time to teach me on instrumentation and who otherwise provided their insight, particularly Dr Vladimir Korolkov, Dr James Kerfoot, Dr Juan Diez Albar, Dr James Thomas, and Dr Alex Summerfield.

I would also like to thank the researchers associated with the MBE systems for producing the samples I investigated, providing their insight, and putting up with the many AFM images I provided in return. Specifically, I would like to thank, Tin Cheng, Professor Sergei Novikov, Professor Christopher Mellor, Professor Tom Foxon, Professor Laurence Eaves, and Professor Andrei Khlobystov. I would also like to thank Dr Graham Rance at the Nanoscale and Microscale Research Centre for his support and assistance. I would also like to thank the technical staff at the School of Physics and Astronomy, and the EPSRC for funding my PhD.

I would like to thank Tyler James, Dr Jonathan Bradford, Dr Manal Alkhamisi, and Dr Abigail Bellamy-Carter for making my time at the university both more enjoyable and more productive.

I would like to thank my parents, Jane and David Wrigley, for their continued support and company through the years. Finally, I would like to thank my partner and friend, Dr Emily Tyler, for her continued support, and for getting me through the tougher times. My best wishes to all I have mentioned, and good luck on your future endeavours.

# Contents

# 1. Introduction

### 1. Introduction

In this Chapter the aims of the thesis are presented with regard to current research in the areas of surface science and molecular electronics on van der Waals heterostructures. Following this will be an overview of the studies carried out as part of this thesis and the ordering of the material.

### 1.1 Overview

In recent years there have been significant advances made in the fields of micro-electronics as a result of the integration of 2D materials into devices. The incorporation of van der Waals crystals into electronics and optoelectronics have paved the way for developments in micro-scale devices with unique properties. Van der Waals materials exhibit a variety of electrical and optical properties and layered structures, and combining these materials opens the possibility for generating novel devices with monolayer thicknesses.

Scalable production of these materials has been developed with the fabrication of graphene via chemical vapour deposition and SiC decomposition, or hexagonal boron nitride with CVD. These processes exhibit strengths conducive to the formation of large-scale devices with controllable characteristics. CVD synthesis of graphene and hBN have been developed in recent years to the point where large domains of relatively defect-free monolayers can be produced and transfer from catalytic substrates has been refined or avoided by direct growth on insulating substrates [1–3]. Research into appropriate precursors and substrate selection have resulted in the reliable production of material ready for integration into devices and heterostructures for the purposes of microelectronics, optoelectronics, and others [4–6].

Molecular beam epitaxy, a vacuum technique with the advantages of highly controllable deposition rates and minimal contamination, has until recently garnered comparably less attention for the formation of these materials. Developments in the production of graphene and hexagonal boron nitride (hBN) with molecular beam epitaxy (MBE) have been slower than those of CVD. In the case of hBN low substrate temperatures resulted in small grain sizes and rough surfaces, such as those generated by Tsai et al. in 2009 [7,8]. Direct graphene production on insulating substrates showed a strong temperature dependence on the quality of the resulting material, while metallic substrates performed better, though necessitating transfer to form device structures [9–11].

More recently, advances in the epitaxial production of these materials have been achieved by increasing the substrate temperatures above 1000°C during growth. This high-temperature molecular beam epitaxy (HT-MBE) has begun an exploration of the potential for clean monolayer production and optical properties on insulating substrates [12–15].

This thesis aims to advance the progress made in the growth of graphene and hBN by high-temperature molecular beam epitaxy, as previously demonstrated by the Nottingham group, including Albar, Summerfield, and Davies, among others [12–16]. These studies established the production of graphene and hBN with high-temperature MBE, with the identification of high-quality, large domains, on insulating substrates, a feat not previously achieved in MBE. In this work the development of these material depositions by consideration of the surface morphology and the importance of epitaxial variables during growth is furthered.

AFM is well established as a process for analysis of the morphology of surfaces at the nanoscale. AFM provides the means to identify features ranging from atomic lattices on the order of angstroms up to protrusions or indentations microns in scale. Additionally, alternating the use of conductive and tapping-modes of operations can provide information on the material composition, resistivity, and other local physical properties of a surface. AFM is widely applied to the surfaces investigated here, and the results from this imaging drive much of the presented studies.

Integration of photo-active molecules into mono- or few-layer heterostructures provides for many potential applications in the fields of micro-photonics and the formation of novel van der Waals-organic devices. Templating optically-active molecules with substrates of comparable symmetry and neighbouring molecular networks can provide the means to control the optical properties of a surface on a macro-scale [17]. In this thesis the separation of luminescent PTCDI molecules from a conductive substrate with the insulating layers of other materials is investigated. This poses the possibility for the tuning of the optical properties of molecules such as PTCDI to facilitate the production of light-emitting diodes among other potential applications. Alongside AFM for the identification of the morphology of deposited molecular structures, photoluminescent spectroscopy has been applied to study the luminescence of the materials.

### 1.2 Overview of the Thesis

The next Chapter presents a collation of background information relevant to the studies carried out in the thesis. The Chapter briefly discusses the properties of graphene and hBN that make them interesting materials for the production of thin electronic devices and the similarities of the two lattices. This is followed by a discussion of the current progress made in the reliable production of graphene and hBN with a variety of growth techniques, including molecular beam epitaxy (MBE), chemical vapour deposition (CVD), and exfoliation. Finally, the Chapter describes the necessary conditions for the formation of supramolecular networks and the reasons for the selection of cyanuric acid-melamine (CA.M) in the later studies.

In Chapter 3 the experimental techniques relevant to the studies in this thesis are presented. The techniques, including atomic force microscopy (AFM), Raman spectroscopy, and fluorescence spectroscopy, are described alongside the necessary physical concepts. The systems and processes necessary for sample preparation are also described, namely exfoliation, vacuum sublimation, and immersion deposition, for the relevant materials.

In Chapter 4 the surface morphology of MBE-grown hBN on HOPG substrates is analysed. The surface features of the samples are compared across multiple substrate temperatures and growth times and AFM data from these observations is presented. The shapes and prevalence of hBN domains are compared when nucleated from graphite steps of differing heights. Finally, the impact of aggregates on the growth of monolayer hBN is discussed.

Graphene sheets grown by MBE on hBN flakes are analysed in Chapter 5. Samples of these G/hBN samples produced with a new MBE carbon source using an e-beam to heat the source material were analysed with AFM and Raman spectroscopy to identify the quality of the graphene sheets. The source for the MBE were investigated to identify a reliable source capable of producing graphene sheets as part of lateral heterostructure studies described in the following Chapter.

In Chapter 6 observations are presented from successive epitaxial depositions of hBN and graphene onto HOPG substrates. The morphology of the resulting monolayers and the heterojunctions is analysed by AFM. The edges of the material domains are considered relative to the lattices, alongside the prevalence of defects and aggregate material.

Finally, Chapter 7 presents observations from the deposition of CA.M and PTCDI supramolecular networks on the surface of graphite and hBN/graphite substrates, with the latter having been produced as was analysed in Chapter 4. The morphology of the molecular monolayers on these varied substrates are compared and the impact on the photoluminescent spectrum of the PTCDI is analysed.

# Chapter 2: Background

### 2. Overview

In this thesis research into a range of topics on the growth of two-dimensional materials and the formation of supramolecular monolayers will be presented. Surfaces of several distinct heterostructures of graphene and hBN were analysed, with consideration paid to the impact of changing growth parameters on the resulting morphologies. In addition, an investigation of cyanuric acid – melamine lattices (CA.M) deposited onto hBN flakes was carried out to analyse supramolecular lattice growth on hexagonal 2D crystals. Before these analyses are discussed a review will be presented of the results of previous studies on the properties and growth of hBN, graphene, and CA.M. Previous studies on the production of thin van der Waals monolayers or few-layer crystals are presented to place this thesis in context.

Section 2.1 describes the properties of graphene and hBN monolayers. The properties of lateral and vertical heterostructures of hBN and graphene are presented in 2.1.3 and 2.1.4 respectively. Periodic heterostructures of hBN and graphene are discussed in 2.1.5. Section 2.2 is a review of studies on the production of few-layer hBN and graphene, presenting the CVD, MBE, SiC decomposition, and bulk exfoliation methods. Finally, supramolecular assembly of molecules is discussed, focusing on prior studies in the application of the CA.M network to van der Waals crystals, in Section 2.3.

### 2.1 Properties of Graphene, hBN, and their Heterostructures

Graphene and hBN lattices exhibit some structural similarities, yet the electronic and mechanical properties of the two materials are distinct. Graphene and hBN share a hexagonal structure with lattice constants of 2.46 Å and 2.504 Å respectively. However, the symmetries of the graphene lattice result in a near-zero bandgap, whereas the diatomic nature of the hBN crystal produces a large bandgap of ~6 eV [18,19]. Bringing monolayers of the two materials vertically into contact with minimal misalignment generates a moiré superlattice which impacts the electronic properties of the resulting material.

In this Section the distinct properties of the two materials are discussed in more detail. The properties of heterostructures comprising lateral and vertical junctions of graphene and hBN are described, and the potential uses and difficulties in production are noted.

### 2.1.1 Properties of graphene

Graphene is a 2D allotrope of carbon, evoking interest in the scientific world for its linear band dispersion near the K point of the Brillouin zone and its semi-metallic nature. The isolation of single graphene sheets was originally considered a physical impossibility, and graphene was first modelled by Wallace (1947) to approximate the behaviour of the graphite surface [20]. Isolated in 2004 by Novoselov and Geim, single monolayers of graphene were produced with the 'scotch tape' exfoliation method [21].

In graphene the hexagonal rings within the layer consist of carbon atoms bonded by hybridised $sp^2$ orbitals, with the interlayer interaction arising from the much weaker van der Waals forces. The $sp^2$ orbitals originate from the ground state electronic configuration of carbon $1s^2 2s^2 2p^2$, which is four electrons short of a closed shell. The s and p orbitals of the highest energy states do not exhibit the symmetry required for the formation of the observed trisymmetric network. To form the hexagon one s orbital electron is elevated, leading to the $1s^2 2s^1 2p^3$ configuration on each carbon atom. The lone s orbital and two of the 2p orbitals hybridise to form three $sp^2$ orbitals, leaving a single unhybridized p orbital. The three $sp^2$ orbitals combine to form the monolayer hexagonal network, with the out of plane p orbital overlapping with the equivalent orbitals of neighbouring carbon atoms to form pi bonds. The extended network of pi bonds results in the high electrical conductivity of graphene, and simultaneously contributes to the formation of the van der Waals crystal as a result of the high polarizability of pi orbitals.

As a honeycomb lattice the unit cell of a graphene monolayer consists of two atoms, with the crystal described by two triangular sublattices offset from each other by the bond length of 1.42 Å. The sublattices as constituents of the complete monolayer lattice are depicted in Figure 2.1 a). The sites of each sublattice, commonly denoted A and B, are all occupied by carbon atoms. When the sublattices are electronically similar, as in the case of freestanding graphene, the material exhibits no bandgap. This similarity can be broken, such as by the presence of a substrate, resulting in a bandgap [22]. The moiré superlattice generated by the overlap of graphene and hexagonal boron nitride is expected to generate a bandgap in this way [23].

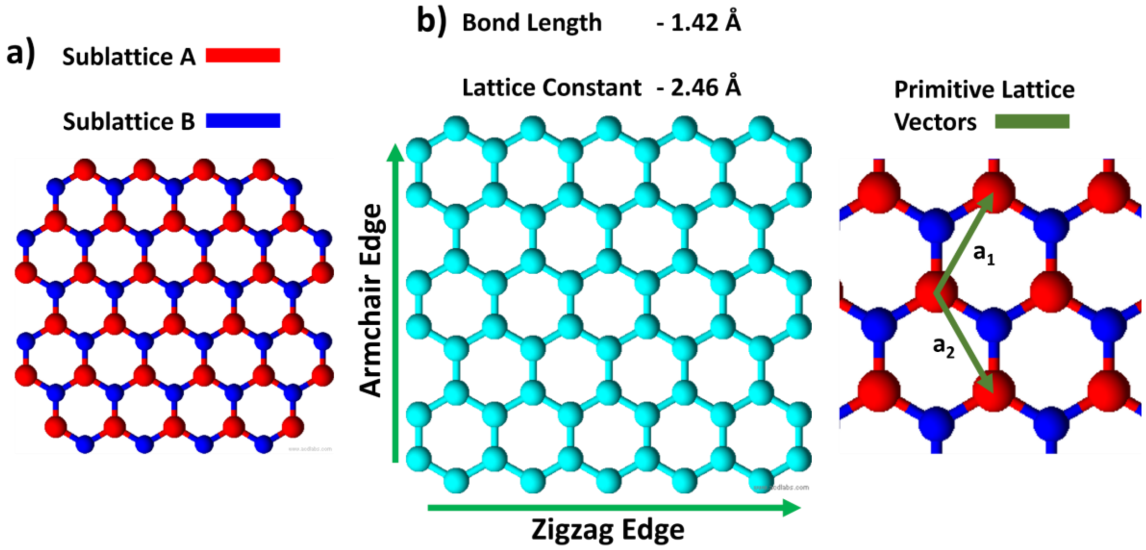

Figure 2.1 – Atomic models of graphene are presented. In a) the two inequivalent sublattices of graphene are highlighted in blue and red. In b) the lattice is depicted with one carbon atom occupying each lattice site, depicting the highly symmetric nature of the graphene lattice. The direction of the armchair and zigzag edges are designated by the green arrows, though note that the other zigzag and armchair directions are obtained by rotations of these arrows by integer multiples of 60°. Finally, on the right the primitive lattice vectors of graphene are depicted, with lengths equal to the lattice constant. Note, that the two sublattices are offset by 1.42 Å and cannot be transformed between with the use of the primitive lattice vectors.

Due to the highly symmetric nature of the graphene lattice, graphene islands will tend to form either a hexagonal or dodecagonal shape [24]. These two shapes originate from the hexagonal nature of the lattice, with the island edges consisting of either or both of the armchair or zigzag directions of the lattice, such as is shown in Figure 2.1 b). Zigzag and armchair edges are common to all hexagonal lattices are commonly abbreviated to Z and A for simplicity. Armchair (zigzag) edges occur at every $60^o$ rotation from any other armchair (zigzag) edge and are oriented $30^o$ from any zigzag (armchair) edges. The armchair edge consists of an equal number of sites from the A and B sublattices, which can be seen in Figure 2.1 a), whereas the sites of the zigzag edge lie on entirely one sublattice or the other. Hence, for a hexagonal island to form there must exist a growth preference for either the armchair or zigzag edges. The dodecagonal islands form when there is equality in the growth rates of the two distinct edges.

Having established the structural properties of the graphene lattice the band structure of the material can be derived. A derivation of the band structure was first constructed by Wallace in 1947 using the tight binding approximation as a preliminary step in establishing the band structure of bulk graphite [20]. This approximation allows for the calculation of the electronic band structure by approximating the atomic wavefunction of an atom within the crystal as a superposition of the atomic wavefunctions for isolated atoms.

As graphene has two atoms in its unit cell the wavefunction must be represented as a linear combination of two wavefunctions, labelled $\mathrm{u}_{\mathrm{A}}(\boldsymbol{k}, \boldsymbol{r})$ and $\mathrm{u}_{\mathrm{B}}(\boldsymbol{k}, \boldsymbol{r})$, which correspond to the sublattices A and B. The resulting wavefunction is as follows, where the contribution of each sublattice is considered with the $A(\boldsymbol{k})$ and $B(\boldsymbol{k})$ coefficients,

$$\psi_k(\boldsymbol{r}) = A(\boldsymbol{k})u_A(\boldsymbol{k},\boldsymbol{r}) + B(\boldsymbol{k})u_B(\boldsymbol{k},\boldsymbol{r}) \tag{2.1}$$

The wavefunctions, $\mathrm{u}_{\mathrm{A}}(\boldsymbol{k}, \boldsymbol{r})$ and $\mathrm{u}_{\mathrm{B}}(\boldsymbol{k}, \boldsymbol{r})$, are in turn composed of the superposition of atomic wavefunctions $\varphi_A$ and $\varphi_B$, centred on the atoms belonging to sublattices A and B, respectively. These can be written as,

$$u_A(\boldsymbol{k},\boldsymbol{r}) = \frac{1}{\sqrt{N}}\sum_{i=1}^{N} e^{i\boldsymbol{k}\boldsymbol{R}_i}\,\varphi_A(\boldsymbol{r} - \boldsymbol{R}_i) \tag{2.2}$$

$$u_B(\boldsymbol{k},\boldsymbol{r}) = \frac{1}{\sqrt{N}}\sum_{i=1}^{N} e^{i\boldsymbol{k}(\boldsymbol{R}_i+\boldsymbol{\delta})}\,\varphi_B(\boldsymbol{r} - \boldsymbol{R_i} - \boldsymbol{\delta}) \tag{2.3}$$

Where δ is $(\frac{a_G}{\sqrt{3}}, 0)$, the displacement between two carbon atoms in the unit cell, and N is the total number of unit cells. An expression for the expectation value of the energy, $E(\boldsymbol{k})$, can be obtained by combining the above equations with the following,

$$E(\boldsymbol{k}) = \int \psi_k^* \widehat{H}\, \psi_k \, d\boldsymbol{r} \tag{2.4}$$

And as a result we obtain,

$$E(\boldsymbol{k}) = \frac{1}{N}\sum_{i,j=1}^{N,N} e^{i\boldsymbol{k}(\boldsymbol{R}_i - \boldsymbol{R}_j)} \int \left(A^*\varphi_{Aj}^* + B^* e^{-i\boldsymbol{k}\boldsymbol{\delta}}\varphi_{Bj}^*\right) \widehat{H}\left(A\varphi_{Aj} + Be^{-i\boldsymbol{k}\boldsymbol{\delta}}\varphi_{Bj}\right) d\boldsymbol{r} \tag{2.5}$$

Where $\varphi_{Ai} = \varphi_A(\boldsymbol{r} - \boldsymbol{R}_i)$ and $\varphi_{Bi} = \varphi_B(\boldsymbol{r} - \boldsymbol{R}_i + \boldsymbol{\delta})$ and similar expression can be written for index j. The expression can be simplified by considering an infinite plane of unit cells and making this change of variables, $\boldsymbol{\rho_j} = \boldsymbol{R_j} - \boldsymbol{R_i}$. The resulting expression can be written as a matrix,

$$E(\boldsymbol{k}) = [A^*(\boldsymbol{k}), B^*(\boldsymbol{k})]\begin{bmatrix} H_{AA} & H_{AB} \\ H_{BA} & H_{BB} \end{bmatrix}\begin{bmatrix} A(\boldsymbol{k}) \\ B(\boldsymbol{k}) \end{bmatrix} \tag{2.6}$$

Where the on-diagonal terms are,

$$H_{AA} = \sum_{j=1}^{N} e^{-i\boldsymbol{k}\boldsymbol{\rho}_j} \int \varphi_A^*(\boldsymbol{r} - \boldsymbol{\rho_j})\, \widehat{H}\, \varphi_A(\boldsymbol{r})\, d\boldsymbol{r} \tag{2.7}$$

And similarly for B. By considering only nearest neighbours the terms, $\boldsymbol{\rho_j} = 0$, which simplifies the on-diagonal terms to,

$$H_{AA} = \int \varphi_A^*(\boldsymbol{r})\, \widehat{H}\, \varphi_A(\boldsymbol{r})\, d\boldsymbol{r} \tag{2.8}$$

The Hamiltonian, $\widehat{H}$, can be represented as a sum of the Hamiltonian from the single atom and a perturbation from the nearest neighbours. This leads to,

$$H_{AA} = \int \varphi_A^*(\boldsymbol{r})\, \widehat{H}_{atomic}\, \varphi_A(\boldsymbol{r})\, d\boldsymbol{r} + \int \varphi_A^*(\boldsymbol{r})\, \Delta V\, \varphi_A(\boldsymbol{r})\, d\boldsymbol{r} \tag{2.9}$$

$$H_{AA} = H_{BB} = E_{pz} + \alpha = E_0 \tag{2.10}$$

Where $E_{pz}$ is the energy of an electron in the 2pz state and the result of the perturbation, α, is symmetric for sites A and B. For the off-diagonal terms the contributions one can write,

$$H_{AB} = \sum_{n.n} e^{-i\boldsymbol{k}(\boldsymbol{\rho_j} - \boldsymbol{\delta})} \int \varphi_A^*(\boldsymbol{r} - \boldsymbol{\rho_j})\, \widehat{H}\, \varphi_B(\boldsymbol{r} - \boldsymbol{\delta})\, d\boldsymbol{r} \tag{2.11}$$

Which becomes the following by noting that the atomic contribution equals zero in this case,

$$= f(\boldsymbol{k}) \int \varphi_A^*(\boldsymbol{r})\, \Delta V\, \varphi_B(\boldsymbol{r} - \boldsymbol{\delta})\, d\boldsymbol{r} = -f(\boldsymbol{k})t \tag{2.12}$$

In which t is the nearest-neighbour hopping energy, With knowledge of the nearest neighbours one can expand the summation and calculate $f(\boldsymbol{k})$. The result of this expansion is displayed in Figure 2.2

$$f(k) = \sum_{n.n} e^{-ik(\rho_j - \delta)} = \underbrace{e^{\frac{ik_x a_G}{\sqrt{3}}}}_{1} + \underbrace{e^{-i\left(\frac{k_x a_G}{2\sqrt{3}} + \frac{k_y a_G}{2}\right)}}_{2} + \underbrace{e^{-i\left(\frac{k_x a_G}{2\sqrt{3}} - \frac{k_y a_G}{2}\right)}}_{3}$$

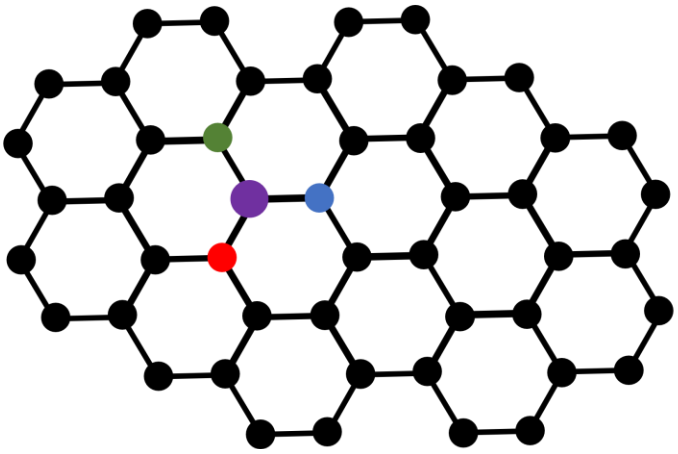

Figure 2.2 – A diagram showing the expansion of the summation that makes up the f(k) function. Each term corresponds to one neighbour of an arbitrary atom in the lattice, here coloured in purple.

where $a_G$ is the modulus of the unit cell vector. The matrix element $H_{BA}$ can be written similarly as,

$$H_{BA} = -t\, f(\boldsymbol{k})^* = H_{AB}^* \tag{2.13}$$

As a result, the Hamiltonian matrix can be simply written as,

$$H = \begin{bmatrix} E_0 & -t\,f(\boldsymbol{k}) \\ -t\,f(\boldsymbol{k})^* & E_0 \end{bmatrix} \tag{2.14}$$

For which the eigenvalues are,

$$E = E_0 \pm t\sqrt{f(\boldsymbol{k})^* f(\boldsymbol{k})} \tag{2.15}$$

By setting $E_0$ as the reference energy and substituting in the equation for $f(\boldsymbol{k})$ an expression for $E(\boldsymbol{k})$ can be obtained,

$$E(\boldsymbol{k}) = \pm t\sqrt{1 + 4\cos\left(\frac{\sqrt{3}k_x a_G}{2}\right)\cos\left(\frac{k_y a_G}{2}\right) + 4\cos^2\left(\frac{k_y a_G}{2}\right)} \tag{2.16}$$

At positions, k, where the expression within the square root is zero, the bandgap is zero. The conditions for this are,

$$\frac{\sqrt{3}k_x a_G}{2} = 2n\pi \text{ and } \cos\left(\frac{k_y a_G}{2}\right) = -\frac{1}{2} \tag{2.17}$$

Or,

$$\frac{\sqrt{3}k_x a_G}{2} = (2n+1)\pi \text{ and } \cos\left(\frac{k_y a_G}{2}\right) = \frac{1}{2} \tag{2.18}$$

Where n is an integer from 0, 1, 2… Some of the solutions to these conditions lie beyond the boundary of the Brillouin zone. However, n = 0 for the second condition, results in positions lying on the corners of the hexagonal zone, occupying the high symmetry $\boldsymbol{K}$ sites. Small changes of $\boldsymbol{k}$ around the $\boldsymbol{K}$ points can be considered by changing the variable $\boldsymbol{k}$ to $\boldsymbol{q} = \boldsymbol{k} - \boldsymbol{K}$ and carrying out a Taylor expansion on $f(\boldsymbol{k})$. The result can be approximated to,

$$f_k(\boldsymbol{q}) \approx \frac{\sqrt{3}a_G}{2}\left(iq_x - q_y\right) \text{ and } f_{K'}(\boldsymbol{q}) \approx \frac{\sqrt{3}a_G}{2}\left(iq_x + q_y\right) \tag{2.19}$$

As such, the eigenenergies around the K and K' points are,

$$E = \pm\frac{\sqrt{3}ta_G}{2}q = \pm\hbar q v_F \tag{2.20}$$

As can be observed the energy dispersion near the K and K' points is linear. This linearity results in the charge carriers behaving as massless Dirac fermions with velocities equal to $v_F$, which is on the order of $10^6$ m/s. The positions of the band structure where the dispersion is linear have been dubbed Dirac cones and the presence of these linear regions leads to many of the unique properties associated with graphene. The $\pm$ sign in the eigenenergy approximation shows that these Dirac cones appear in the conduction and valence band, with the cones meeting at the Fermi level.

A significant limitation of graphene from the perspective of 2D electronics is the lack of bandgap, which results in low on/off ratio transistors incompatible with digital function. There are several proposed methods for the introduction of the bandgap, one of which is the confinement of the graphene in one dimension. Graphene nanoribbons then, consisting of monolayers of graphene extending unconstrained in only one dimension, provide a potentially simple and tuneable method for the introduction of a bandgap. In addition to this, the small width of the structure results in a greater significance for edge states of the ribbon, which have an influence on electric and magnetic properties.

Tight binding calculations have shown that the band structure of graphene nanoribbons (GNRs) depends upon the width of the ribbon and the nature of the edge [25,26]. Zigzag ribbons, those where the entire length of both edges follows the zigzag direction, are always metallic. Armchair ribbons exhibit metallic or semiconducting band structure dependent upon the ribbon width. Specifically, armchair ribbons exhibit metallic band structures when the number of lines of carbon atoms, taken along the armchair direction and with a complete hexagon crossing three lines, is equal to 3M – 1 for integer, M [27]. For a number of carbon lines not equal to 3M – 1 a bandgap is opened up in the armchair ribbon compared to unconstrained graphene. Additionally, the scale of the band gap is also dependent upon the width of the ribbon, with greater energy gaps seen in thinner ribbons.

The band structure of the zigzag ribbon is flat at zero energy [25]. The zero energy dispersion, dE/dk, about this point results in a predicted perfect conducting channel in the presence of impurities [28].

As a result, zigzag ribbons and chiral ribbons with perfect edges are expected to exhibit excellent transport properties. Chiral ribbons are those consisting of both zigzag and armchair regions along the length of the ribbon. Zigzag ribbons are also distinct from armchair ribbons by the expression of magnetic ordering, such as a paramagnetic response at room temperature [29].

Various methodologies for the production of graphene nanoribbons with fine width control have been investigated, with considerable interest for those by which nanometre scales can be achieved. Lithographic approaches making use of scanning tunnelling microscopes (STM), atomic force microscopes (AFM), or transmission electron microscopes (TEM) have been reported to produce ribbons with widths of ~ 10 nm for AFM and STM, and widths down to 0.7 nm with TEM [30–32]. Though relatively high precision of scale is achievable with these devices, they remain indefinitely restricted in practice by the lack of scalability inherent in the process.

Other processes that produce nanoribbons by the reduction of graphene sheets or nanotubes include the etching of the sheets with catalytic particles, or the unzipping of nanotubes via chemical agents [33–35]. These are limited in precision by the scale of the precursor material, the nanotube diameter in the unzipping process, or the size of the metallic nanoparticles necessary for catalytic etching [36].

Bottom-up approaches to graphene nanoribbon production have also been explored. Chemical vapour deposition (CVD) has proven to be effective for the generation of nanoribbons with scales down to ~20 nm on $SiO_2$/Si substrates [37,38]. This is achieved by the fabrication of Ni templates on the substrate, which are then exposed to ethylene at high temperatures to seed the growth of the graphene. The structure of the resulting nanoribbon is then dictated by the Ni template from which it has grown and on which it resides. It has been noted by Celis et al. that further application of these graphene nanoribbon requires transfer to an insulating substrate [36].

### 2.1.2 Properties of hBN and the Growth of the 2D Monolayer

Hexagonal boron nitride (hBN) is an insulating van der Waals crystal isomorphic to graphene. The hexagonal lattice consists of alternating B and N atoms bonded with hybridized $sp^2$ orbitals. Despite the similarities in the in-plane bonding of the hBN and G lattices, hBN is an insulator with a bandgap of ~6 eV [18,39]. This bandgap differences between graphene and hBN arise from the differences in $p_z$ orbital filling between the two crystals. In graphene the $p_z$ orbitals are half-filled. In hBN the $p_z$ orbitals are filled on B and empty on N atoms, due to the energy differences between the two sites.

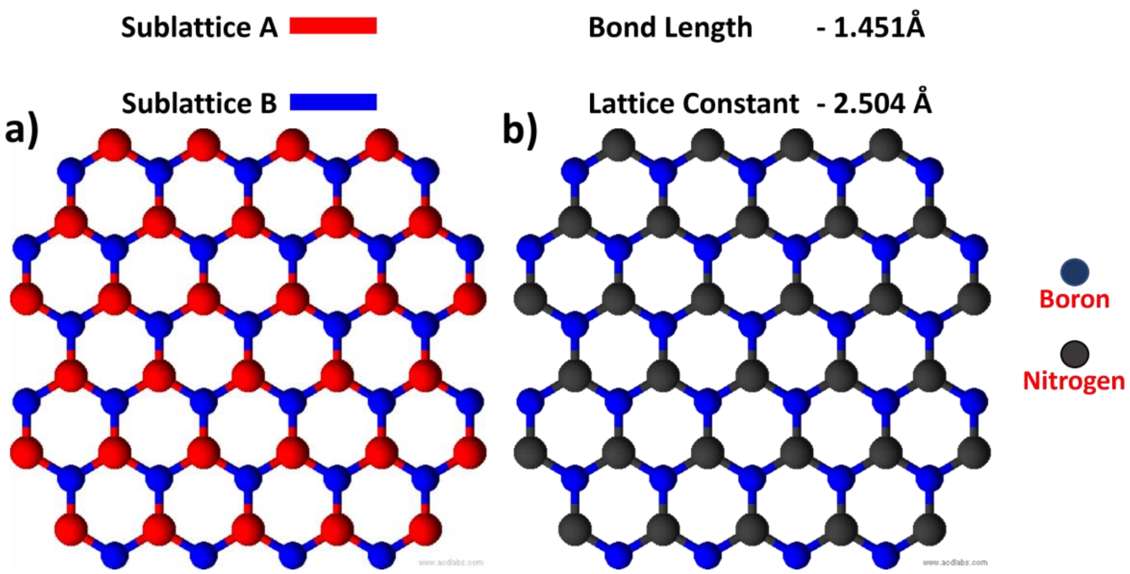

Figure 2.3 – Atomic models of a monolayer of hexagonal boron nitride (hBN). In a) the two sublattices of the hBN are presented in red and blue, respectively. hBN is a diatomic crystal with each sublattice occupied by one of the two elements, boron or nitrogen. This can be confirmed by comparing the sublattice model in a) with the model in b) which depicts the lattice with the lattice positions occupied. The bond length of hBN, and thus the lattice constant, are comparable with graphene, differing by only 1.8%.

The melting point of hexagonal boron nitride is greater than 2900°C in $N_2$, with a decomposition temperature of up to 1000°C in air [40]. In addition to these properties, the large bandgap and inert nature of hBN make it excellent for encapsulating van der Waals heterostructures, preventing degradation and contamination while preserving the optical and electronic properties of the device

[41]. hBN also makes a good substrate for 2D materials due to the lack of dangling bonds and charge impurities. A small lattice mismatch of only 1.8% exists between hBN and graphene, with the lattice constant of hBN being the larger of the two[42]. In general, similar lattice constants allow one material to template the initial growth of a second [43]. Dean et al. (2010) showed that a hBN substrate can improve the carrier mobility of graphene versus other substrates, and graphene/hBN devices have been produced exhibiting density-independent carrier mobilities of 80,000 $cm^2 V^{-1} s^{-1}$, three times greater than that for graphene on $Si/SiO_2$ substrates [44,45].

The electronic bandgap of hBN was established only recently as being of indirect nature, at about 5.95eV [19]. The relatively high quantum efficiency has previously led to misidentification as a direct bandgap, such as by Watanabe and Taniguchi in 2004 [18]. In 2016 Cassabois, in the paper 'Hexagonal Boron Nitride is an Indirect Bandgap Semiconductor', established the basis of the current understanding [19]. There is still some disagreement over the exact bandgap, but recent theoretical and experimental studies have identified a shift towards a direct transition in the monolayer material [39,46].

The large bandgap of hBN and strong covalent bonds result in the observed chemical inertness and high stability of the bulk to monolayer material. As a result, hBN has been explored as an encapsulating layer to reduce deterioration of devices involving more chemically active 2D materials [47,48]. Graphene tends to adsorb organic contaminants when exposed to air, black phosphorus deteriorates rapidly when exposed to atmosphere [49]. Examples of hBN encapsulation of both materials show the potential for stabilisation of 2D devices that would otherwise prove impractical.

The large optical bandgap of hBN, from ~5.3 eV for bulk material to ~6 eV for monolayer, has driven interest in hBN as a component in deep ultraviolet detectors and emitters [50]. Recent studies have demonstrated electroluminescence and photocurrent generation from hBN-based heterostructures, which are expected to exhibit higher photoelectric efficiencies than other conventional semiconductor based DUV devices [50,51].

The growth of hexagonal boron nitride islands differs from those of its carbon-based counterpart due to the lack of inversion symmetry. The presence of two species of atom in the lattice leads to a differentiation of the zigzag edges as mentioned before [52]. Since the A and B sites of the sublattice are filled with B or N atoms the zigzag edge consists of entirely one element or the other. The result of this is a potential for different growth rates between the nitrogen-terminated zigzag ($Z_N$) and boron-terminated zigzag ($Z_B$) edges, which leads to island shapes not observed in the graphene growth on some substrates and with some growth methodologies [52,53].

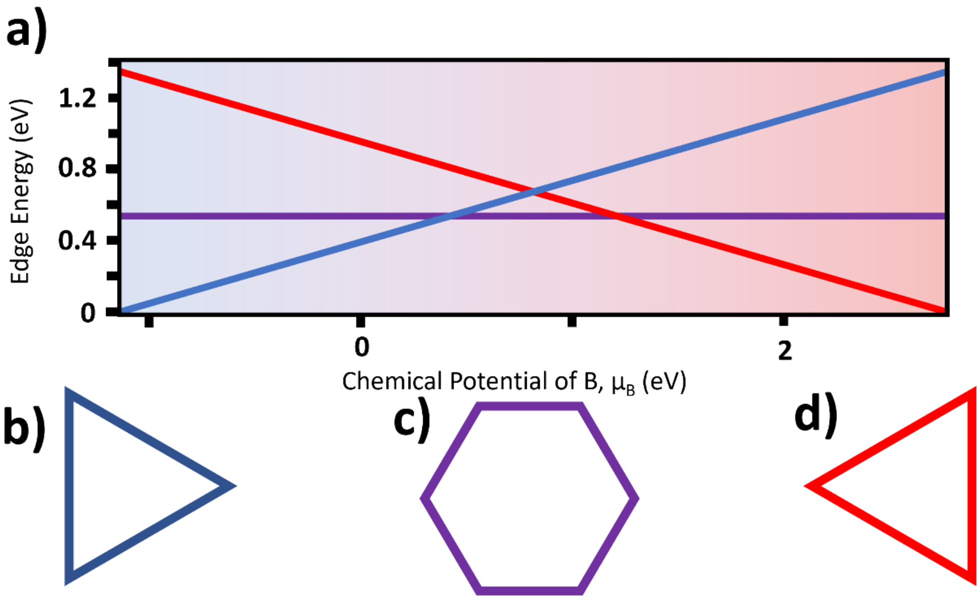

Figure 2.4 – The graph in a) and the shapes presented in b) – d) have been taken from Liu et al. (2011), in which the chemical potentials of the constituent elements of hBN during growth are seen to result in different island shapes on the surface of a Cu substrate. In a) the dependence of the edge energies of the $Z_B$ (red), $Z_N$ (blue) and A (purple) edges on the chemical potential of B during growth is depicted. The expected island shapes at $\mu_B$ of -0.86 eV, 0.85 eV and 2.69 eV are depicted in b) to d). Though this data was shown for a Cu substrate in the work of Liu et al. the logic applies equally for a graphite substrate, though with unknown values for the chemical potentials and the resulting transitions between the shapes. For each growth state, representing a vertical line on the graph, a different island shape would be expected to result.

Liu et al. discussed the influence of the chemical imbalance of the hBN edges in determining growth of hBN islands [52]. In their 2011 paper, Liu et al. use an equilibrium approach to establishing edge preference, starting by representing the edge energies as a sum over the atoms in the A and Z edges [54]. The preferred edge is found to be dependent on the chemical potential of the system, which itself depends on the chemical state of the constituents, as shown in Figure 2.4 which was taken from the 2011 paper [52]. When the chemical potential of the N species is lower with respect to the B species $Z_N$ edges will arise as depicted in Figure 2.4 a). The chemical potential of the constituents in the system are dependent on several factors, such as the pressure, temperature, and the density of atoms of the species. Under MBE growth conditions the system is not in chemical equilibrium, however the energetics considered by Liu et al. are likely to still be relevant to our studies [52].

Zhang et al. established the nucleation barriers of the different edges, and describe how the barrier energies of both zigzag edges vary with the chemical potential of the boron [53]. By considering the growth from a kinetic approach, as opposed to the energy equilibrium approach of Liu et al., they show that the direction-dependent growth velocity depends exponentially on the energy barriers. As a result, ‘rounded’ polygons, or shapes with edges distinct from zigzag or armchair, are very unlikely. hBN islands will therefore be predicted to take on triangular, hexagonal or dodecagonal shapes as seen in Fig 2.4 taken from Liu et al. (2011) [52]. If nucleation occurs at step edges the resulting islands will be trapezoidal or triangular, depending on the preferred shape and the relative orientation of the step to the hBN lattice. Though the theoretical work of Zhang et al. assumed a copper substrate, it is likely applicable to other substrates too [53].

The key observations to be taken here from these works are the limited variety of island shapes, and the dependence of these island shapes on the growth conditions. The influence of the relative proportions of boron and nitrogen species on the predominant growth edge should also be noted.

### 2.1.3 Properties of Vertical G/hBN Heterostructures

The overlap of two similar lattices results in the formation of a superlattice, often described as the 2D analogue to the beat frequencies observed by the overlap of 1D waves. In the systems considered here the lattices are predominantly hexagonal, with similar though not identical lattice constants. Figure 2.5 depicts the overlap of two similar hexagonal lattices, rotationally aligned, with a mismatch in the lattice constants of 5.5%. As can be seen the two lattices periodically completely align and then misalign, resulting in a hexagonal superlattice. The period, referring to this distance between aligned sites, of this hexagonal superlattice can be obtained with the following equation.

$$\lambda = \frac{(1+\delta)a}{\sqrt{2(1+\delta)(1-cos\phi)+\delta^2}} \tag{2.21}$$

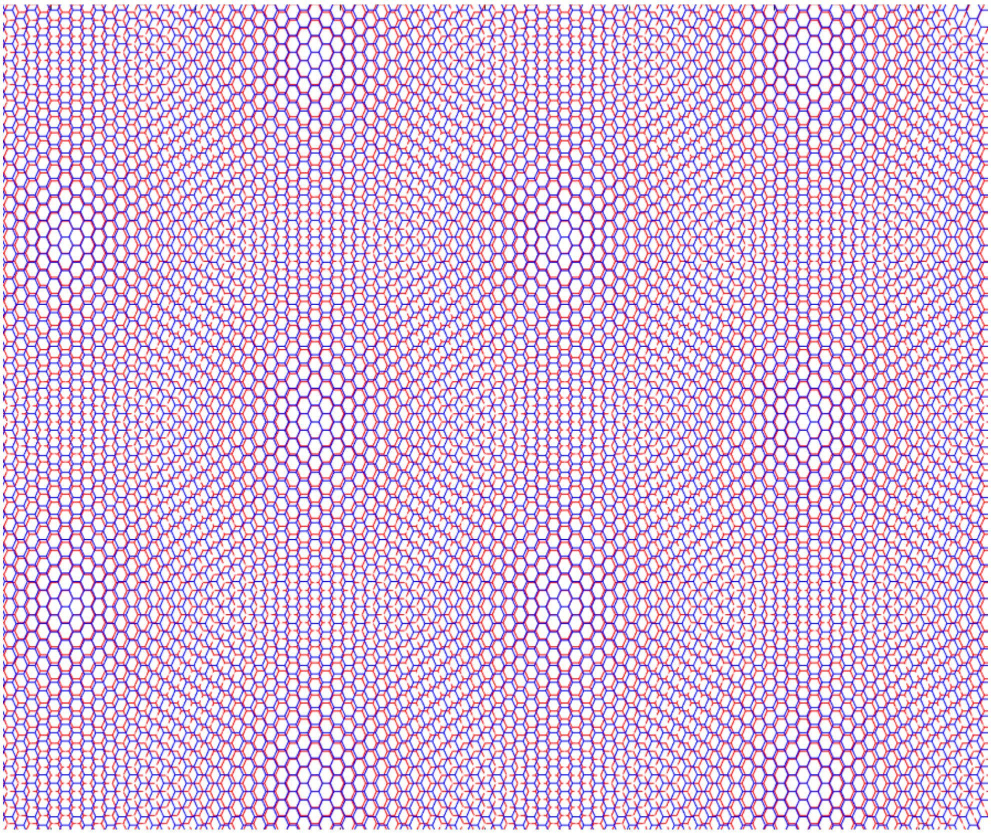

Figure 2.5 – Two overlaid hexagonal lattices with lattice constants differing by 5.5% are shown, with the resulting superlattice being visible by the transition between regions in which vertices overlap perfectly and those in which vertices are displaced significantly between the two lattices. The process is identical to that seen in the overlap of graphene and hBN lattices, though with a lattice mismatch of 1.8%.

Equation 2.21) has been used to show the dependence of the moiré superlattice period, $\lambda$, on the lattice mismatch between the graphene and hBN, $\delta$, the lattice constant of graphene, $a$, and the rotational offset between the two, $\phi$ [55]. The moiré period is strongly dependent on the rotation of the surface and on the relative difference in lattice constants. The smallest period in graphene on hBN is obtained when the rotational misalignment is $30^{o}$ due to symmetry considerations and leads to a moiré period of ~4.46 Å. The maximum period that can be expected with zero rotational misalignment of the lattices is 13.6 nm. However, it is possible to achieve a greater period by application of strain. Strain applied by stretching or compressing the lattices reduces the average difference in lattice constants and results in much larger moiré periods. At 1.8% strain a lattice mismatch of zero is reached, resulting in an infinite moiré period.

The two lattices of graphite and bulk hBN exhibit different stacking modes. The two relevant stacking modes are labelled as AA and AB stacking. As depicted in Figure 2.6 a) in AA stacking the lattice sites of one monolayer lie directly above the sites of the layers above and below. In AB stacking, shown in Figure 2.6 b) the lattices of the layers above and below are offset by a vector equal in length to the edge of one hexagon and oriented along the armchair direction. AB stacking, sometimes referred to as Bernal stacking, is the mode exhibited by graphite. The stacking for hBN consists of an AA' structure, where the atoms of each adjacent layer have identical lateral co-ordinates, but the site elemental occupancy is inverted between adjacent layers. For a vertically stacked, incommensurate heterostructure the adjacent layers will consist of different materials, requiring new notation. If the lattice constants of the two adjacent lattices differ then the stacking will change periodically across the surface. An example of this is depicted in Figure 2.6 with a graphene monolayer lying beneath a hBN monolayer. As can be seen in Figure 2.6 b), where the two lattices are aligned such that the sites in the hBN layer lie directly atop those in the graphene layer the stacking can be labelled AA-type. Regions of AA-type stacking will be separated by a lateral distance comparable to the moiré period of the structure with the edges of the moiré hexagon exhibiting a transition between AA-type and AB-

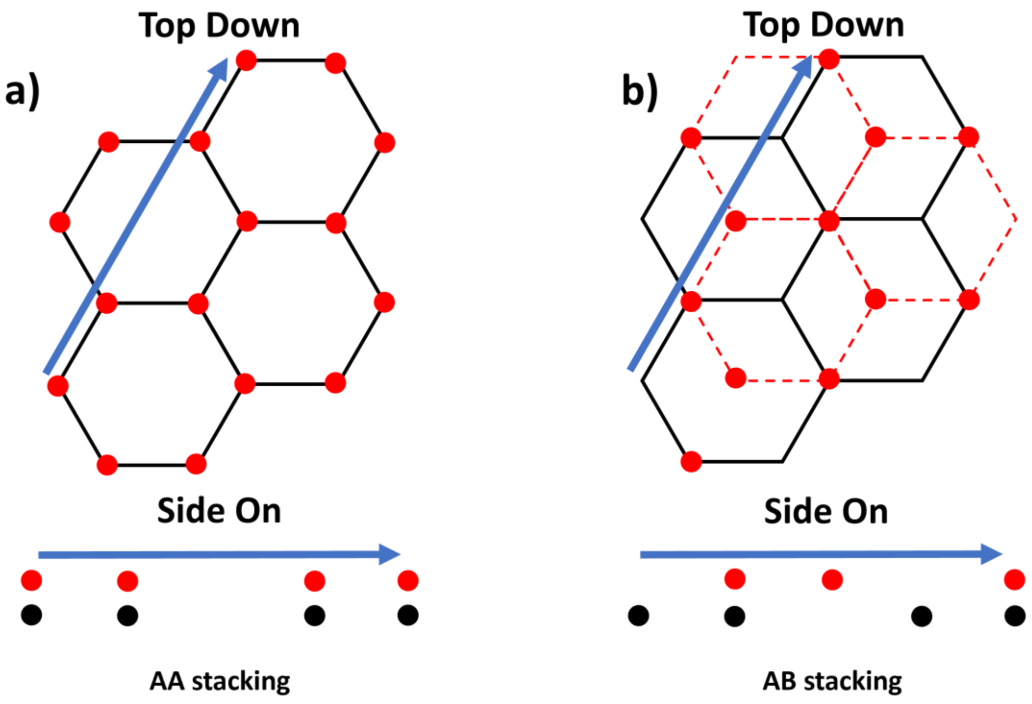

Figure 2.6 – Models depicting the AA and AB stacking modes. For each stacking mode a top down and side on view is presented. A blue line identifies the profile along which the side on view has been taken. In a) the corners of the hexagons in one monolayer lie directly atop the corners of the hexagons in an adjacent layer. This is known as AA stacking, and is referred to as AA' in the case of hBN when B atoms of one layer lie directly atop N atoms in the adjacent layers. In b) half of the sites at the corners of the lattice of one layer lie directly atop the corners of the hexagons in the adjacent layers. The remaining half of the sites, alternating as one goes around the hexagon, instead lie at the centre of the hexagons in the adjacent layer. This stacking is referred to as AB or Bernal stacking and is common to graphite.

type stacking [56]. At the corners of the moiré hexagons AB-type stacking will occur, with either B or N atoms occupying the sites directly above the graphene sites in the layer below. Adjacent AB-type regions will exhibit alternating elemental occupancy, as identified by Figure 2.7 c) and d).

Woods et al. describe how the graphene and hBN heterostructure can undergo a local transition into a perfectly commensurate state. In this commensurate state the graphene lattice locally distorts to match lattice constants with the hBN over a small area, with the resulting strain accumulated in edges of the commensurate region [57]. The resulting alternating regions of lattice matching and strained

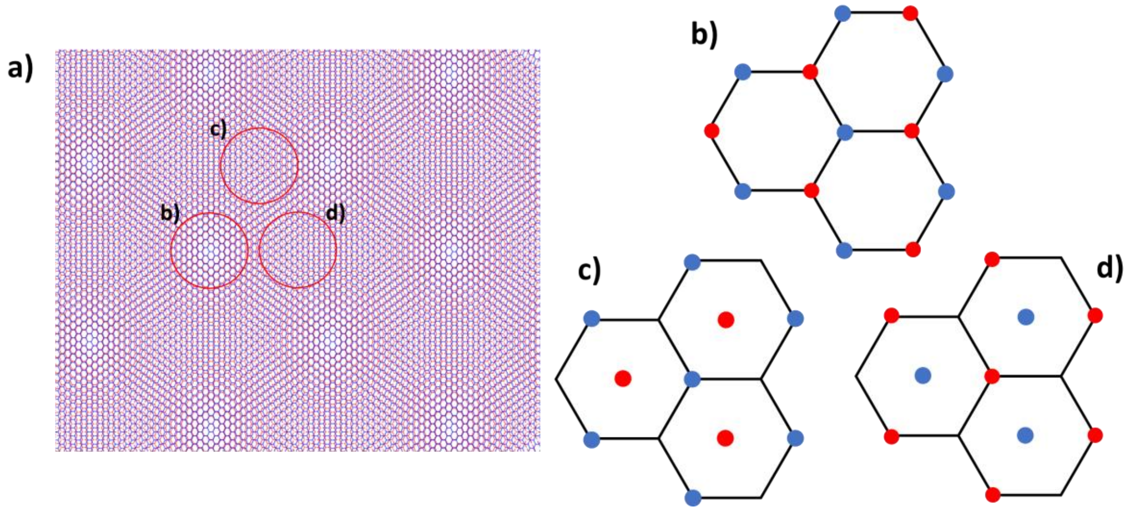

Figure 2.7 – Presenting atomic models of the changes in stacking mode through a hBN on graphene heterostructure. The moiré pattern is depicted in a) and three positions of the lattice are highlighted. For each position the atomic model is shown in b), c), and d). In these models the black lines refer to the graphene layer, and the blue and red circles identify the boron and nitrogen atoms of the hBN, respectively. At the centre of the moiré hexagons, as shown in b), the stacking is similar to AA, with graphene atoms lying directly beneath the B and N atoms. At corners of the hexagons shown in c) and d) an AB-like stacking is obtained. At adjacent corners of the moiré hexagons the elemental occupancy of the site lying above the centre of the graphene hexagons is inverted between boron and nitrogen.

edges can be observed as a moiré lattice with a period greater than the unstrained maximum period of 13.8 nm.

Summerfield et al. proceeded to show that the graphene lattice can be grown into this commensurate state by means of high temperature MBE (HT-MBE), with the maximum period observed governed approximately by the growth temperature [12,14,15]. The proposed explanation for the appearance of the commensurate state in the HT-MBE produced heterostructures was the difference in the thermal coefficients of graphene and hBN at the growth temperatures [15,58]. This leads to a build-up of strain on the surface as the sample cools to room temperature post growth [15].

The presence of the moiré superlattice influences the electronic properties of the material. In graphene the superlattice introduces secondary Dirac peaks with an energy dependent on the wavelength of the moiré lattice [23,55,59]. It has also been previously hypothesised that the presence of the superlattice could open up in a bandgap in graphene, which is required for the creation of efficient graphene transistors [60,61]. The specifics of the bandgap are impacted by the stacking of the vertical heterostructures, alongside any twist angle between the layers, and the layer spacing, with the potential for a maximum bandgap of ~ 160meV [62].

In addition to the formation of a bandgap, potential optical properties of G/hBN heterostructures have previously been discussed. As graphene is excited in the visible region and hBN in the ultraviolet region, the two components of the hBN/G heterostructure are mostly unimpacted from an optical standpoint [63]. As a result of this and the primarily c-axis oriented photoemission from hBN, photocurrent generation in G/hBN/G vertical heterostructures was investigated by Song et al. [51]. In this study the graphene layers, acting as electrodes, efficiently collected the photocurrent generated by the bulk hBN material. This shows the potential applications for G/hBN heterostructures for the purposes of ultraviolet detection or emission.

### 2.1.4 Lateral G/hBN Heterostructures

Lateral heterostructures, as opposed to vertical heterostructures, are confined to the 2D plane. In lateral heterostructures an interface has formed between two materials with similar lattices within a single plane of atoms, such as an in-plane interface formed between graphene and hBN. The structures have generated particular interest for potential applications in the fields of integrated circuits and quantum technologies. Previous instances of devices fabricated with lateral heterostructures of some transition-metal dichalcogenides have exhibited very high-performance [64,65].

The fabrication of G/hBN lateral heterostructures is additionally valued for the potential to design for the energy band modulation of the resulting 2D material [66]. The formation of high $I_{on}/I_{off}$ ratio field effect transistors (FETs) via G/hBNC/G heterostructures has additionally shown the potential for incorporating the two materials, with variations in the relative carbon level of the BNC material dictating the band structure and providing a means for tunability within the purely 2D system [67].

Beyond the tuneable band structure G/hBN materials exhibit localised energy states at the 1D interface. These states exhibit a blue emission unobserved in the separate materials that can be enhanced by the increase in interface density of the surface [68]. Kim et al. propose that other unexplored properties of these interfaces may exist, such as unknown optoelectronic, or thermal properties, arising from the disorder inherent to the lattice mismatch [68]. As a result of this interest there have been several studies that have worked to produce lateral heterostructures of G and hBN on copper substrates through the use of CVD [43,66,69,70].

In these works, the reliable growth of graphene on Cu has been used to provide island seeds for the nucleation of the hBN. Alternating the deposition of the precursors for G and hBN has successfully produced a 2D striped heterostructure upon the copper surface. The widths of the ribbons can be controlled down to the scale of 100 nm. Regions of the graphene and hBN produced in this manner exhibit wrinkles, expected to arise from differences in the differential thermal expansion coefficient between the grown materials and the substrate [71].

Sutter et al. (2014) describe how the certain metallic substrates, such as the Cu commonly used in producing the G/hBN structures, inhibit the phase separation between the graphene and hBN resulting in the formation of a B-C-N phase [70]. The presence of C adatoms on the Cu substrate was shown to result in this mixing and minimising the C adatom density provided a means to reduce the prevalence of the B-C-N phase.

### 2.1.5 Superlattices of graphene and hexagonal boron nitride

Superlattices consist of two or more materials layered periodically, with layer thicknesses usually much greater than the lattice constant. Differences in band structures result in a structure similar to multiple quantum wells, whereby the barrier width is small enough that the wells are coupled. This simple understanding of superlattices may be complicated by the presence of edge states between the two or more materials, which may be introduced by mismatching of the lattices. Additionally, the growth of one layer upon the other is usually dependent on the matching of the concurrent lattices, limiting the potential materials from which superlattices might be constructed.

Whereas the majority of superlattices are vertical, stacked such that the layer thickness of the constituent materials defines the periodicity, the growth of 2D materials opens the possibility for lateral superlattices constrained to a single monolayer. For lateral superlattices the periodicity is defined by the widths of the nanoribbons making up the constituents. Graphene and hexagonal-boron nitride superlattices have been modelled previously, and some studies have reported the fabrication of large domain superlattices with these materials [72].

Significant interest in G/hBN lateral superlattices has focused on the thermoelectric properties of the monolayer [73–75]. The generation of electricity from waste heat, a subject of considerable interest for power-saving measures, has been previously limited by low energy-conversion efficiencies, defined as ZT. A predicted ZT of 2.5 was predicted as a potential limit for some G/hBN superlattice structures, comparable with other well-performing materials at the forefront of thermoelectric study [74,76]. To increase the energy-conversion efficiency of these structures the periodicity must be decreased, as the density of interfaces has been shown to lead to a reduction in thermal conductivity, on which ZT is inversely dependent [73].

Superlattices of G/hBN on the scale of ~100 nm domains have been previously reported, from which a split-loop resonator was produced [72]. The produced monolayers could be transferred to other substrates, providing a means for the fabrication of compact and flexible components. However, for the purposes of achieving thin, high-efficiency thermoelectric materials, much smaller domains must be grown.

### 2.2 Growth Processes for 2D Material Production

Bottom-up growth methods for the epitaxial production of materials on a substrate can result in one of three primary growth modes. These growth modes are commonly referred to as Frank-van der Merwe (FvdM), Volmer-Weber (VW), and Stranski-Krastanov (SK) growth. In FvdM growth the material accumulating on the surface will form monolayer sheets, starting subsequent layers only when the first is nearly complete. VW growth consists entirely of the growth of 3D islands, without

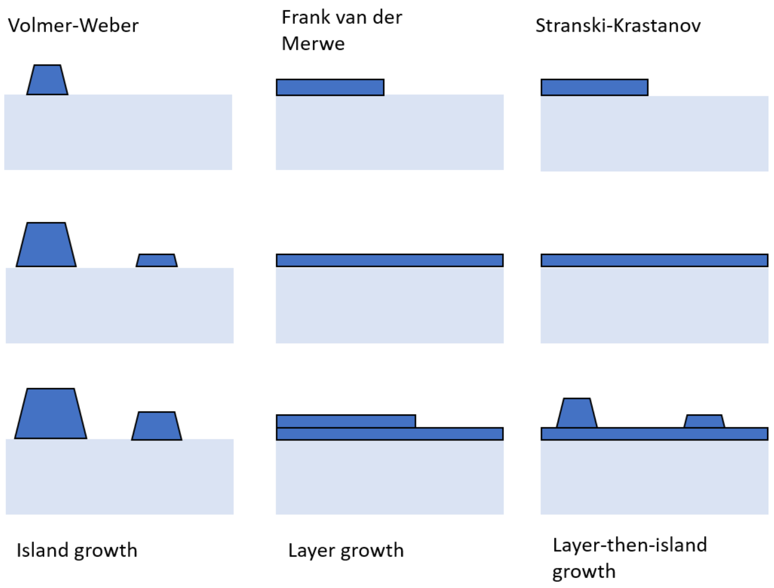

Figure 2.8 – Three vertical diagrams depicting the distinct epitaxial growth modes of a material onto a substrate. Characterised by differing equilibria between the strength of interaction between the material and itself, and the material and the substrate, the result is island growth, layer growth, and layer into island growth as a result of a weakening substrate influence.

the formation of 2D layers. The third growth mode, SK growth, begins as 2D sheet growth and subsequently transitions into island formation after the formation of some complete monolayers.

The three growth modes arise from differences in adatom-adatom and adatom-surface interactions. If adatom-adatom interactions are stronger than those between the adatom and the surface the growth will tend towards the formation of 3D islands and the VW growth mode. If adatom-surface interactions are dominant, then monolayer sheets will form. The SK mode occurs when both of these conditions are true at different periods of the growth process. Initially the surface-adatom interactions are the strongest, leading to monolayers. As monolayers form, strain will accumulate from lattice mismatches between substrate and the growing layers, which results in a transition towards island growth after one or more layers.

A purely 2D growth mode is discussed by Lei Liu (2014) as a distinct mode of growth to FvdM [43]. The three criteria for this mode are, growth entirely within a single atomic plane, the growth of material from a 2D seed, and the crystallography of the grown material being entirely governed by the seed. The results are thus distinct from the FvdM mode by the lack of any multilayer formation at later growth times, with some process being necessary to inhibit the formation of additional layers. This growth mode would likely be preferable for the formation of 2D lateral heterostructures.

Structural qualities of the graphene surface should be considered when estimating the results of a growth technique such as grain sizes, defect concentration, and surface roughness. Electronic properties such as carrier mobility are often compared when determining the quality of the material [42,46,69]. This is because the carrier mobility depends on the density of ionized dopants, intentional or otherwise, and on the density of defects present in the sample. Other factors, such as any substrate, will also influence the carrier mobility, so it is not a perfect method for the identification of pristine monolayers.

Graphene can be grown following the Frank van der Merwe growth mode (FvdM) on the hBN surface, forming predominantly a single layer growing from the nucleation centre [9,77]. The availability of nucleation sites, the growth rate and the preferred growth edges may vary with the specifics of the growth process, but the essential growth mode is unchanged. To promote graphene growth over the other allotropes of carbon it is often preferable to make use of templating, whereby the growing monolayer is guided by the substrate layer. Several hexagonal lattices can used for this purpose, such as the previously mentioned hexagonal boron nitride and the iridium (111) surface [23,59].

When a monolayer or higher step is present on the surface of the growth substrate it will often provide a site for the nucleation of new monolayer growth. In these instances the shape of the monolayer island will be obstructed by the presence of the step, as a result of the energy cost for adsorbed atoms

**a) Islands of hBN nucleated on terraces**

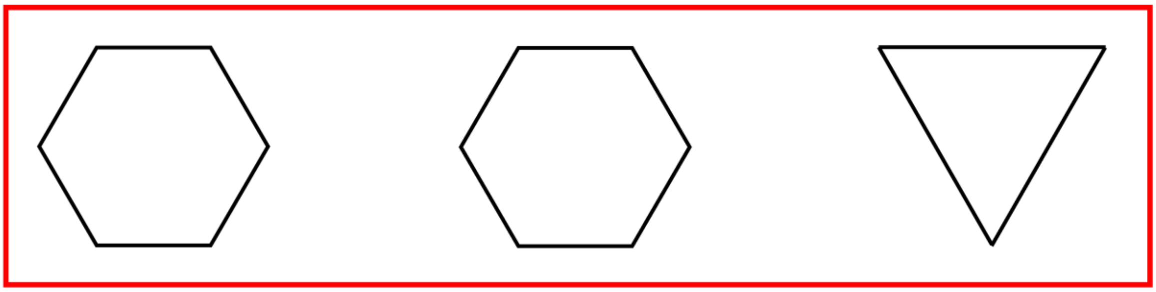

**b) Islands of hBN nucleated from steps**

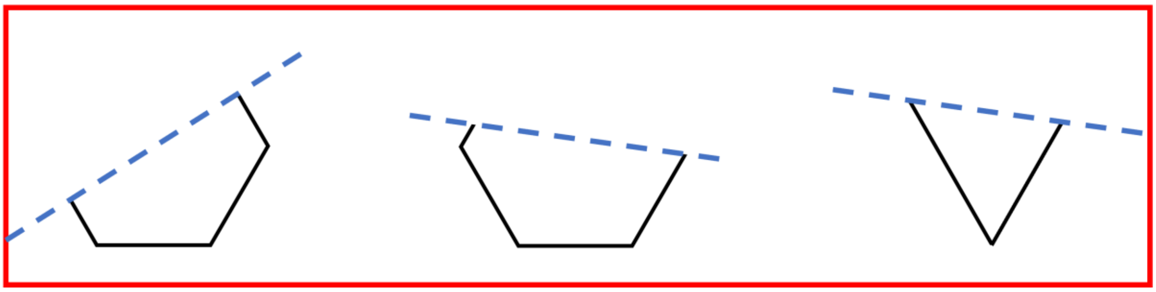

Figure 2.9 – Epitaxial hBN forms hexagonal or triangular islands on many substrates. Diagrams are presented to show the alternate shapes that would be expected from nucleation along a step on the surface of the substrate. In a) the original shapes are presented, as if nucleation and subsequent growth occurred entirely on a terrace of the substrate. In b) arbitrary steps are drawn across the islands. Steps on the surface hinder adatom migration due to the energy cost of migration up or down steps, which would be expected to limit the growth of the islands.

moving up or down a surface step [78]. In the case of graphene on hBN this results in irregular structures forming at step edges, such as those depicted in Figure 2.9.

For the production of monolayer thickness material both an appropriate substrate and exfoliation or epitaxial growth process must be selected. Four common methods for the fabrication of 2D van der Waals structures are discussed below with the advantages and disadvantages considered. The reasons for the selection of MBE for this work will also be presented.

### 2.2.1 Exfoliation of Graphene

The first identified method for obtaining monolayer graphene is that of exfoliation from a bulk graphite source. This method, now known as the 'scotch tape' method, was first described by Novoselov and Geim in their seminal 2004 paper, 'Electric Field Effect in Atomically Thin Carbon Films'. The process involves the repeated peeling of thin layers from the bulk material and the subsequent deposition of these thin layers onto a substrate [21]. Though the specific process varies significantly between studies, how the technique results in graphene flakes remains the same.

First, a small flake of the source material of about 1-2mm across, is placed onto an adhesive tape; here we used Scotch® tape. The sticky side of the tape is folded in half and the two sticky ends brought together until the crystal is fully enclose by the tape, at which point the tape is pulled apart. This will cleave the crystal parallel to the plane of the layers as a result of the relative weakness of the interlayer forces. This procedure is then repeated until the tape is coated in a layer of thin crystalline material. Finally, the loaded tape is firmly pressed onto the substrate surface and peeled away, leaving some of the crystalline material on the substrate.

While the majority of material deposited in this way will consist of few-layer up to several tens of microns thick material, monolayer material will also be found on the surface. Graphene and few layer graphene (FLG) obtained in this manner both exhibit very high mobilities, up to about ~10,000 $cm^2/Vs$.

As noted before carrier mobility is commonly used as a metric for identifying high quality material due to its dependence on defects density.

Alternative methods for overcoming the interplanar interaction of van der Waals crystals to produce mono- or few-layer material are available, such as ball-milling, electrochemical exfoliation, and liquid-phase exfoliation. All these methods use shearing and normal forces, but the resulting distributions of large to small crystals and bulk to monolayer flakes will differ between methods. Of these techniques liquid-phase exfoliation (LPE) has been adopted by some companies for the large-scale production of few-layer material. The produced material remains in a stable dispersion until deposited onto a surface, and consists of flakes with length scales of 300 – 800 nm and thicknesses less than ~10 ML [79]. Flakes of these scales are valuable for the fabrication of conductive coatings and printed electronics [80].

### 2.2.2 Chemical Vapour Deposition of Graphene and hBN

Chemical vapor deposition (CVD) involves the interaction of reactants present in a gaseous form with a heated catalytic substrate, such as that depicted in Figure 2.10. The process aims for the formation of crystalline materials on the substrate, with thicknesses ranging from individual monolayers up to microns. In the conversion of the reactants to the final products three interactions are involved, these being thermal decomposition, chemical synthesis and chemical transport [1]. Thermal decomposition refers to the breakdown of a reactant into one or more products as a result of heating. Chemical synthesis refers to the reaction of one or more reactants into one or more products. Finally, chemical transport is a process by which reactants at point A react to form volatile intermediate products, which may diffuse through the controlled environment until reacting at a destination to form the final products.

These processes are controlled by manipulation of the flow rates, densities of precursor gases, and the temperature of the substrate. By using lower pressures, the volume flow and velocity of the gas are greater for the same molar flow over the substrate, and the precursor concentration is lower. The low concentration and high velocity of the incoming material improve the controllability of the reactions. Low pressures can contribute to differences in the resulting surface, as seen in $MoS_2$ where a layer-by-layer growth is observed at low pressures, compared to a mixture of mono-/multilayers at higher pressures [1].

Temperature is another tuneable parameter of the system, for which strict control is necessary. Even small changes in the temperature at the source can alter the saturation pressure of precursor materials resulting in significant impacts on the growth. It also influences the reactions in the system as higher temperatures can overcome greater energy barriers or increase the rate at which reactions occur. For example, increasing the temperature of the substrate increases the diffusion rate of atoms on the surface, which improves the uniformity of the final product.

In general, CVD growth of graphene makes use of a methane precursor over a metallic substrate [24,46,69,77,81]. The methane gas dissociates to allow carbon accumulation on the substrate at

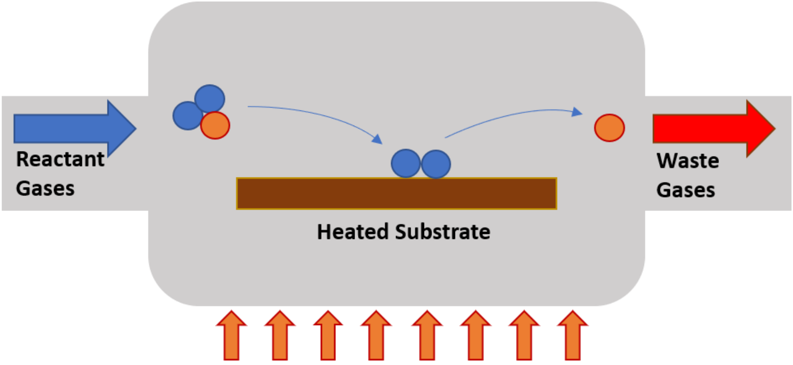

Figure 2.10 – A diagram depicting the chemical vapour deposition (CVD) process. Reactant precursor gases are passed over a heated, usually catalytic, substrate resulting in the breakdown of the gas into constituents. Some of the reaction product will then go on to form the epitaxial layer, while the rest is removed from the chamber as waste gases. The manipulation of the precursor material, flow rate, alongside substrate material and temperature, make this process highly tuneable.

temperatures between 1000°C and 1600°C. Choice of precursors and substrate can also significantly alter the quality of the final product. Substrates that have previously been used for the production of graphene by CVD include Au, Cu, Co, Ir, Fe, Ni, Pt, Rh and Ru [82]. Of the various catalytic metals used, the most common substrate is copper, though nickel and iridium have also been widely studied [83,84]. The copper foils used in the process are low cost and exhibit low carbon solubility at standard CVD growth pressures [85]. The purely diffusive growth process observed on copper and gold substrates favours the production of a single complete monolayer graphene due to the inability of the methane feedstock to access the catalyst where the graphene is already present [82]. This occurs due to the low solubility of carbon in these metals, and results in reduced multilayer formation and larger grain sizes compared to some other substrates [10].

The quality of the graphene layers formed via these processes can approach that of mechanically exfoliated graphene. This has usually been estimated by the field effect mobility exhibited by the graphene samples. Exfoliated graphite devices offer mobilities in the range of 3000 to 10,000 $cm^2/Vs$ [21], while higher quality CVD grown samples on copper attain values up to 5500 $cm^2/Vs$ [83,86]. By varying the substrates used in the growth process it has been shown that significant improvement in the graphene-based devices can be obtained. The lack of dangling bonds and the resulting low reactivity of the hBN lattice leads to greatly improved mobilities [5]. To make use of these beneficial properties one can transfer CVD-grown graphene onto the hBN film resulting in mobilities of 20,000 $cm^2/Vs$ or larger, much greater than exfoliated graphene on $SiO_2$ substrates [5,87].

hBN growth by CVD can be achieved through the use of ammonia borane or borazine precursors [85]. Subsequent graphene growth on these CVD-grown hBN layers tends to form layers beneath, rather than on top of the hBN layer [81]. If the hBN is thick enough to isolate the growing graphene from the metallic surface the graphene will grow on the top surface of the hBN. For graphene grown on thick hBN crystals moiré patterns occurring on the islands of graphene show that the graphene lattice aligns with the underlying hBN, and interfacial stress is mostly released [77]. These graphene islands exhibit hexagonal forms, following the zigzag and armchair edges of the graphene lattice. This is to be expected for graphene growth that has been templated by the underlying hexagonal lattice.

Since hBN is an insulator, carrier mobility cannot be used to characterise sample quality. As described by Uchida et al. (2020), grain size can provide an alternative method for comparing material quality between studies [88]. Substrate selection plays a substantive role in the quality and functionality of grown hBN material, with a variety of substrates having been used previously. Metallic substrates for hBN growth, such as Cu(111) thin films, Cu foil, Ni(111), and Ir(111) among others, provide a catalytic surface for the decomposition of the hBN precursors [89–93]. These surfaces exhibit hexagonal symmetry and lattice constants similar to that of hBN. As hBN has previously been shown to preserve the mobility of graphene layers when acting as a substrate, several studies have been performed to grow mono- or few-layer hBN with large domains. A primary goal of the CVD production of hBN has been to maximise the scale of hBN grains in order to reduce presence of defects inherent in the merging of domains. Studies on Cu(111), Cu foil, and Ir(111) have identified the importance of steps in the metal surface from which hBN may nucleate [90,92,94]. Steps on the Ir(111) and Cu(111) surfaces were shown to align the orientation of nearby domains, reducing the defect density upon coalescence. Similarly, the use of step edges in an annealed Cu (110) foil by Wang et al. resulted in the production of a 100-square-centimetre single-crystal hBN monolayer [94]. To date CVD growth of hBN on Cu(111) substrates provides for the greatest lateral scale production of the single-crystal hBN monolayer. Ni(111) substrates are considered valuable for the production of hBN due to a better lattice match than other transition metals, and a stronger interaction between metal and grown film. These properties have the potential to increase the growth rate of the material, improving the scalability of production. It has additionally been shown that hBN material grown on the Ni(111) surface via CVD allows for the fabrication of 2D adlayers above and below the hBN layer, providing a means for the catalysed production of multiple 2D layers into atomic heterostructure stacks [95].

The study of hBN growth on non-catalytic substrates, such as sapphire and $SiO_2$, is considered valuable for the avoidance of transferring the resulting material for device fabrication, such as single photon emitters and 2D FETs [96,97]. Growth on sapphire surfaces is also valuable as it provides a means for the integration of hBN into existing device platforms, such as GaN and Al(In,Ga)N. Similarly, deposition of hBN on silicon substrates allows for simple integration into existing semiconductor device structures. However, CVD growth of hBN on non-catalytic substrates tends to produces low grain sizes, usually on the order of ~100 nm [98]. The largest domain size for a non-catalytic substrate to date was ~1 µm on a graphite surface [99]. In comparison the growth of hBN on a Ni-Fe film on r-sapphire results in grain sizes over ~10 µm [88]. As with previous growths of hBN on metallic substrates, transfer of the hBN onto other substrates is necessary for the formation of many devices. During this transfer process the introduction of defects is possible and thus direct growth of hBN onto the final substrate remains preferable.

The growth of hBN on HOPG substrates is of interest as a path towards the fabrication of multilayer graphene/hBN heterostructures, acting as a template for first layer growth. Fabrication of hBN on HOPG is additionally valued for the two-dimensional nature of the HOPG material, and the avoidance of transfer processes. Previous growths of hBN on HOPG via MBE have also demonstrated high optical quality, necessary for the production of potential DUV emitters [12]. It is for these reasons that HOPG substrates were selected for hBN growth in this work.

### 2.2.3 Molecular Beam Epitaxy of Graphene and hBN

Molecular beam epitaxy is a process whereby evaporated beams of precursor material impinge upon a heated substrate under ultra-high vacuum (UHV) conditions (pressures < $10^{-9}$ Torr). The beams are formed inside effusion cells by sublimation of the bulk source material. As shown by the diagram in Fig. 2.11, the beams then traverse the ultra-high vacuum environment onto a substrate mounted atop a heater [100]. A low depositon rate can be used in an UHV environment, allowing for slower, more controllable growth. Several parameters in the system can be tuned to control the growth. Examples of these parameters are the nature of the effusion cell and the species source material it produces, alongside the incoming flow rate, substrate, and substrate temperature, all influence the results of the growth [100].

Previous studies by the Nottingham MBE group have investigated the practicalities of growth and the unique features of graphene and hBN produced using high temperature molecular beam epitaxy (HT-MBE) [39,101,102]. Previous attempts to grow graphene by MBE were unable to produce clean graphene, with small, nanometre scale, domains and large quantities of amorphous carbon material on the surface [9,103]. These early growths were carried out with growth temperatures lower than 1000°C, being limited by the available MBE systems.

With the introduction of the modified Veeco-system at Nottingham higher growth temperatures have been used and shown to produce much higher quality samples. Graphene has been grown on hBN flakes supported by a 1cm$^2$ sapphire chip. At temperatures at or above 1650°C the graphene layer exhibits greatly reduced defect presence, as established by Raman spectroscopy in Cheng et al. (2016) [12]. Samples produced in this manner additionally exhibit graphene domains of the order of ~20µm [15]. These improvements appear to arise from the significantly improved diffusion of carbon on the hBN surface at these temperatures.

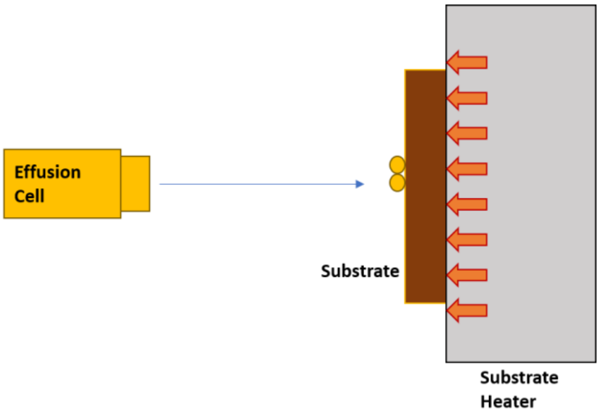

Figure 2.11 – A diagram is presented of a simple molecular beam epitaxy (MBE) system. In this system an effusion cell containing a precursor material is heated resulting in a beam of constituent material. The beam passes through an ultrahigh vacuum environment until collision with the substrate. The epitaxial layer then accumulates from this material. The precursor material, substrate, growth temperature and flow rate are all variable parameters, allowing for precise control over the resulting surface.

hBN has been grown on HOPG substrates in the same MBE system. Laleyan et al. and previous works from Nottingham have shown higher temperatures, such as those above 1300$^{o}$C, lead to monolayer boron nitride growth [8]. The grown material was shown to exhibit minimal defects and high crystallinity.

In Chapter 5, a study has been carried out comparing the quality of graphene material generated with different carbon sources during MBE growth. Prior studies of the high-temperature molecular beam epitaxy (HT-MBE) growth of graphene used one of two different sublimation sources. The first of these sources consisted of a simple graphite filament, through which a current was passed [14,15,104]. This results in Joule-heating of the filament and sublimation of carbon clusters, which can then be directed onto a substrate. The source has been described as unreliable in deposition, with the quality of the deposited sheets varying between depositions. The second source consisted of a sealed tantalum (Ta) tube containing graphite powder [14,16]. Joule-heating of the Ta tube causes a chemical reaction between the carbon and Ta, allowing for the diffusion of the carbon through the walls of the tube. At the external surface of the tube the carbon can evaporate and be funnelled towards the substrate.

The potential benefits of this second source, described by Albar et al., include the sublimation of primarily atomic carbon material, as opposed to the carbon clusters obtained by other sources [16]. This source was limited in practice by the semi-regular breakdown of the filament, with a new filament being required after every fifth or sixth deposition. These sources are compared to a new e-beam sublimation source in Chapter 5.

### 2.2.4 SiC Decomposition for Graphene Production

Graphite can be formed by the thermal degradation of silicon carbide, SiC. When SiC is heated to temperatures above 1150$^{o}$C under vacuum conditions the vapor pressure of Si becomes very high compared to that of the C [105]. This results in a silicon-depleted region near the surface, which will restructure into graphite due to its thermodynamic stability. Charrier et al. established that the substrate temperature during the process strongly influences the number of layers in the resulting material, and that single-layer graphene can be obtained [106]. Graphene produced by SiC decomposition does not require transfer to other substrates for practical application, as it resides on a semiconducting Si substrate common to electronic devices.

Initially graphene produced from these techniques was of low quality as the high sublimation rate and low temperature led to minimal surface reconstruction. By encapsulating the SiC crystals in graphite the evaporating system is brought closer to equilibrium, allowing for more controlled growth. As a result the quality of SiC degradation produced graphene can be significantly improved [107]. In De Heer et al. the quality of the graphene sheet is established with Raman spectroscopy [107]. Raman spectroscopy of graphene, as will be discussed further in Chapter 3, allows for the identification of defect presence by measuring the relative height of the D peak response. The concentration of defects has been assigned as a measure of quality, due to the influence of defects on the electronic and optical responses of the graphene monolayer.

Production of graphene with SiC decomposition in an argon atmosphere at 1 bar was identified by Emtsev et al. to result in a significant improvement in quality and greater monolayer domain sizes [105]. This increase in quality was assigned to the much higher annealing temperatures that can be used before Si sublimation arises. In vacuum conditions Si sublimation becomes significant at 1150$^{o}$C, whereas no sublimation was observed below 1500$^{o}$C in the argon atmosphere. As a result, surface diffusion is increased and surface restructuring can take place prior to graphene formation, leading to a flatter substrate geometry. This method of graphene production is capable of reliably generating mono- to few-layer material with large (2 – 20 µm) domain sizes on a flat, semiconducting substrate [108].

### 2.3 Supramolecular Assembly of CA.M

A supramolecular network is an interconnected complex of molecules bonded with non-covalent interactions. For example, monolayer networks bound with van der Waals interactions or hydrogen bonds. The formation of these supramolecular assemblies is governed by molecular self-assembly processes. Such processes are characterised by the lack of outside influence on the ordering of the resulting network, with the structure of the network arising primarily from the chosen substrate and the molecules contributing to the network.

The networks formed from molecular self-assembly exist in a thermodynamic minimum of the system, and as a result their production is highly reliable [109]. Candidate molecules must be carefully selected, or network formation may not occur. Due to the weak nature of the interactions joining the molecules the sum of entropic contributions to the formation of a network can become significant [109]. To limit this the molecules involved should be capable of forming multiple noncovalent interactions.

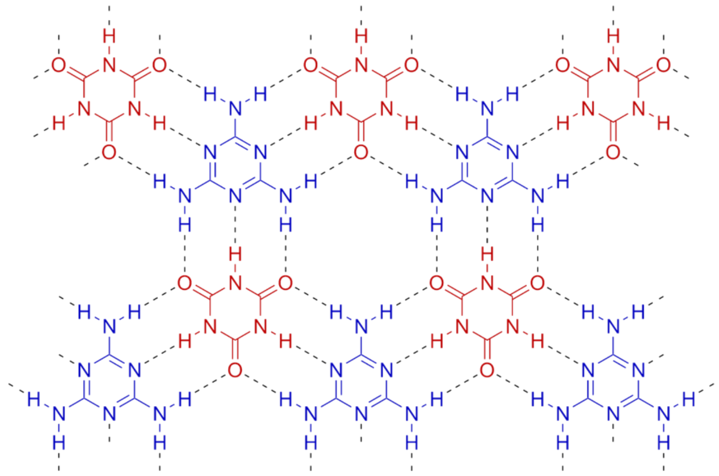

Figure 2.12 – Displayed is the lattice formed by cyanuric acid and melamine, represented in red and blue respectively. The dashed lines joining labelled atoms represent the positions of intermolecular hydrogen bonding, whereas filled lines correspond to intramolecular covalent bonding. The trisymmetric nature of the two molecules allows for the formation of hexagonal networks, repeating with a period of ~0.99 nm, as measured by Korolkov et al. on the hBN substrate. Hydrogen bonds formed between the oxygen species of the cyanuric acid and the amino groups of the melamine produce the stable 2D network.

The first network considered here is that of cyanuric acid-melamine (CA.M), which forms a repeating structure involving a 1:1 stoichiometric ratio of cyanuric acid and melamine molecules. A diagram of the resulting hexagonal structure is displayed in Figure 2.12, consisting of two sublattices distinguished by the presence of one or the other of the molecular components. Each molecule forms three hydrogen bonds with each neighbour, so the structure is comparatively strong for a supramolecular assembly. Due to the relatively large number of hydrogen bonds the structure is stable up to temperatures around 350$^{o}$C [110]. In contrast to other structures CA.M can be produced in laboratory conditions and the resulting open, hexagonal network is ideal for subsequent functionalisation [111].

A previous study by Korolkov et al. reported that the CA.M network can be used to improve the atmospheric stability of a black phosphorus (bP) surface [112]. The network, after deposition onto the bP, limited the contact of the black phosphorus surface with oxygen and water, removing the pathway for degradation [113]. In that study the CA.M structure consisted of a single near-complete monolayer. Due to its relatively high strength and lack of in-plane conductivity an ordered multilayer formation of

CA.M could be expected to form a stable tunnelling barrier when sandwiched between conducting layers.

### 2.4 Summary

As was discussed MBE is theoretically effective in the production of van der Waals materials at low temperatures without the need for catalytic metal substrates. Until recently minimal studies had been undertaken on the use of MBE for growing hBN/HOPG or G/hBN structures. In this thesis the growth of hBN/HOPG and G/hBN samples produced at high temperatures (>1000$^{o}$C), and analysis of surface morphologies with AFM is reported. In the next Chapter the methodologies and techniques necessary to produce and investigate these heterostructures is detailed.

# Chapter 3: Experimental Techniques

### 3. Introduction to Experimental Techniques

In this Chapter the various techniques for sample preparation and analysis underpinning the research presented in this thesis are discussed. In Section 3.1 a description of the scotch tape exfoliation method is provided. This technique was used to produce thin graphite and hBN flakes on Si/SiO$_2$ substrates for subsequent deposition of cyanuric acid-melamine networks (CA.M), perylene tetracarboxylic diimide (PTCDI), MBE growth of hBN and/or graphene. Scotch tape exfoliation was also used to produce thin hBN flakes on sapphire substrates for MBE deposition. In Section 3.2 the preparation of samples for MBE deposition is discussed, focusing on the cleaning of substrates prior to introduction in the vacuum chamber. The Section also introduces the MBE setup used and the parameters for deposition.

Sections 3.3 and 3.4 provide the underlying theory and the methods used for, respectively, photoluminescence studies and Raman spectroscopy in this work. Photoluminescence was applied to analyse the molecular layers on graphene and hBN substrates. Raman spectroscopy was used to characterise G/hBN samples. In Section 3.5 X-ray photoelectron spectroscopy is described. Data acquired from the technique is presented in Appendix I to discuss the elemental environment at the surface of some samples.

Sections 3.6 and 3.7 describe the setup and methodology for the deposition of PTCDI and CA.M onto substrates via vacuum deposition and immersion deposition, respectively. These layers were deposited on HOPG and hBN/Si substrates.

Images of the grown samples were acquired with atomic force microscopy (AFM) in tapping, contact, or conductive modes. Section 3.8 provides a theoretical basis for the tapping and contact modes with the dependences of measured characteristics on surface properties. The Section then describes the experimental setup used in this work.

### 3.1 Exfoliation of van der Waals Crystals

Exfoliation methods enable production and transfer of thin flakes of vdW crystals onto substrates. In this work the scotch tape method was used to deposit thin flakes of hBN and G onto sapphire and hBN substrates respectively. The fabrication of thin 2D material flakes via exfoliation has been a prominent technique since the isolation of monolayer graphene by Geim and Novoselov in 2005 [114]. Exfoliation methods vary in detail, but primarily consist of the cleaving of vdW materials by mechanical forces [115]. A scotch tape exfoliation method was used for sample preparation in this work with adhesive tapes used to pick up bulk crystals of the relevant material. After pick-up the tapes were folded on themselves such that the crystals stuck to the tape on two sides. By peeling the folded tapes apart the crystals cleave and repetitions of this process result in few-layer or monolayer crystals [116]. Following the loading of the tape with the few-layer crystals the tape is gently pressed onto the required substrate, such that the crystals are in contact with the substrate and the adhesive tape. By slowly peeling the tape away from the substrates some of the few-layer flakes will be deposited onto the surface.

The technique relies on the weak interlayer bonding found in Van der Waals (vdW) crystals in order for the materials to cleave when the adhesive tape is separated. Due to the relatively weak bonding between the planes in the materials, there is a tendency to cleave parallel to the plane. The stronger bonding of the tape to the crystal also results in cleaving during the final deposition. As a result the uppermost surfaces of most of the deposited crystals are expected to be free from adhesive residues. Flakes produced with this method vary in scale laterally from tens to over 100 microns on the surface, and vertically from a single monolayer up to 10s of nanometres. These heights can be identified by AFM, and thinner flakes can be broadly identified via optical microscopy. For thin graphite flakes on

$SiO_2$/Si chips a small contrast between the colour of the flake and the substrate signifies that the observed flake is thin on the order of monolayers [117].

The method works equally well for the production of thin graphitic and hBN flakes and has been used for the preparation of thin-layer material for subsequent MBE depositions as well as CA.M and PTCDI depositions.

### 3.2 Sample Preparation for Molecular Beam Epitaxy

Boron, nitrogen, and carbon were deposited within an MBE with the intent of producing hexagonal boron nitride and graphene monolayers. Prior to MBE growth it is necessary to clean the substrates to remove volatile contaminants. All samples that underwent MBE deposition for this work consisted of thin hBN flakes exfoliated onto a 1 $cm^2$ square sapphire substrate or 1 $cm^2$ HOPG chips. The exfoliation process leaves residues of the adhesive tape on the sapphire surface alongside the thin flakes. This tape residue must be removed prior to transfer into the vacuum system. The process used to clean the hBN/sapphire and HOPG substrates is described in works by Cheng and Summerfield, and consists of two stages [12,15]. The HOPG with the outermost faces exfoliated and hBN/sapphire substrates are firstly immersed overnight in 99.9% pure toluene obtained from Sigma Aldrich. Subsequently, the substrates are annealed in a tube furnace at 300 $^{o}$C and 400 $^{o}$C (HOPG and hBN/sapphire respectively) for 4 hours in a flow of 5% hydrogen to 95% argon gas at 0.15 slpm. At these temperatures the hydrogen reacts with and removes the organic contaminants on the surface [2,118]. After the substrates are loaded into the ultra high vacuum (UHV) system they are outgassed at 400 $^{o}$C for 0.5 hours prior to growth.

The MBE system used is a custom GENxplor MBE system purchased from Veeco and modified to extend the range of growth temperatures up to 1850 $^{o}$C. To deposit carbon a vertical e-beam source (EBVV 63-T4 supplied by MBE Komponenten) is used in combination with a high-purity pyrolytic graphite charge as the anode target for the production of the carbon flux. This source relies on thermionic emission to release electrons from a tungsten surface, which are subsequently accelerated by a potential difference of 5 kV for a current of 300 mA. The path of these accelerated electrons is directed by a perpendicular magnetic field towards the solid carbon source. This curvature prevents contaminants from the tungsten surface impacting the sample growth. Additionally, the e-beam can be raster-scanned to minimise the drilling of the beam into the surface, which would reduce overall carbon flux over time.

For the production of hexagonal boron nitride, a solid boron source and a nitrogen plasma were used. The nitrogen source consists of a high-efficiency radio-frequency (RF) plasma source using a fixed RF power of 550 W with a nitrogen flow rate of 2 sccm. The boron source was an EBVV 63-T4 vertical electron beam evaporator, directed onto a crucible containing pure boron crystals. During e-beam hBN growth the current was 50 mA with the electrons accelerated by a potential of 6 kV.

### 3.3 Photoluminescence

In this work photoluminescence was carried out on molecular networks of CA.M and PTCDI deposited on hBN and HOPG substrates. Photoluminescence is the emission of light (luminescence) from a material after it is excited through the absorption of incident photons. If an absorbed photon is of sufficient energy it will elevate an electron from a ground state to an excited state of the system. From here there are multiple potential processes which can result in luminescence, such as fluorescence and phosphorescence.

In the ground state all orbitals up to and including the highest occupied molecular orbital, shortened to HOMO, are occupied [119]. Photons of sufficient energy can be absorbed to excite an electron in the HOMO state to an orbital with energy at or greater than the lowest unoccupied molecular orbital (LUMO). HOMO orbitals are may be those with greater percentage p character, from which electrons

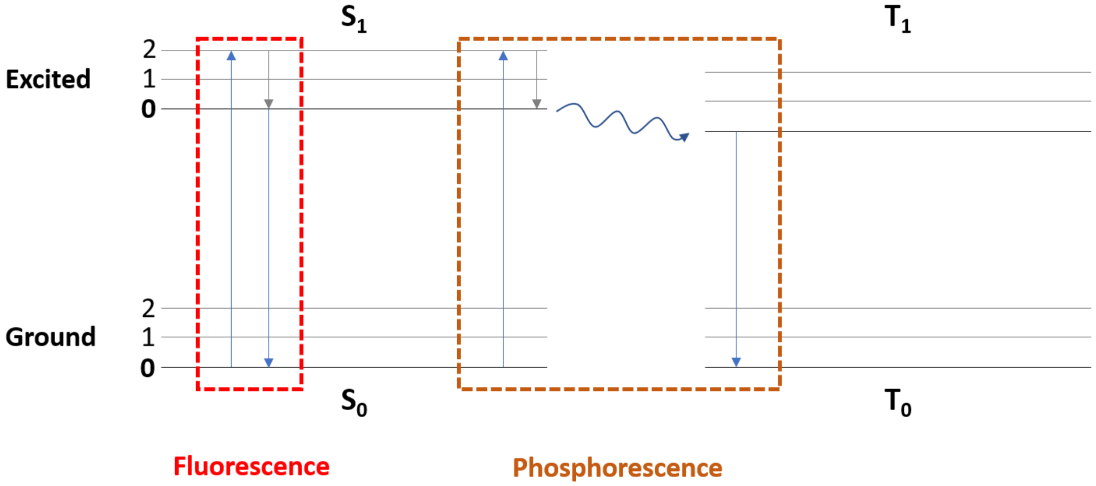

Figure 3.1 – Diagrams depicting the fluorescence and phosphorescence processes occurring between energy levels labelled as ground and excited. Three vibrational sublevels of the electronic states are depicted and it should be observed that the excited energy states of $T_1$ are lower in energy than $S_1$. The S labelled states are singlet, while the T labels refer to triplet states. Transition between singlet and triplet states is forbidden by symmetry, but may occur in practice due to the spin-orbit interaction between singlet and triplet states.

may transition to (LUMO) antibonding orbitals after photon absorption [119]. Incident photons of insufficient energy to excite an electron into a LUMO state may give rise to exciton formation. That is, the creation of a bound e-h pair. Excitons may also form from the relaxation from an excited state and may result in quenching of the fluorescent emission [120].

Vibrational levels, such as the levels labelled 0, 1, and 2 in Figure 3.1, subdivide the electronic states. These vibrations may consist of stretching, rotation, or torsion along single or multiple bonds of the molecular structure. The presence of the many distinct vibrations acts to create a broad structure of sublevels associated with each electronic level, which may appear as multiple sharp peaks or as broadening of the emission dependent on equipment precision.

As depicted in Figure 3.1, fluorescence transitions occur between singlet states. Electrons in a molecular orbital exist in one of two spin states, usually labelled up and down. The electronic states of each molecule can be distinguished as singlet or triplet in nature. Singlet states are those for which electrons can be paired with opposing spins, leading to a total spin of zero. Triplet states are those for which two unpaired electrons with the same spin are present. Transitions between states of different multiplicity, that is singlet and triplet, are forbidden. However, spin-orbit coupling between the distinct states results in the possibility of transition [119]. With a non-zero probability for an electron to be in singlet or triplet state it is possible for a molecule to undergo a transition between singlet and triplet states. This is referred to as intersystem crossing and plays an important role in phosphorescence.

Emissions from excited states can be reduced by a series of processes known as quenching. Quenching processes are separated into two categories, static and dynamic. Static quenching refers to the formation of a non-fluorescent complex between the quencher and the dye molecule [121]. The formation of the complex, which may occur when quencher and molecule come into contact, reduces the fluorescence intensity as a result of the reduced availability of fluorescent molecules. Dynamic quenching is a group of processes in which interactions between an excited fluorescent molecule and act to deexcite the molecule without luminescent emission from it.

The graphite substrates used in Chapter 8 quench fluorescence predominantly via an energy transfer mechanism [122]. This process was described by Persson and Lang to result from the coupling between electron-hole pairs in the metal quencher and the vibrating dipole of the excited molecule [123]. Energy transfers from molecule to metal at a rate dependent on the distance between the metal and the molecule. As a result, the presence of a spacer layer, or the suspension of the molecules above the metallic surface, will act to reduce the effect of the quencher and increase the intensity of the emission.

To measure fluorescence a source of photons with known excitation energy is directed onto a sample, and the wavelength dependence of the intensity of the emitted light is measured. Lasers are often used as sources, due to their highly monochromatic emission. The power can be controlled and the emission is spatially localised. The slight variance in the frequency of the laser light can be further reduced by the use of certain filters prior to direction onto the surface.

In our setup laser light is then directed onto the sample via a beam splitter and a focusing objective lens. The fluorescent emission from the surface is collected with an objective lens and directed through a beam splitter towards a diffraction grating, followed by a CCD detector. By rotating the diffraction grating, wavelengths within a particular range can be selected and directed onto the CCD collector, allowing for identification of the intensity of the emission within the wavelength range.

For this work the laser used is a Horiba Deltadiode 405L providing a 405nm wavelength with an average power of 10 µW over a spot size of approximately 2 µm. Individual spectra were plotted using OriginPro 8.5, which provides a peak fitting program. Peaks were fitted to the data with a Voigt profile due to the possible presence of homogenous and inhomogeneous broadening of the peaks. Multiple spectra can be used to map a surface with a precision down to the diffraction-limit of the system. The spectra are obtained at multiple points over a surface, usually defined by a rectangular grid of points. A false-colour image can then be generated by assigning colour dependent on the intensity, positions, or full width half maximum (FWHM) of a selected peak.

### 3.4 Raman Spectroscopy

Raman spectroscopy has been used in this thesis to estimate changes in the local lattice properties of graphene grown on hBN/sapphire substrates. In Raman spectroscopy a laser is shone onto a lattice or molecule, exciting it into a virtual energy state. Subsequently the excitation energy will be re-radiated as a photon. If the returned photons possess the same energy as the outgoing then no total change in vibrational state has occurred between absorption and emission and the result is termed Rayleigh scattering. The two alternatives to the more common Rayleigh scattering are depicted in Figure 3.2. If the re-emitted photon is of an energy greater than the original photon, then the atom that absorbed it will have started in a vibrational state higher than the ground state. As a majority of molecules or atoms in the lattice will populate the ground vibrational state at room temperature this form of

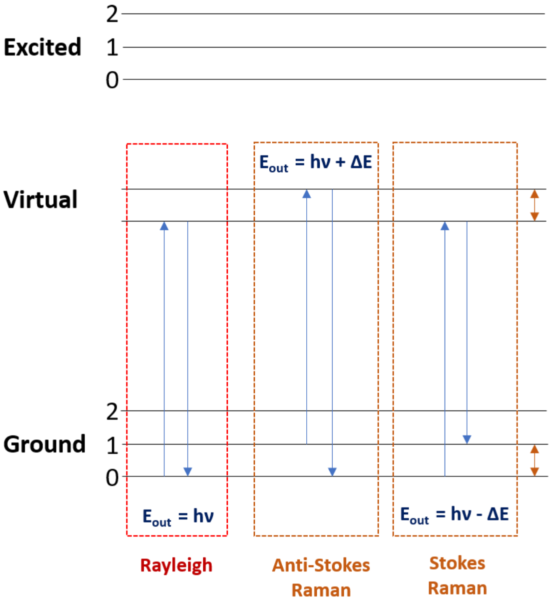

Figure 3.2 – Raman photon emissions arise from the excitation of electrons into virtual electronic states and the subsequent drop down into a ground state differing from that which the electron originally occupied. De-excitation into a different ground state to the original occupation, which is usually the 0 state at room temperature and below, occurs due to interaction with phonons in the lattice. As a result, the Stokes and Anti-Stokes processes, labelled in the diagram, provide a means for identifying properties of the atomic lattice under investigation. Small changes in the lattice, such as those originating from strain or doping, can be measured by investigation of changes in the emissions from Raman processes.

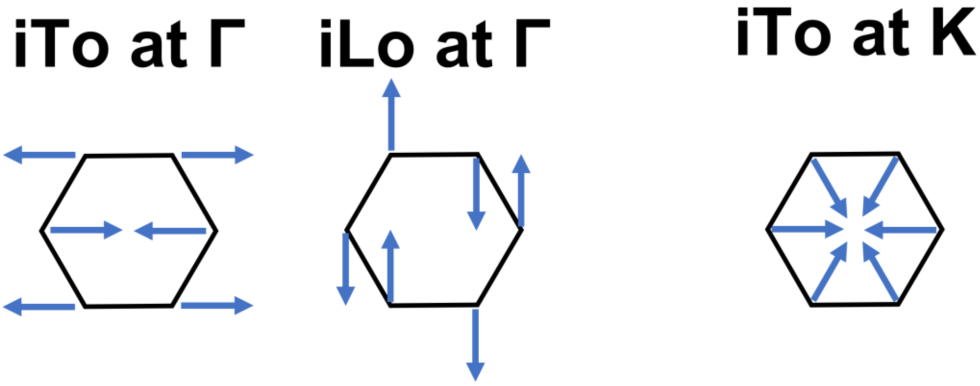

Figure 3.3 – Diagrams of the iTO and iLO tangential stretching phonon modes at the Γ point, and the iTO breathing mode at the K point. These modes contribute to the G and D peaks of the graphene Raman spectrum. The G peak arises from a first-order process involving the interaction of iTO and iLO phonons at the Γ point with an excited state. The D and 2D peaks result from more complex processes involving iTO phonons at the K point.

scattering, termed anti-Stokes Raman scattering, is uncommon and returns a relatively weak signal [124].

If the molecule or atom emits a phonon prior to emission of the captured photon the resulting photon will exhibit a loss of energy equivalent to the difference in a vibrational state of the molecule or lattice. This is by far the stronger of the two non-Rayleigh processes and is known as Stokes scattering [124]. In this work all measurements taken with Raman spectroscopy were confined to Stokes scattering and any references to Raman implicitly refer to the detection of the Stokes emission.

Not all vibrational modes of a lattice will result in a Raman emission as a result of selection rules arising from symmetry considerations. For graphene there are three peaks commonly observed in the spectrum, labelled G, D and 2D [125,126]. The G band is associated with the doubly degenerate iTO and iLO phonon modes at the Γ point, as depicted in Fig. 3.3 [127]. The G peak is the only Raman-active band observed in graphene that consists of a first-order process. The peak is non-dispersive and is seen at a wavenumber of ~1580 $\text{cm}^{-1}$. The position of the G band is sensitive to the number of graphene layers, as well as the level of doping and surface strain, providing a means to identify several key properties of a produced graphene surface [128–130].

The D and 2D bands involve iTO breathing mode phonons at the K point. The D band is a forbidden mode in pristine graphene, but can be activated by the presence of defects or edge states. This is due to the second-order or double resonance process that results in the band involving one inelastic scattering event from an iTo mode phonon and one elastic scattering event from a defect. Somewhat similarly to the D band, the 2D band arises from iTo phonons at the K point. It is distinct by requiring two iTO phonons, without need for a defect as part of the process. As a result, the presence of defects is not necessary for the activation of the 2D band, and 2D peaks are observed in the pristine graphene spectrum. Due to the symmetry of the graphene valence and conduction bands near the Dirac points the 2D peak can also be activated by a triple resonance process, which has been proposed to explain the relatively high intensity observed often observed from this emission [127].

As a result of the changes to the electronic structure from monolayer to multilayer graphene the number of allowed processes that may contribute to the double resonance and triple resonance bands increases, which allows for the identification the layer number by making use of the 2D band [127]. The D and 2D peaks are dispersive, with wavenumbers of 1350 $cm^{-1}$ and 2690 $cm^{-1}$ respectively for a 532 nm incident wavelength [127]. It has been shown previously that the density of point defects influences the relative intensities of the D and G peaks, allowing for an estimation of defect density in any graphene sample [127]. In the low defect density regime,

$$\frac{I_D}{I_G} = \frac{C(\lambda)}{L_D} \tag{3.1}$$

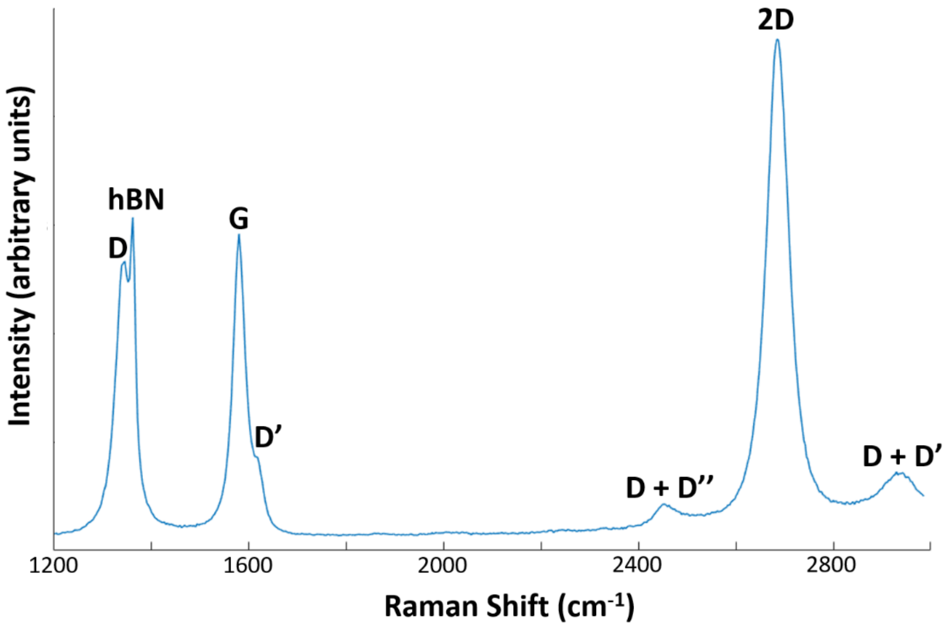

Figure 3.4 – An example of the Stokes emissions taken from a sample consisting of a single monolayer of graphene grown upon a hBN substrate. The position, relative magnitude, width, and number of peaks are influenced by numerous factors such as the presence of defects, strain in the lattice, and the number of graphene layers. This spectrum is consistent with defected monolayer graphene with the addition of a single peak arising from the hBN layer.

In which $I_i$ is the intensity of peak I, C is a constant dependent on the incident laser wavelength and $L_D$ is the average inter-defect distance. For a wavelength of 514 nm C(λ) = 102 nm$^2$. In addition to defect densities Raman is also capable of establishing the presence of strain in graphene [15]. Summerfield et al. [15] showed that for a graphene/hBN heterostructure the 2D peak splits into 3 distinct peaks when strain is present in the lattice. Two of these peaks exhibit red-shifting proportional to the strain, which allowed the authors to clarify the link between strain and the superlattice period [15].

The Raman spectrum of hBN consists of a single peak at 1365 cm$^{-1}$, with high quality hBN with a natural B isotope mixture exhibiting a FWHM of this peak around 30.0 cm$^{-1}$ [131]. For samples of graphene on hBN the thickness of the graphene layer is much lower than the penetration depth of the laser, and so the hBN emission is observed in the final spectrum as seen in Figure 3.4. This occurs even for samples where the monolayer coverage of graphene over the hBN flakes is at or in excess of 100%.

The LabRAM HR system from HORIBA Scientific at the Nanoscale and Microscale Research Centre in Nottingham was used to measure the data presented in this thesis. The system provides access to four lasers, with wavelengths ranging from NIR through visible to UV. After the selected laser has been scattered from the surface it is directed through one of several gratings into a CCD detector. For the Raman data presented in this work a 532 nm laser wavelength operating at ~4 mW or ~40 mW power was shone onto a sample with a spot size of ~1 µm. The emission was directed through a 600 lines/mm grating and the shift calibrated with a Si(100) reference sample.

### 3.5 X-Ray Photoelectron Spectroscopy

X-ray photoelectron spectrscopy (XPS) makes use of the photoelectric effect to analyse the binding energy values for the surface of a sample. The binding energy values obtained correspond to particular elements on the surface, and the chemical environment experienced by those elements. As a result the technique provides for a relatively quick, unintrusive manner for the identification of the chemical constitution of a sample near the surface.

Step by step the technique first involves the production of x-rays of a known energy or energy range. This is commonly achieved by the bombardment of an anode material with high energy electrons, such as aluminium. X-rays produced in this manner exhibit characteristic energies of the element from which they were created. Commonly used are x-rays obtained from the Al Kα emission with energies of ~1.5 keV. Monochromation of the light collected from the bombarded anode is carried out to select for these x-rays and the light is then directed onto the surface of the sample to study. Simply, the light interacts with electrons in the sample with energy enough to eject the electrons. Some of these electrons will exit the surface of the sample without undergoing inelastic transitions along the travel

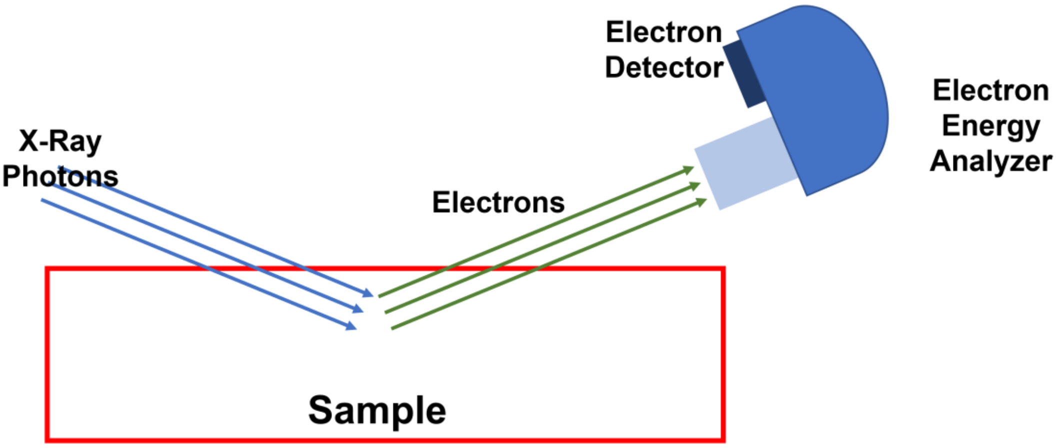

Figure 3.5 – An example XPS setup is presented. Incoming x-ray photons incident upon the sample kick out electrons from orbitals of the surface with binding energy below that of the photons. The electrons are collected and passed through an electron energy analyser (EEA), which filters out electrons with specific energy ranges to send on to the electron detector. By varying the range of the EEA a spectrum is obtained to be plotted as a graph of counts against energy.

path and will subsequently be collected and directed into an electron energy analyzer (EEA). From here the energy of the electrons can be identified and electrons counted as a function of energy. A diagram of this process is presented in Fig. 3.5. The observed energies can then be related to the binding energy with the work function of the spectrometer and the incident x-ray energy, both of which will be known quantities. The result of this are then displayed as graphs of electron count intensity against binding energy for subsequent analysis.

The method primarily delivers results deriving from the surface of the investigated material due to the influence of the material on ejected electrons passing through. This is characterised by the effective attenuation length of a material, λ, as per the Beer-Lambert relationship which goes as follows,

$$I = I_0 e^{-\frac{d}{\lambda}} \tag{3.2}$$

Where the drop off in intensity of electrons emitted from depths greater than d are given as a function of the effective attenuation length. If the electron collector is angled away from the normal of the surface the equation can be modified where the $d$ term is replaced by $d\, cos(\theta)$. As a result of this change the intensity is seen to drop off greatly as the angle of the collector is shifted from the normal, reducing the rate at which electrons are collected from deeper into the sample. For most XPS setups the collection angle differs significantly from the normal.

At the University of Nottingham where these studies were carried out a Kratos AXIS ULTRA DLD device is available. Though multiple sources are present in the device all data presented here makes use of monochromated Al Kα emissions as mentioned previously. The pressure of the measurement chamber is kept at or below $5 \times 10^{-9}$ Torr to minimise the scattering of ejected electrons prior to detection, which is standard procedure for most XPS devices. The sorting of electrons by energy is carried out with a hemispherical analyser before detection and counting via a triple channel plate and delay line detector.

### 3.6 Sublimation of PTCDI

The deposition of PTCDI was carried out using sublimation in a dedicated vacuum system. Sublimation involves the heating of an organic source material for the production of thin films. To achieve this a heated source, substrate holder, and high vacuum environment are required. First the sample must be cleaned prior to loading into the system, to prevent the accumulation of lingering contamination in the vacuum system. This is achieved here via one of two methods, depending on the substrate to be used. For hBN flakes exfoliated onto silicon dioxide the surface can be annealed with a blow torch to evaporate any organic residue left behind by the tape. The temperatures produced by the blowtorch are too high to avoid damaging the graphite surface, so the HOPG substrates were annealed in a tube furnace as described in Section 3.2.

The vacuum deposition system is depicted in Figure 3.6 as a diagram and with a photograph of the outside of the chamber. Once prepared the samples were loaded onto the substrate holder which was then inserted into the system in the position indicated. The holder consists of a ceramic plate on which

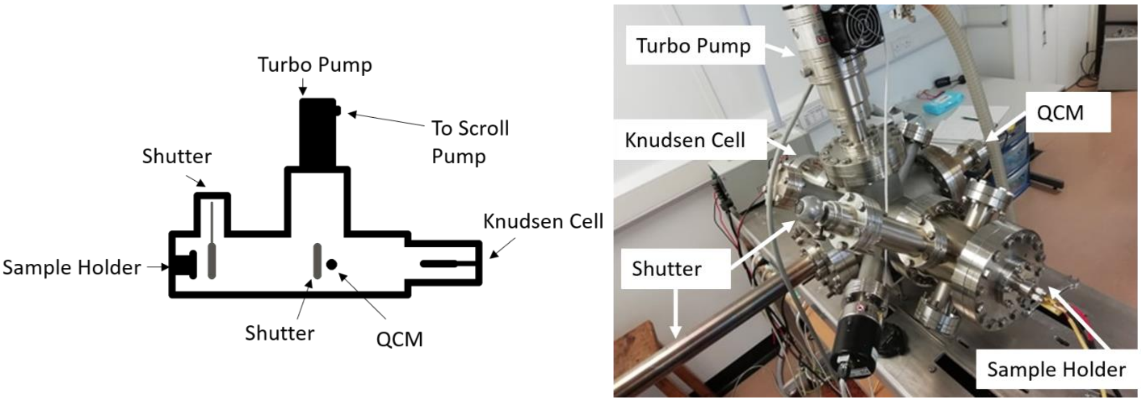

Figure 3.6 – A diagram and photograph of the vacuum setup used to deposit PTCDI for the samples used here. Vacuum conditions of 5 x $10^{-7}$ mbar are obtained prior to deposition. The sample holder contains a heater to allow for substrate heating prior to and during the growth. The QCM monitor was used to establish the deposition rate before opening the shutter to perform the deposition.

the samples are pinned, underneath which lines a tungsten sample heater. Once loaded into the system a vacuum environment of 5 x $10^{-7}$ mbar was obtained using the combination of a scroll pump and a turbo molecular pump. The vacuum chamber itself contains a single Knudsen cell, a quartz crystal microbalance (QCM), and two shutters.

After having achieved a vacuum environment, the samples were annealed to evaporate organic residues present on the surface. For hBN and graphene flakes temperatures of 500 °C and 200°C respectively were used to anneal for one hour, as read by a C-type thermocouple set within the sample holder. If CA.M was present on either substrate only 50 °C to prevent loss of the molecular layer. During growth the substrate temperature was held between room and 150 °C to influence the growth properties of the PTCDI. As with annealing the substrate temperature was capped at 50 °C when CA.M layers were present.

The Knudsen cell filled with PTCDI was heated to 442 °C for deposition. The QCM monitor was checked at regular intervals until the deposition rate of PTCDI had stabilised at around 0.2 nm/min. The dual shutters were then opened for a precalculated period of time to control the dosage to the substrate. Once the deposition was complete the shutters were closed, and the chamber left to cool. The chamber could then be opened, and the samples removed for analysis.

### 3.7 Immersion Deposition of CA.M

CA.M is a molecular network of cyanuric acid and melamine that has been previously shown to deposit in single monolayers on the surfaces of hexagonal vdW crystals and other materials [132,133]. Here an immersion deposition method previously demonstrated by Korolkov et al. enabled the production of monolayers of CA.M on hBN substrates [112].

CA.M deposition was carried out on 1cm$^2$ chips of Si/SiO$_2$ laden with hBN flakes and 1cm$^2$ chips of HOPG via immersion. When not in use the melamine and cyanuric acid solutions were stored with molar concentrations of 160 µM in water. For the immersion a solution of 8 µM of cyanuric acid and melamine was prepared by mixing the bulk solutions of CA and M with water at a 5:5:90 ratio. After preparation the solution was used for up to one hour after preparation, after which aggregation of CA and M prevents use for future immersions.

The immersion was then performed by holding the prepared substrate beneath the water line of the solution before removal and drying with a N$_2$ air spray. As described by Korolkov et al. sixty seconds of immersion is enough to consistently deposit one monolayer of the CA.M network onto the surface of the hBN/Si samples [112].

### 3.8 Theoretical and practical AFM

Atomic force microscopy (AFM) is commonly used in the study of crystalline surfaces for its atomic scale precision. Here AFM was used to analyse properties of the graphene and hBN sheets such as domain size, edge directions, and coverage. In this Section a simple theoretical understanding of tapping mode (amplitude modulated AFM) and conductive AFM will be described, alongside the various parameters that can be mapped in order to produce images.

In AFM the interactions between an atomically sharp tip brought into close proximity with a surface are measured to estimate the morphology and some other properties of the surface. These interactions include the collective of dipole interactions known as van der Waals forces and the Pauli repulsion resulting from the proximity of fermions. The combination of these two sets of processes are summarised in the Lennard-Jones potential, the equation for which is shown below,

$$V(r) = 4\varepsilon\left(\left(\frac{\sigma}{r}\right)^{12} - \left(\frac{\sigma}{r}\right)^{6}\right) \tag{3.3}$$

The first of the two terms accounts for the Pauli repulsion and the greater power dependence relative to the second term shows that the repulsion term will become more significant at smaller distances, r. The second term accounts for the van der Waals interactions, which are long range forces when compared to the repulsion. ε and σ terms can be understood as defining the depth and position of the potential well described by the equation, respectively. A depiction of the potential is presented in Figure 3.7, showing two distinct regimes. In the first regime the differential of the potential is negative, so it is often labelled the repulsive regime. In contact-mode AFM the tip travels across the surface at a contour of constant repulsive force at a distance consistent with this regime.

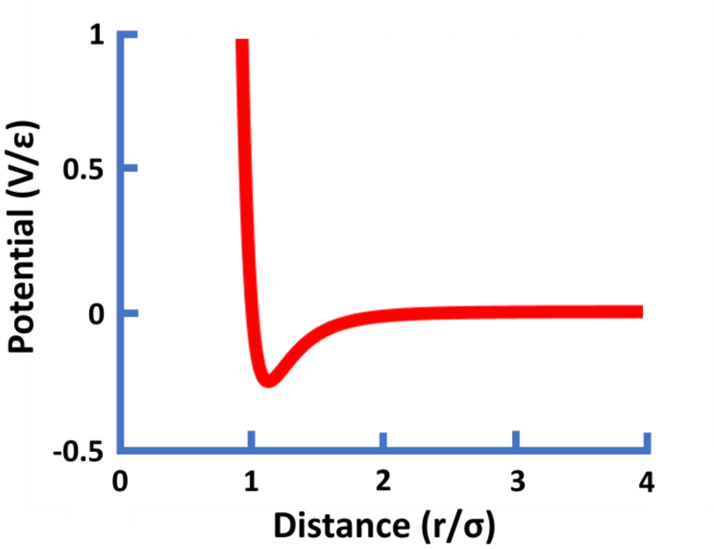

Figure 3.7 – A depiction of the Lennard-Jones potential. At large distances the van der Waals interactions dominate, known as the attractive regime in AFM. As the distance is reduced a transition about the minimum is observed whereby the Pauli repulsion term dominates, usually labelled as the repulsive regime. Contact-mode AFM is exclusively carried out in the repulsive regime, whereas tapping-mode AFM usually occurs in the attractive regime.

In tapping-mode a cantilever with an integrated pyramidal probe, usually composed primarily of silicon, is oscillated above the surface to be imaged at a distance consistent with the attractive regime of the Lennard-Jones potential. The mechanical system can be approximated as a damped driven oscillator with external forces originating from the surface. It can be described by the following equation,

$$m\frac{d^2z}{dt^2} + \gamma\frac{dz}{dt} + k(z-d) = F(z) + F_0cos(\omega t) \tag{3.4}$$

Where $z$ is the distance between probe and sample, and $F(z)$ is the force felt by the probe due to the sample surface. $d$ is the free amplitude of the oscillator and $m$ and $\gamma$ are defined as the mass and damping coefficient of the system, respectively. By considering small oscillations, $z'$, about the equilibrium position, the following equation is obtained,

$$m\frac{d^2z'}{dt^2} + \gamma\frac{dz'}{dt} + \left(k - \frac{dF}{dz}\right)z'(t) = F_0cos(\omega t) \tag{3.5}$$

This equation is the same as for the damped driven oscillator before, but with an effective spring constant defined as,

$$k_{eff} = k - \frac{dF}{dz} \tag{3.6}$$

The latter term here modifies the spring constant of the system by the force gradient above the surface. This results in a resonant frequency shift proportional to the gradient of the external forces so long as the amplitude of this gradient is much smaller than the spring constant. Height images can therefore be obtained by moving the oscillating tip laterally over the surface, and keeping the driving frequency and excitation amplitude constant, such as in AM-AFM. This allows for the measurement of the height of the surface and the phase shift. By considering the relative phase lag between the driving force and the system and the cantilever response it can be shown that the shift in phase can be written as,

$$\varphi = \tan^{-1}\left(\frac{m\omega\omega_0}{Q(k_{eff}-m\omega^2)}\right) \tag{3.7}$$

Where $Q$ is the quality factor of the system, $\omega_0$ is the resonant frequency in free air, and $\omega$ is the resonant frequency near the surface. If the frequency of the system is being held constant the phase lag will shift as the tip is brought in close to the surface. Magonov et al. go further and established that the extent of the phase shift is partially dependent on the average length of time in a period of the oscillation that the tip interacts strongly with the surface [134]. This interaction period is described as likely to be dependent on the stiffness of the tip and sample. Similar arguments can be presented to show the dependence of the phase shift on the adhesion, friction and viscoelasticity of the samples [134]. Here phase imaging was used to distinguish between materials where surface coverage is below a whole monolayer, and for identifying amorphous aggregates of carbon and boron nitride. For the majority of images presented tapping mode was used. These images were taken using NuNano Scout 70 tips, with stiffnesses of 2 N/m in an Asylum Research Cypher S system.

Two tapping mode imaging regimes were observed in these samples, corresponding to the attractive and repulsive imaging regimes described by García and San Paulo in 1999 [135]. In their work they discussed the existence of two distinct imaging regimes characterised by the overall forces applied to the tip during each period of its oscillation. The regimes can be identified during imaging by the average phase lag observed as an overall attractive regime will lead to the phase obeying $\varphi > 90^{\circ}$. In contrast an overall repulsive regime, which is generally obtained with lower free oscillation amplitudes, leads to $\varphi < 90^{\circ}$. In this work the majority of images were obtained in the attractive regime, though it is worth noting that a greater contrast is observed in phase images between HOPG and hBN in the repulsive regime. In the repulsive regime as described by García the tip is only in intermittent contact with the surface, differing from the continuous contact characterised by contact mode AFM [135].

Conductive AFM and contact mode were used to provide lattice resolution. In contact mode AFM the tip is brought 'into contact' with the surface, whereby contact is defined such that the force experienced by the tip is repulsive at all times. As the cantilever is moved across the surface it is deflected by the changes in the surface height and these deflections are outputted as the false-colour image. The tip is held on the surface via a feedback loop that holds constant the force against the tip. Due to the strong gradient of the forces exerted on the tip in this system it is possible to discern atomic resolution on reasonably flat surfaces.

Conductive AFM works similarly to contact mode, with the feedback loop holding the deflection force constant and deflection images being obtained. However, conducting tips were used, such as the NuNano Spark 70Pt tips used here. These tips are manufactured similarly to the Scout 70s but, are additionally coated with a thin platinum conductive layer. With these tips a voltage can be applied during scanning, and the resulting current of the system recorded to establish the resistivity of the surface. Electronic features of the surface show up strongly in these current images, such as the moiré superlattice arising from graphene/hBN heterostructures. With the use of conductive imaging on the Asylum Research Cypher-S system it is fairly simple to obtain images of the lattices.

After obtaining these images they were analysed by several programs, as appropriate to the required final results. The Gwyddion analysis software is excellent for flattening images and aligning rows to easily identify features in the false-colour images [136]. Small changes to the tip can arise as it is moves across a surface, often leading to a small misalignment in the height of adjacent rows in the final image. For the most part this can be simply resolved by removing the difference in the average values of each row. Similarly, flattening allows the removal of any background plane that may obscure finer features of the surface. Such planes can arise from a slightly tilted sample, or large-scale height variations of the surface greater than the size of the image. Removal of these planes can be performed by a 2D difference of least squares on a surface about a pivot point defined as the centroid of the image.

# Chapter 4: Surface Morphologies of MBE-grown hBN

## 4. Overview

In Chapter 2 several properties of the hBN lattice were identified that make it an excellent substrate or capping layer in combination with mono- or few-layer graphene and other 2D materials. A lack of dangling bonds, and high chemical stability contribute to minimise the material's influence on the graphene in any resultant device, whilst acting to preserve and prevent contamination in device structures. The similar lattice constants of graphene and hBN introduce interesting electronic modifications to the graphene, and aid in the epitaxial growth of one upon the other. Prior studies have proven the viability and potential quality of hBN grown on graphite and a variety of metallic substrates. Discussed in Chapter 2, CVD growth of hBN on Cu has shown the potential for the fabrication of van der Waals heterostructures on metallic, catalytic substrates. High temperature molecular beam epitaxy (HT-MBE), carried out by the Nottingham group, provides a method for the epitaxial deposition of thin hBN layers on a non-catalytic HOPG surface.

In this Chapter further investigation of the HT-MBE method of growth is reported. The morphology of the hBN on graphite surface is analysed, and the controllability of the growth process determined. Samples were grown as in Chapter 3, with a range of substrate temperatures and growth times, and analysed with AFM. In this Chapter the dependencies of the hBN monolayers on temperature, time, and morphology of the HOPG substrate are investigated, and suggestions for the optimisation of the growth to produce these heterostructures are made from these results.

## 4.1 Growth Parameters

HOPG substrates for the deposition of hBN were cleaned and loaded into the MBE vacuum system as described in Chapter 3. The e-beam source described in Chapter 3 was used to deposit boron and the relevant growth parameters varied between samples are shown in Table 4.1. All other parameters of growth were kept the same for each sample and are described in Chapter 3. Notably there are no previous reports of the use of the described e-beam source for boron deposition, and the results presented in this Chapter show the validity and quality of the source for these purposes. Six samples are listed in Table 4.1, with each identified by a roman numeral. The first set of three were kept at a constant substrate growth temperature of 1250$^{o}$C, and were varied in growth time from 20 to 60 minutes as shown. The substrates of the second set of three were held at different temperatures during growth, within the range 1080$^{o}$C and 1520$^{o}$C, using a constant growth time of 40 minutes. Sample II is included in the growth temperature-varied set, representing the 1250$^{o}$C substrate temperature.

**Table of Samples**

| Sample Name | Temp ($^{o}$C) | Time (mins) | Group |
|---|---|---|---|
| I | 1250 | 20 | Time |
| II | 1250 | 40 | Time, Temperature |
| III | 1250 | 60 | Time |
| IV | 1080 | 40 | Temperature |
| V | 1390 | 40 | |
| VI | 1520 | 40 | |

Table 4.1 – A list of all samples used in this Chapter is presented. I-III were grown at the same substrate temperature with differing growth times. The growth times of IV-VI plus II were all 40 minutes and differ from each other by the substrate temperature during growth. All other growth parameters were the same for all samples.

After removal from the vacuum system each sample was measured with X-ray photoelectron spectroscopy (XPS) to identify contaminants and determine the purity of the grown material. Identified contamination was minimal, and the XPS data is presented in Appendix 1 for further perusal. At this point the samples were imaged with AFM to obtain the data presented below.

## 4.2 AFM Methodology

Tapping and conductive modes have been used to identify different features of the surfaces. Tapping mode images are used for the identification of features much larger than the atomic lattices, up to several microns. The phase images obtained simultaneously to the topography with tapping mode prove valuable for distinguishing the two materials. In topography the small difference in height and limited contrast between the hBN and graphite monolayer constrains identification. Phase images provide a means of distinguishing the two different materials, as described in Chapter 3. Conductive mode imaging has also been used to distinguish graphite and hBN and to obtain images with lattice resolution. These images provide a means for comparisons between the orientations of lattice vectors and the direction of growth edges and grain boundaries. Additionally, small differences in resistivity resulting from the moiré superlattice can provide enough contrast in conductive images to resolve these structures. Contact topography images were obtained simultaneously to the current channel images using the conductive mode.

For the images presented in the figures below, lighter colours refer to increased height in topographic images and higher resistance in conductive images. Profiles have been presented from topography images to display surface morphology at specific points.

### 4.3 Common Features Across Samples

Several features of the growth are common to all samples, though the properties, such as coverage, facet orientation and morphologies, differ depending on substrate growth temperature and time. For example, monolayers of hBN grow primarily from steps in the graphite surface. Examples of these steps and other features are identified by AFM, such as the images presented in Figure 4.1, and their dependence on growth parameters is discussed in more detail in subsequent Sections.

Incomplete monolayers of hBN have grown from monolayer and multilayer steps on the graphite surfaces of the samples. Figure 4.1 a) and b) show epilayers of hBN grown from monolayer graphite steps. The epilayers are terminated by edges parallel to the direction of the step, or triangular facets

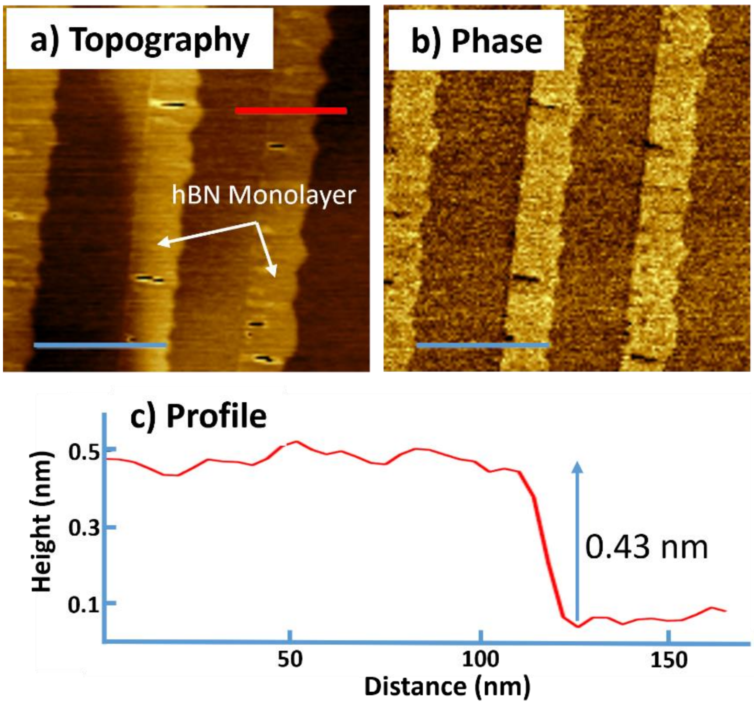

Figure 4.1 – Monolayer sheets of hBN are common to all samples. a) and b) show topographic and phase images, respectively, of the same position on sample V with scale bars of 200 nm. Three epilayers have grown from three monolayer steps in the graphite surface. The phase response shows a significant contrast between (lighter) hBN and (darker) graphite, making it simple to distinguish the two materials. The profile in c) was taken from the topographic image a) and shows a monolayer height of 0.43 nm between the hBN and graphite.

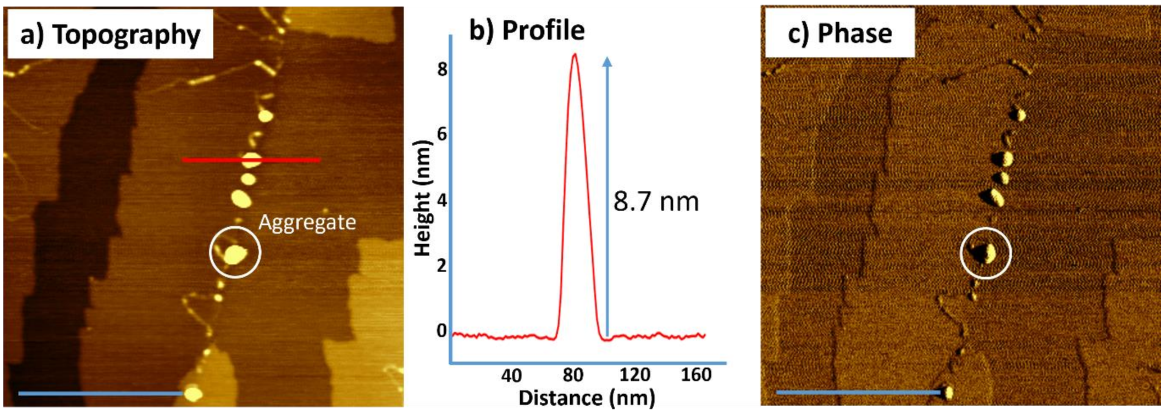

Figure 4.2 –The AFM images a) and c), with scale bars of 200 nm, have been selected to show the formation of aggregates from a monolayer step. The aggregates appear as bright points in the topography with significant heights, such as that exhibited by the profile in b). The vertical scale of the aggregates exceeds the monolayers by an order of magnitude.

depending on the misorientation of the dominant growth edge from the graphite edge direction, as will be discussed in more detail. The epilayers form from the nucleation of multiple domains of hBN along the step which eventually meet or merge as growth continues. Step heights of 0.43 ± 0.02 nm are obtained from topography images, as in Figure 4.1 c). A variety of factors, including operational parameters and choice of cantilever, have been shown to impact the apparent height of monolayers from tapping-mode images such as that above [137]. Changes in the chemical interaction between the tip and surface as the tip crosses over two materials, such as the hBN and graphite here, results in changes to the apparent height of the step between the materials [138]. In the images presented here an increase relative to the expected true height of 0.35 nm is measured [62]. Lai et al. discuss how the chemical interactions of tip and surface could lead to an increase in apparent height where the relative Hamaker constants of the two materials is greater than one [137]. If this is the case here a dependence of the apparent height on the sharpness of the tip and operational parameters of the system will have arisen, leading to the observed changes in the step height.

In addition to the monolayer sheets, amorphous aggregates are formed predominantly at the graphite steps. Examples of aggregates on a step are depicted in the topography and phase images of Figure 4.2 a) and c). These aggregates are characterised by heights on the order of several nanometres, as shown in Figure 4.2 b), and a minimal presence on terraces at most temperatures. Rows of aggregate and monolayer formation can also be observed running along the graphite surface without a step present; this is believed to arise at grain boundaries in the graphite surface. As will be shown later the density of aggregates varies with both growth temperature and time. Temperature also influences where the amorphous structures are observed. At the lower growth temperature sample, IV, amorphous aggregates are nucleated on graphite terraces away from the steps.

On sample IV triangular islands of hBN have nucleated on graphite terraces, as shown in Figure 4.3 a). The edges of these islands align with two orientations observed on each terrace, with each orientation distinguished by a rotation of 180°. Triangular islands of hBN have previously been reported on other

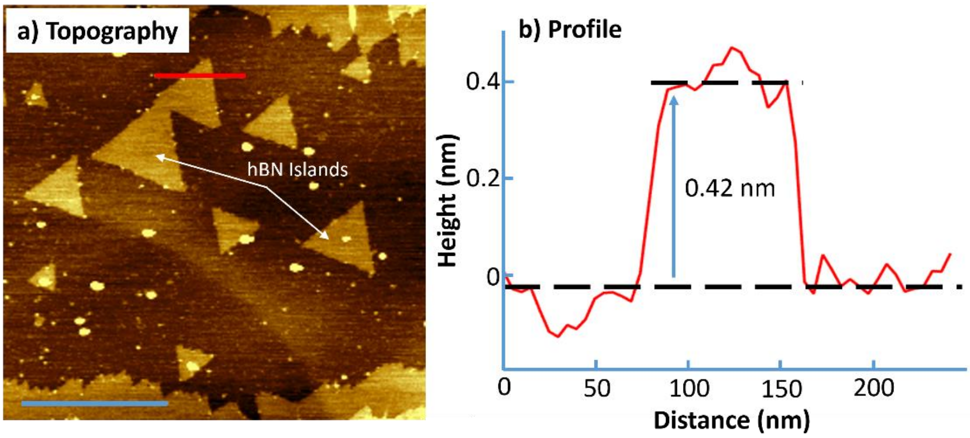

Figure 4.3 – a) topographic image of a graphite terrace on sample IV, on which can be seen multiple hBN islands. Islands nucleated on terraces are seen on other samples but are considerably less common. The triangular islands can be seen to follow one of two orientations, differing by a 180° rotation. The profile in b) was taken across one of the islands and shows a height of 0.42 nm, consistent with the hBN monolayer observed in Figure 4.1.

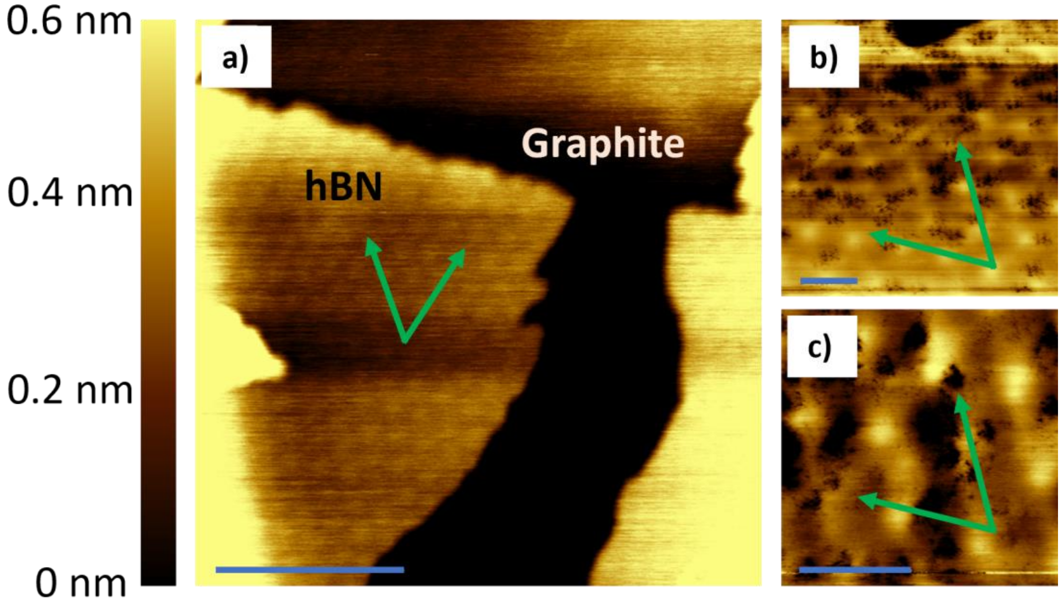

Figure 4.4 – Images depicting examples of moiré patterns observed on samples of hBN grown on graphite. a) shows a monolayer of hBN taken with tapping mode AFM with a present moiré period of 16.7 nm. The scale bar of the image is 100 nm. b) and c) are 100 nm and 50 nm conductive images respectively with scale bars of 20 nm. The measured moiré patterns of b) and c) are 15.2 nm and 17.6 nm respectively. Green arrows on all images are provided to identify the direction of the moiré lattice vectors.

substrates, and are explained by the dominance of one of the zigzag edges during growth [139]. Isolated islands of hBN are observed on the samples grown at higher substrate temperatures, but with greatly reduced frequency.

Moiré superlattices can be observed on epilayers of hBN on the graphite substrate. The patterns on these samples, where observed, often exhibit a moiré period of 13.5 nm. This is the value expected for aligned incommensurate hBN on graphite, as described in Chapter 2. Larger moiré periods than 13.5 nm are depicted in Figure 4.4, obtained by tapping mode as in a) and conductive mode in b) and c). These extended patterns can be explained by the accumulation of strain during cooling as described in Chapter 2.

## 4.4 Dependence of Morphology on Growth Time

The dependence of the morphology of monolayer hBN on growth time was investigated. Samples I, II, and III were prepared, with growth times progressing from 20 minutes to 60 minutes at a constant growth temperature of 1250°C. The average width of the hBN sheet from the step edges provides a method from which the coverage can be estimated, while simultaneously providing a measure of the scale of the hBN domains.

In order to estimate the surface coverage the area of a hBN epilayer along a graphite step of known length is measured. The area divided by the length of the step provides the average sheet width of that epilayer. This measurement has been taken from just over 400 steps identified on 15 images taken across the 3 samples I to III, in order to provide an accurate measurement of the average sheet width. This method is necessary due to the non-uniform width of the epilayer. Misalignment of the leading growth edge of the hBN from the direction of the graphite step results in triangular

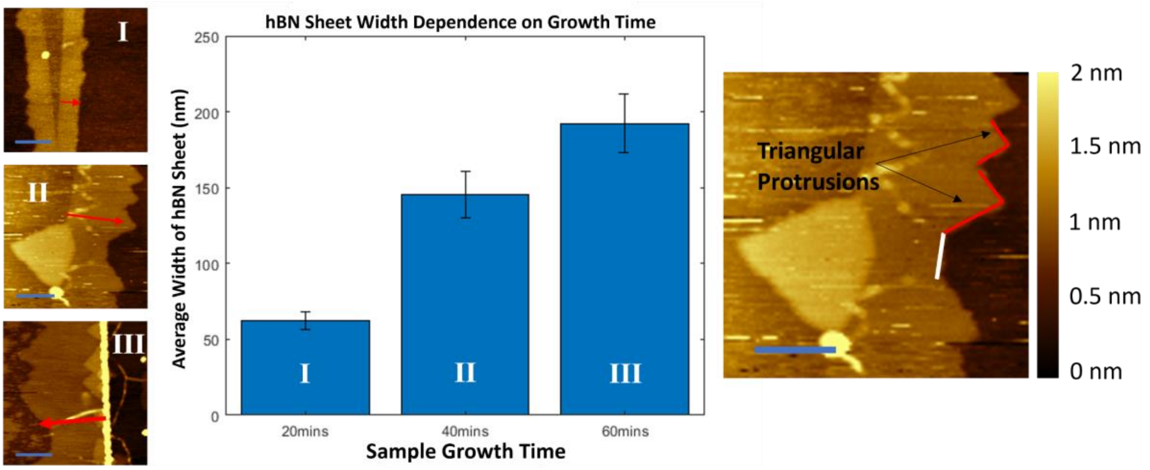

Figure 4.5 - Histogram of the observed sheet width dependence on growth time for 20 minutes (I), 40 minutes (II), and 60 minutes (III). The sheet width is observed to follow an approximately linear increase over the temperature range. This has been highlighted with AFM images taken from each sample, all with scale bars of 100 nm. Red arrows indicate the obtained average width for each image. The image on the right is the same image presented for sample II and has been marked to identify what has been referred to in this Chapter as the triangular protrusions.

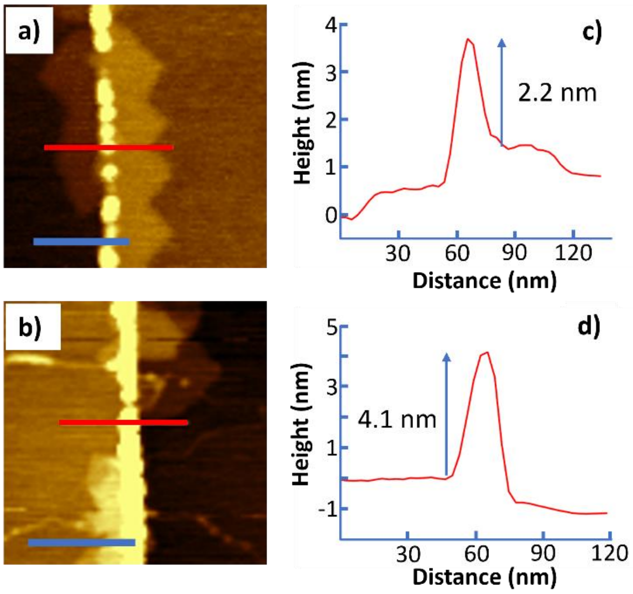

Figure 4.6 – AFM images a) and b) have been taken from samples I and III. The images show lines of aggregates formed along multilayer steps running vertically down the images. Scale bars are 100 nm and profiles of the aggregates have been taken along the red lines. These profiles are depicted in c) and d), shown adjacent to the corresponding AFM images. A substantial increase in height of the aggregates is noted between the two samples consistent with the increased growth time from I to III.

protrusions, such as that identified in Figure 4.5. By taking the average area of the hBN protruding from a graphite step the non-uniform width of the step arising from the triangular extensions was taken into account. The application of this method to samples I, II, and III results in the values presented in Figure 4.5. An approximately linear trend is observed across the three samples, implying a constant growth rate of the monolayer.

Figure 4.6 shows that aggregates on the steps also increase in scale with the increase in growth time. Images a) and b) are centred on a line of aggregate material found on multilayer steps for samples I and III. Profiles of these images, presented in c) and d), show an increase in height of the aggregate material from sample I to III. Measurements of the average aggregate cross section taken from ten steps on each of samples I, II, and III show a linear trend. On sample I the aggregate cross section is observed to be 29 ± 6 nm$^2$, with sample II and III exhibiting cross sections of 63 ± 11 nm$^2$ and 84 ± 15 nm$^2$, respectively.

## 4.5 Temperature Dependence of the Growth

Growth temperature can strongly influence epitaxial growth since various chemical and physical energy barriers must be overcome for the formation of clean, regular structures. To investigate the temperature dependence of growth, samples were produced with substrate growth temperature ranging from 1080$^{o}$C to 1520$^{o}$C, each grown for 40 minutes as described in 4.1. The dataset of samples II, IV, V and VI cover this temperature range, providing all images and subsequent data for this Section. Several features of the surface, namely sheet width, aggregate presence, and domain shape, were observed to vary with substrate growth temperature. Each is reported below as a separate subSection.

### 4.5.1 Sheet Width Variation with Substrate Growth Temperature

In Figure 4.7 a) average estimates of the sheet width are measured over a range of growth temperatures. From this we see that at growth temperatures between 1250$^{o}$C and 1390$^{o}$C a sizeable drop in the sheet width occurs. This reduction in sheet width likely arises from the re-evaporation of adsorbed species on the surface prior to incorporation in the growing epilayers. For the purposes of growing large domains, a growth temperature of 1250$^{o}$C or lower would be preferred. However, as will be seen in 4.5.2, these lower growth temperatures lead to the production of larger volumes of aggregate material.

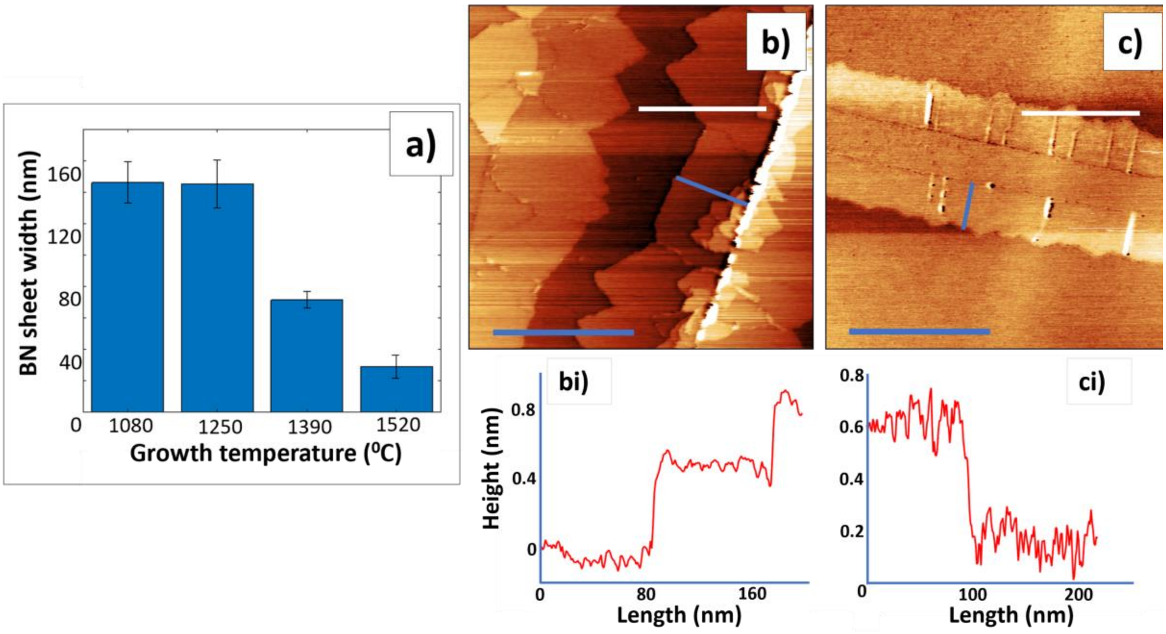

Figure 4.7 – Chart a) displays the hBN sheet width as measured from the graphite step for four samples with different substrate temperatures during growth. Raising the temperature of the substrate during growth increases the evaporation of surface material prior to incorporation in the hBN sheets, thus reducing the resulting width of the hBN sheets. Contact topography images b) and c) with 200 nm scale bars from samples II and V, respectively. Passage of the tip over steps may lead to changes in the tip, leading to the horizontal bands seen in the images. The step widths without triangular extensions are depicted by the blue lines here. They are 110 nm and 66 nm, respectively. Surface b) shows that triangular extensions can form a significant fraction of the monolayer sheet coverage. A more accurate measure of sheet width as depicted in a) is found from the average area divided by the length of the graphite step from which the growth is nucleated.

### 4.5.2 Aggregate Reduction with Temperature

The volume of aggregated material at a graphite step has been obtained from tapping mode topography images using the Gwyddion program described in Chapter 3 [136]. Firstly, the data was visualised by false colour mapping with a scale dependent on the measured height of the surface at each point. Next, the height of the surface was zeroed on the upper terrace of a step. Following this the aggregate on the step was selected by threshold masking the surface and the volume of masked material subsequently measured by taking the area of a pixel and multiplying by the height at the position of the pixel. In addition to a temperature dependence of the aggregates AFM images showed

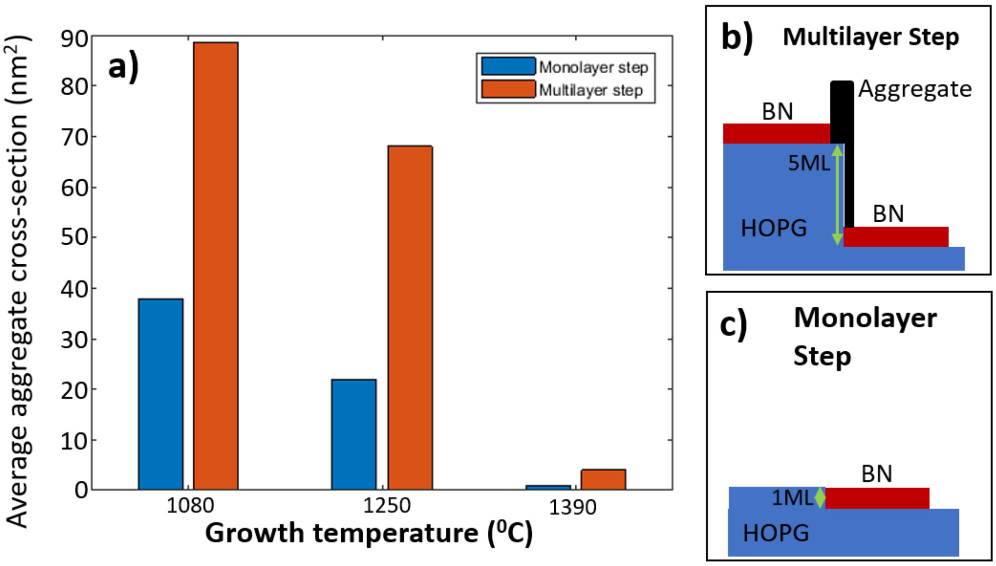

Figure 4.8 – A bar chart, a), displaying the average aggregate presence on monolayer and multilayer steps at three different growth temperatures. The aggregate cross-Section value is obtained by dividing the volume of measure material by the length of the step over which the measurement is taken. The monolayer steps exhibit significantly reduced aggregate material when compared to the multilayer steps on the same samples. The volume of material also correlates negatively with the growth temperature of the samples. This is to be expected due to the $\sim k_BT$ energy dependence for the re-evaporation of particles from the surface. b) and c) display diagrammatically the present understanding of how material is structured around steps of differing heights on the surface.

a significant difference in aggregate material accumulation depending on the step height. The presence of large aggregates makes accurate estimation of the number of layers in steps difficult. As a result of this limitation the dataset distinguishes only between monolayer and multilayer steps in the graphite surface.

Figure 4.8 a) displays the results of this investigation. The aggregate cross-Section referred to in a) is the volume of aggregate material on a step normalized by the length of the same step. It can be seen from these results that monolayer steps consistently lead to a lower aggregate presence compared to multilayer steps.  Higher growth temperatures also contribute to the reduction of aggregate presence from monolayer and multilayer steps.

Diagrams b) and c) depict the shape of the surface at each step. At the multilayer steps, such as that shown in b), monolayers of hBN have nucleated from the lower side of the step. Monolayer sheet formation is also observed above the step from the amorphous aggregate as seen in the multilayer height step depicted in Figure 4.6 a). The aggregate is depicted as extending from the bottom to the top of the step as the multilayer nature of the graphite step likely contributes to the formation of the aggregate. Differences in the growth of hBN sheets from steps of different heights are discussed in Section 4.6.

### 4.5.3 Growth Edge Direction Dependence on Temperature

Properties of the edges of 2D materials significantly alter the properties of the resulting 2D structure [140]. In the growth of 2D structures the direction of the dominant growth dictates the morphology

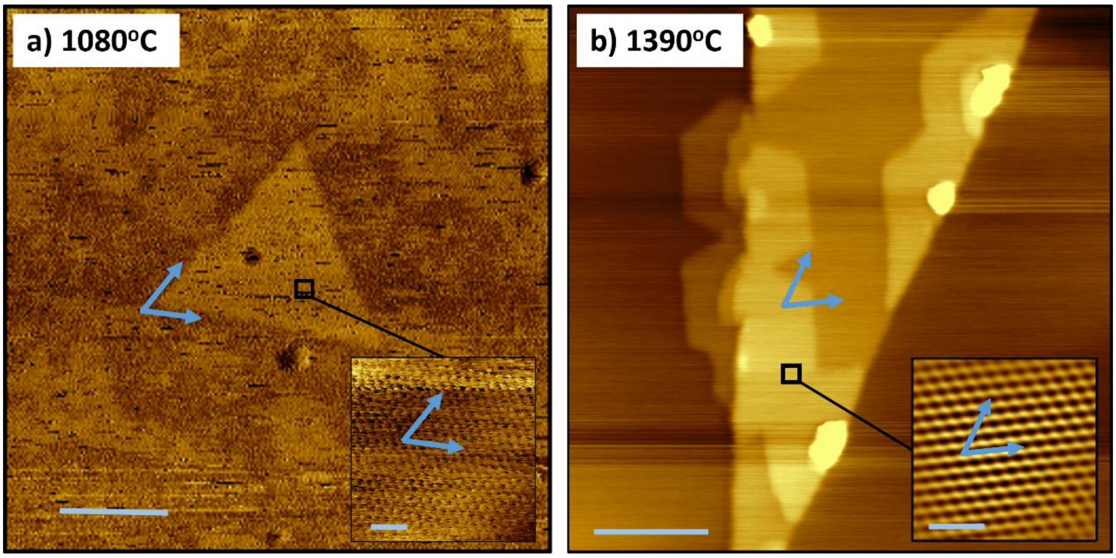

Figure 4.9 – Two contact mode images of the hBN/graphite surfaces with differing grain shapes taken from samples IV and V, respectively. Scale bars for the images are 200 nm, with scale bars of 1 nm for the two insets. The insets depict lattice images taken from identified points in the hBN domains. The directions of the lattice vectors have been identified and are shown on both the insets and the corresponding large-scale images. With the directions of the vectors being parallel (perpendicular) to the edges the same edges can be identified as zigzag (armchair).

of the resulting domains. The crystallographic orientation of the domains was identified and the predominance of different orientations was found to differ with substrate growth temperature.

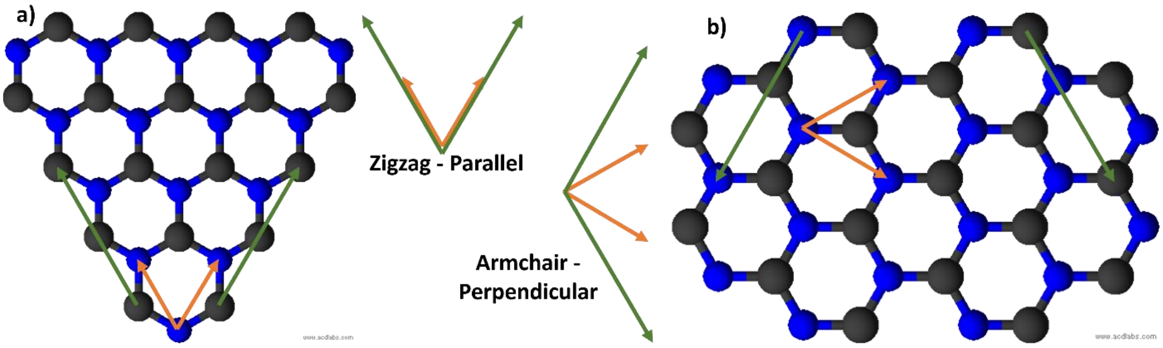

Figure 4.10 – Two lattices representing hBN are presented in a) and b). In each diagram the lattice vectors have been drawn in orange. Green arrows represent the direction of the edge of the lattices, which have also been drawn alongside the lattice vectors in the centre of the figure. Only orientation, not magnitude, matters for this diagram. Zigzag edges can be seen to lie parallel to the direction of the lattice vectors, while armchair edges lie perpendicular.

Contact topography images, such as those shown in the insets of Figure 4.9, were acquired with lattice resolution. The direction of the lattice vectors can then be compared with the direction of the domain edges. Island edges that run parallel (perpendicular) to the lattice vectors have formed following the zigzag (armchair) direction of the lattice. The orientations of the lattice vectors relative to the island shapes are shown in Figure 4.9 a) and b).

As was discussed in Chapter 2, the zigzag direction of the hBN lattice is not symmetric under elemental inversion. The zigzag edges may be terminated by B or N and the rate of growth of these two distinct edges may differ dependent on growth conditions. Figure 4.10 a) and b) exhibit small domains of hBN with zigzag and armchair dominant growth edges, respectively. The result is two islands with distinct geometries. A preference during growth for zigzag terminated edges of hBN results in triangular islands, such as in a). In the case where the growth rates of the two distinct zigzag edges are comparable hexagonal islands will theoretically form, but this was not observed on these samples.

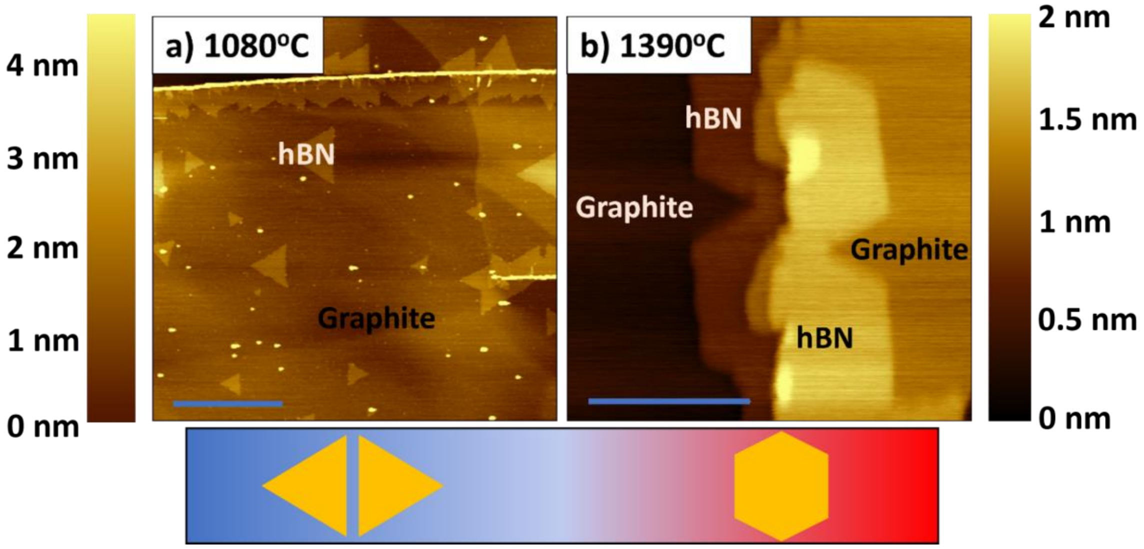

Figure 4.11 – AFM images a) and b) highlight the dominant shape of the hBN monolayers on these surfaces. Image a) was obtained in tapping mode and b) in contact mode. Scale bars are 500 nm and 100 nm respectively. Domains of hBN on sample IV, grown at 1080$^{o}$C, are triangular as seen in a). Samples grown at the higher substrate temperature used for V exhibited only hexagonal domains, with armchair edges, exhibited by the image in b).

Armchair terminated edges of hBN do not fundamentally change under inversion and the underlying hexagonal symmetry remains.

Comparison of the presence of islands of different shapes across samples of different growth temperatures revealed a transition between two morphologies. Figure 4.11 shows the observed transition of the hBN domain morphology from triangular to hexagonal shapes as the growth temperature was increased between samples. In Figure 4.11 a) each of the triangular islands is aligned with one of two directions as a result of the solely zigzag nature of the islands. Though the image in a) has been selected to exhibit the triangular hBN islands the reader may note an edge at the top of the image from which many of these domains have nucleated. In Figure 4.11 b) the higher growth temperature sample is shown to exhibit a hexagonal form. The temperature difference during growth resulted in changes to the preferred edge direction of the monolayer sheets during growth. In 2016 Zhang et al. described how the chemical potential of the constituent elements and the choice of substrate dictate the resulting island shape for epitaxially grown hBN [53]. Their work takes an atomistic approach to explaining the multiple stable structures for hBN islands on Ni(111) and Cu(111) substrates. On copper they found that varying the growth conditions between N-rich and B-rich changes the nucleation barriers of the different zigzag edges, resulting in a transition from N-terminated zigzag edges to B-terminated via other stable edges. This in turn changes the morphology of the islands from triangular to truncated triangles to hexagons as the growth conditions were varied sample to sample.

For the samples presented here the deposition rates of nitrogen and boron were not varied. Instead, the variation in temperature was the determining factor in the formation of the different edges and shapes. If the diffusion barriers of B and N on the graphite surface differ from each other, whilst being of the same order as ~$k_BT$ then a variation of the substrate temperature will impact the availability of B and N migrating across the surface. This in turn would influence the availability of the constituents at the growing edges of the monolayer sheet, providing a mechanism for varying the dominant selected edges.

DFT studies of the strength of interaction of nitrogen and boron atoms with an HOPG substrate provide adsorption energies of B and N atoms during the growth. The two studies referenced here for B and N adsorption energies make use of the optB86b-vdw density functional method, and the resulting adsorption energies are -1.29 eV and -1.1 eV respectively [141,142]. Differences in the adsorption energies show that increasing the growth temperature will reduce the relative prevalence of the N relative to the B species. A prior work using LDA derived functionals calculated migration energies for adsorbed B and N on a graphene surface. The migration energies referred to in the work are defined by the system energy difference between an adatom being present at adjacent sites on the graphene surface. These values provide a minimum of the height of the diffusion bar, but cannot inform on the total height of the barrier. The migration energies of B and N were calculated at 0.12 eV and 1 eV respectively, though the values calculated are very likely to be overestimates due to the choice of functional [143]. Thus, as growth temperatures are increased the diffusion rate of the B will increase relative to that of the N species. At the lowest growth temperature considered the N to B ratio will be greatest, and N-termination may be supposed.

It should be noted that the large spot size of the Raman system and the identical crystalline appearance of the different zigzag edges in AFM prevent identification of the zigzag termination here.

### 4.6 Role of Graphite Steps in Nucleation

A notable difference between the hBN nucleated from monolayer steps on the graphite surface and that growing from multilayer steps has been identified. As can be seen in Figure 4.12 sheet and aggregate material has grown primarily from steps on the graphite substrate at all temperatures. As

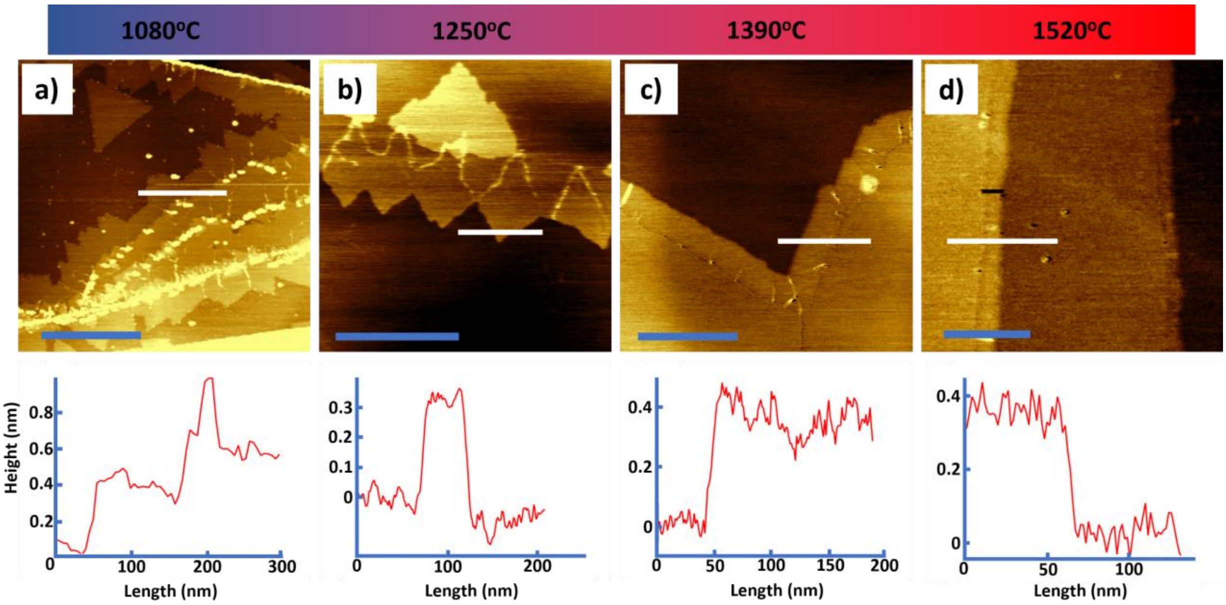

Figure 4.12 – Growth from monolayer steps on samples grown at different substrate temperatures are presented to summarise the differences observed in the growth. Scale bars differ between images and are 400 nm, 250 nm, 300 nm, and 100 nm for a-d) respectively. Profiles are depicted taken from the white lines on each image to establish the presence of the monolayer. As the temperature is increased between the samples in images a-d) the quantity of material seen after growth is reduced. For samples grown at temperatures at 1390°C and above no aggregate material has accumulated at monolayer steps. Above 1080°C the steps are necessary for the formation of hBN sheets as islands of material are rare or not observed.

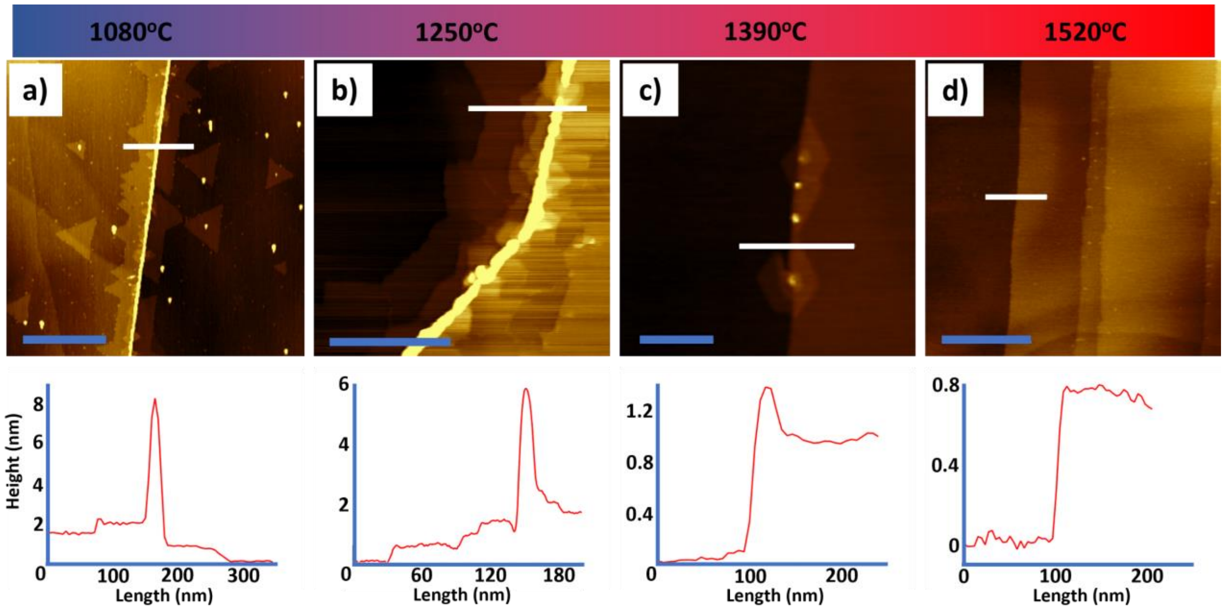

Figure 4.13 – Images taken from samples grown at the four different growth temperatures are presented to show temperature-dependence of material present at multilayer steps. Scale bars differ between images at 400 nm, 200 nm, 150 nm, and 300 nm for a-d) respectively. Profiles taken along the white line are presented beneath each image to identify the height and presence of the multilayer step. As the growth temperature was increased between samples reduced aggregate formation is observed. For the temperatures represented in a) and b) the presence of the multilayer step or the aggregate formed from it has provided nucleation sites for the formation of material along the top edge of the step, which is considerably less common for the monolayer steps. In the higher temperature samples all sheet and aggregate formation is observed to have been reduced, with no aggregate or sheet formation at all from the multilayer steps for the 1520°C sample.

the growth temperature increases between the samples depicted in Figure 4.12 a-d) monolayer height steps provide sites for nucleation of sheet material while a reduction of aggregate material is obtained. By comparison the images in Figure 4.13 showing multilayer steps on the surface continue to exhibit aggregates up to and including the highest growth temperature. Growth from multilayer and monolayer steps additionally differs by the increased nucleation of sheet material above the multilayer steps at the lower growth temperatures and a comparative loss of nucleated sheet material at the higher growth temperatures. The height of the steps has influenced both aggregate formation and monolayer sheet formation from the upper and lower sides of the steps with variation over the considered temperature range.

### 4.6.1 Nucleation from Monolayer Steps

As can be seen in Figure 4.12 a) and b) the majority of sheet material has grown out from the lower side of the graphite step. The edges provide sites for nucleation of hBN sheets during growth via the attachment of boron and nitrogen atoms. The 2D nature of the graphite surface additionally provides templating for the assembly of 2D hBN material, a necessary condition for the formation of planar growth [43]. Figure 4.14 displays atomic models exhibiting three of the lateral interfaces that can be expected from merged planes of hexagonal boron nitride and graphene.

The models provide the building blocks for lateral interfaces of arbitrary scale and direction on the surface. For any of these interfaces reversal of the B and N occupation of A and B sites of the sublattice results in a new lattice asymmetric with the original. As a result two adjacent hBN domains with different A and B site occupation cannot merge without defect formation and grain boundaries will form between them. The grain boundaries formed from this inversion could be expected to align perpendicular to the graphite step due to the similar growth rates of the neighbouring domains. On the samples investigated grain boundaries with a variety of orientations have grown, including some boundaries running perpendicular to the graphite step. By identifying the direction of the graphite step the lattice direction of the grain boundary can be assigned and the composition of the grain boundary may be considered.

The stability of the interfaces depends upon the registry of the lattice with the underlying graphite lattice. Zhong et al. predicted that a bilayer of hBN and graphene will exhibit a preferred stacking of AB in which only half of the atoms in one layer lie directly under atoms in the adjacent layer [144]. The diatomic nature of hBN requires establishing where B or N atoms will lie directly under C atoms in this stacking mode. Zhong et al. estimated that AB stacking with B atoms directly beneath C will lead to the most stable structure, though the energy difference between this stacking and the other two were relatively small [144]. In the interfaces presented in Figure 4.14 if the edge carbon atom lies atop the centre of a hexagon in the layer beneath then the depicted ZZ edges will exhibit AB (nitrogen) and AB (boron) stacking respectively, and the armchair edges could exhibit either. If the edge carbon atom

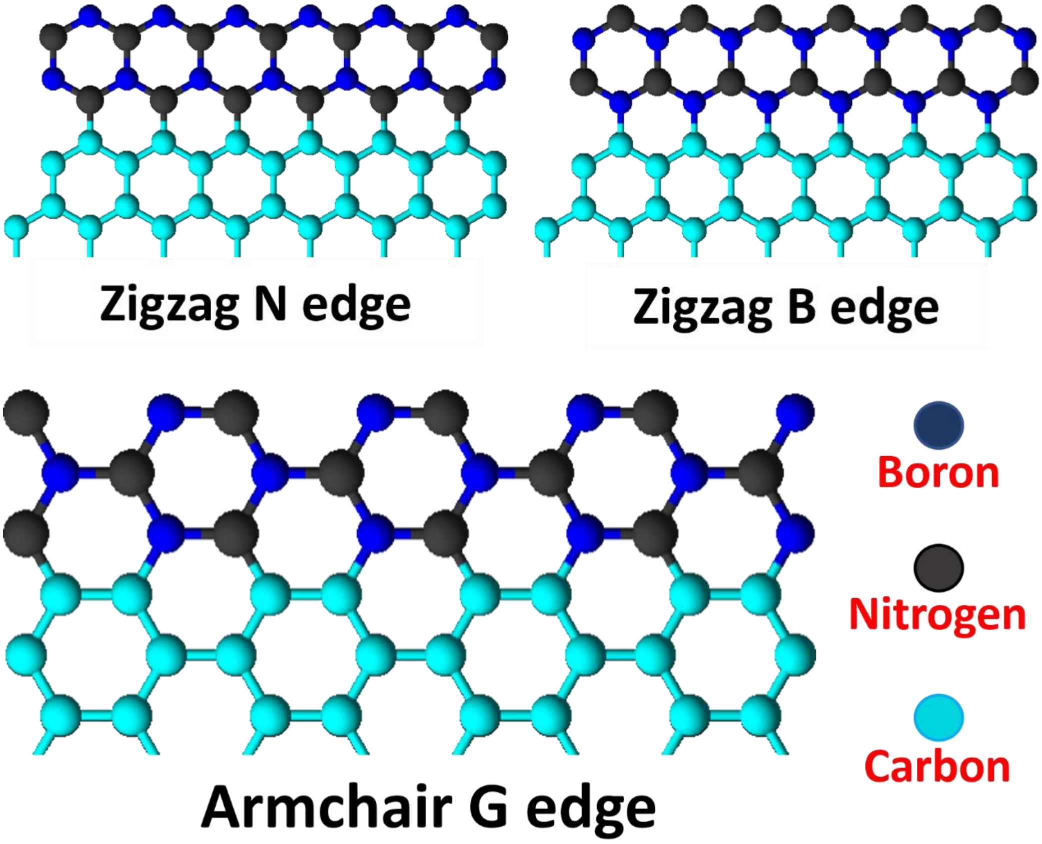

Figure 4.14 – Models of graphite monolayer steps merged with hBN layers. Geometrical considerations of the hexagonal structure results in three distinct interfaces between the graphene and hBN without the formation of defects. a) and b) represent an interface of the two materials along the zigzag direction. Where the two materials have merged exclusively C-B or C-N bonds are formed. Transitioning between a) and b) on the same step could occur by the formation of a line defect on the surface where the two phases meet. In c) the interface follows the armchair direction. Both B and N atoms bond directly to the carbon edge in this instance. Boundaries between neighbouring domains may still arise from inversion of the occupancy of the A and B sites. The lines of defects that would arise from the armchair or zigzag interfaces differ substantially.

resides in the other sublattice site then the edges will exhibit AB (boron) and AB (nitrogen) stacking, respectively. Due to the similar stability of AB (boron) and AB (nitrogen) it is uncertain whether the graphite sublayer will have an impact on the growth of hBN interfaces. The images available cannot distinguish between the two AB stacking modes, though it should be supposed that AB (boron) will be more prevalent where the N to B ratio is low during growth.

Due to the diatomic nature of the boron nitride lattice the composition of the grain boundaries are determined by the interplay of strain at the boundary and the energy cost of forming homo-elemental bonds [145]. The conflict between these two parameters drives the selection of defects along the grain boundaries, as described by Liu et al. (2012)[145]. In their work they identify two defect pairings that can arise at these boundaries, labelled 4|8s and 5|7s, which refer to the number of atoms in the defect

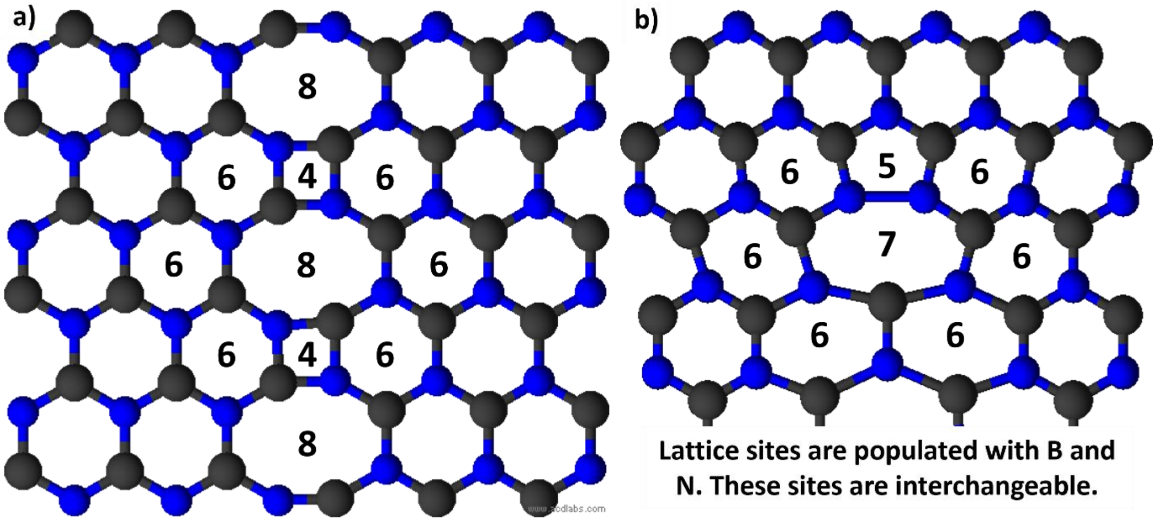

Lattice sites are populated with B and N. These sites are interchangeable.

Figure 4.15 - Diagrams are shown containing a) 4|8 defect pairs and b) 5|7 defect pairs, respectively. In a) a line of 4|8s follow the armchair direction of the hBN lattice, with minimal impact on neighbouring atoms. This defect chain is expected to be energetically favourable when the two domains on either side are misaligned by 180° as shown. Though the 4|8 defects in 4.13 a) follow the armchair direction, lines of 4|8s can arise along zigzag directions of the lattice too. b) shows a single 5|7 defect pair, differing from the 4|8 defect by the need for a homo-elemental bond between the 5- and 7-member rings. The contest between accumulated strain, energy cost of the homo-elemental bond, and the relative misorientation of the domains determines which defect pair is preferred during growth [145].

rings. The appearance of these defects is shown in Figure 4.15, with a) and b) depicting 4|8 and 5|7 instances, respectively. These defects always arise in pairs, such that a 4-member ring may not exist without the formation of an adjacent 8-member ring. 4|8s require no homo-elemental bonds, but introduce significant lateral strain compared to the 5|7s. A single homo-elemental bond exists between the 5- and 7-member rings of the 5|7 pairing and there is less deformation of the lattice, resulting in a lower cost in strain. The most stable defect of the two pairs is dependent on the relative orientations of the hBN domains, as this impacts the strain accumulated by the formation of the defects [145]. For domains of 180° relative rotations, equivalent to the inversions described earlier, 4|8s are expected. 4|8s buckle out of plane to reduce the strain accumulated in formation. This buckling may explain the observed height of the grain boundaries in tapping mode AFM.

The straight graphite steps observed by contact mode AFM to follow zigzag and armchair lattice directions lead to adjacent hBN domains with little or no misalignment. In these instances, the boundaries are expected to consist of 4|8 defect pairs.

During the MBE growth of hBN on graphite two distinct structures are observed to nucleate above monolayer steps, amorphous aggregates, and monolayer sheets of hBN. Defects arise at the lateral hBN-graphite interface of monolayer graphite steps due to the lattice mismatch between the two materials. The lattice mismatch leads to the accumulation of strain along the interface until point or line defects form. These defects and any others that may arise along the edge provide potential nucleation sites for material on top of the graphite steps.

### 4.6.2 Impact of Multilayer Steps on Aggregate and Monolayer hBN Formation

In Figure 4.16 a) the multilayer steps are seen to provide nucleation sites for the formation of monolayer hBN above and below the steps. The lower half of the image shows a monolayer step in which coverage of the region above the step is greatly reduced in comparison that above the multistep. The hBN growth on different graphite steps additionally differs by the growth beneath the steps. Multilayer steps have been observed to exhibit reduced nucleation of the monolayer hBN sheets below the step, as shown in b). This is only observed for the higher temperature samples, which also exhibit a comparative reduction in the presence of aggregates at these multilayer steps.

Multilayer unreconstructed steps of graphite consist of hybrid $sp^2$ orbitals. Unlike in the case of the monolayer a single monolayer of hBN grown from this step does not provide stability or bond at every available site. The remaining carbon atoms provide sites for the nucleation of additional boron nitride sheets or introduce non-planar material at the step. At the step, attraction between the graphitic layers can induce a slight $sp^3$ character to the outermost bonding orbitals, which introduces a 3D nature to the bonding system [146]. It is the potential for bonding between layers and the greater potential for the formation of defects which could result in the aggregate structures observed.

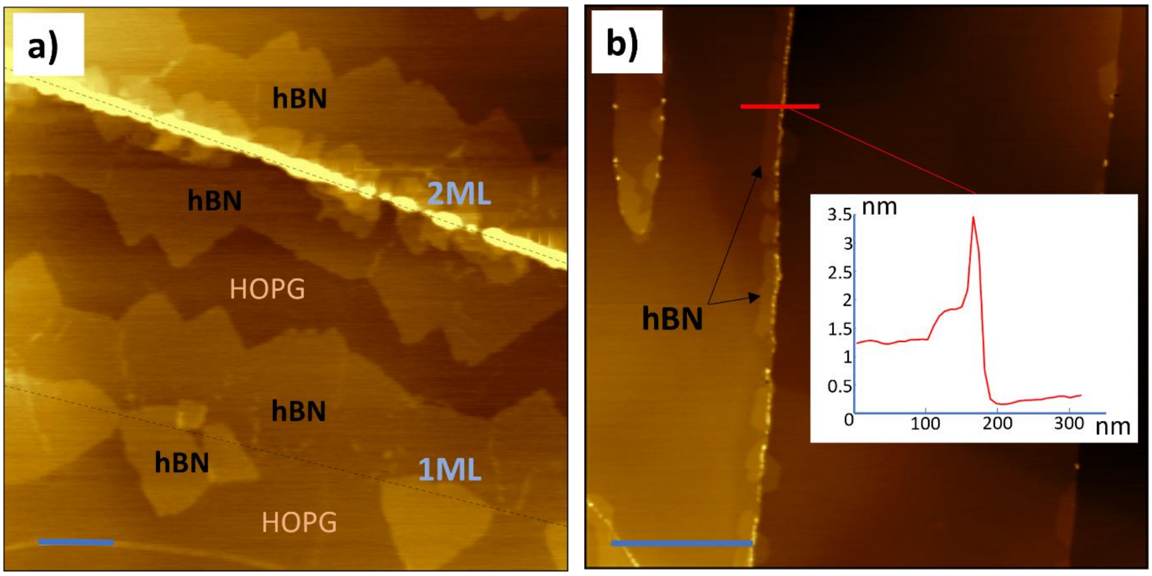

Figure 4.16 – Topography Images a) and b) were obtained by tapping mode AFM and have been selected to highlight differences between monolayer and multilayer differences in growth. With a scale bar of 100 nm a) depicts a 2ML step in the upper half of the image, from which can be seen high monolayer sheet presence above and below the step, and high aggregate presence along the step. Fragments of multilayer hBN nucleation are also observed with minimal lateral growth. Image b) shows a multilayer step upon which hBN is only observed on the upper half, identified using the profile in red. The lack of monolayer sheet nucleation at the lower edge of multisteps is exclusive to the higher temperature samples, V and VI.

In the formation of a hBN sheet on a graphite monoatomic step many of the potential pathways for the nucleation of the aggregates are missing compared to multilayer steps. Only point defects at the graphite edge or those introduced by the mismatch strain between hBN and graphite allow for the continued formation of the amorphous 3D structures. As was represented in Figure 4.8 c), the monolayer step at the bottom of the image exhibits a greatly reduced aggregate presence, in agreement with the suppositions on the nucleation possibilities.

## 4.7 Summary

Various properties of the produced hBN/graphite structures have been analysed with combinations of tapping mode and contact mode AFM. Variation in the growth parameters, namely substrate temperature and growth time, strongly influence the morphology of the surface. Control of these parameters provides a means to optimise growth for the production of lateral and vertical heterostructures by minimising amorphous aggregates. Higher temperatures are observed to reduce the formation of aggregates and the growth of the hBN sheets, though minimal aggregation is observed at growth temperatures of 1390°C with non-trivial hBN sheet presence.

Another observed impact of increased substrate temperatures is the changing morphology of hBN islands and step growths. A transition is observed from triangular shapes to hexagonal across samples grown with substrate temperatures from 1080°C to 1390°C. Prior works on Ni suggest changes in the chemical potentials of the B and N constituents may cause the transition, which in turn are influenced by changes in the relative prevalence of the constituent materials as the temperature varies.

Different graphite steps, distinguished by height in layers, exhibit markedly different aggregate and hBN sheet presence. Aggregate density is substantially increased at multilayer steps when compared to the monolayers which, at higher temperatures, exhibit little to no aggregate presence at all.

Additionally, hBN sheets nucleate preferentially on the lower terrace of a monolayer step, but are comparatively rarer below the multilayer steps at higher growth temperatures.

# Chapter 5: MBE Production of Graphene with an e-beam Sublimation Source

## 5. Introduction

Prior studies on the high-temperature molecular beam epitaxy (HT-MBE) of graphene made use of two distinct carbon sources. These sources generated the required carbon flux by the Joule-heating of either a high-purity graphite filament, or a sealed Ta tube containing finely powdered carbon. MBE with both sources can produce graphene monolayers on a hBN substrate. As described in Chapter 2, these sources exhibit limitations that should be overcome to scale the production of graphene as necessary for industrial applications. The graphite sublimation source results in a relatively high density of carbon deposits, from which monolayer graphene appears to nucleate. The Ta filament source on the other hand exhibits a high turnaround of filaments, with filaments breaking after every few depositions as a result of the necessarily high operating temperatures. In this Chapter the results of a source designed to produce the carbon beam with sublimation resulting from heating induced by an electron beam are investigated.

Graphene has been grown on hexagonal boron nitride using molecular beam epitaxy of carbon onto hBN flakes. The produced G/hBN flakes exhibit complete monolayer coverage of the graphene, with occurrences of bilayer and multilayer material, and amorphous carbon aggregation. Moiré patterns with periods above the incommensurate maximum of 13.6 nm are observed. Other features of the graphene layers include defects in the moiré patterns, strain-induced distortion of the moiré pattern, and cracks in the graphene layer. These properties and other surface features were observed and measured with atomic force microscopy. In this Chapter these features are described and explanations for the retention and impact of strain accumulated during growth are presented.

The process for the production of the G/hBN samples on sapphire is presented in 5.1, and the analysis methods for the subsequent samples are discussed in 5.2. Following these Sections the surface features are described and, where possible, explained, in Sections 5.3 through to 5.4. Finally, the Raman maps taken across the surface of flakes on the samples is presented, and a comparison between the Raman spectra of graphene on terraces against that of the aggregates is provided.

### 5.1 Production of the graphene

Before introduction to the vacuum system the sapphire substrates must be cleaned and loaded with hBN. Sapphire was selected as the substrate due to its high chemical stability and melting temperature, remaining stable at temperatures above 2000°C. The 1 cm x 1 cm x 1 mm c-plane sapphire substrates were cleaned with a toluene immersion, followed by $N_2$ stream drying, immediately prior to the hBN exfoliation. hBN flakes prepared via exfoliation were then deposited by pressing the loaded tape onto the sapphire surface before peeling away to leave flakes on the surface. The exfoliation deposition of hBN flakes onto the sapphire substrates results in tape residue on the sapphire. This material was removed prior to introduction of these substrates into the vacuum system with a two-step process. Firstly, the hBN/sapphire samples were soaked in toluene overnight before removal and drying with a $N_2$ stream. Secondly, the samples were introduced to a tube furnace and heated to 400°C for 8 hours under a $H_2$:Ar (5% $H_2$ and 95% Ar) atmosphere with a flow rate of 0.15 slpm.

After this cleaning process the samples were placed onto a Ta holder and introduced to the MBE chamber described in Chapter 3. The system is pre-annealed at 400°C for 0.5 hours in the vacuum chamber. The sample holder is then heated to 1390°C, measured by a thermocouple behind the substrate holder. Carbon is deposited for 2 hours from the e-beam evaporator EBVV 63-T4 source. To achieve a consistent deposition rate between samples the current applied to the tungsten filament after a fresh fill of the carbon source material was 200 mA, which was increased by 50 mA for every subsequent deposition. The deposition rate is estimated ex-situ by AFM of the sapphire substrate, comparing a gap scratched into the carbon layer with tweezers to the height of the carbon layer. The growth rate of the carbon layer on the sapphire is found to average 38 ± 1 nm/hour, while only a small fraction of carbon material is retained on the hBN flakes.

### 5.2 Methodology of AFM and Raman

After cooling in the vacuum system, the samples can be removed and imaged with tapping- and contact-mode AFM. AFM images of the surface were otherwise acquired in the same manner as discussed in Section 4.2. The phase images provided by tapping-mode AFM provide the means to identify the material composition of the surface, and topography can be used to find the thickness of features at a location.

Raman spectra obtained from several flakes have been used to identify the material composition with lateral precision down to the spot size of ~ 2 microns. Spectra were acquired with a Horiba LabRam HR, using the 532 nm laser calibrated prior to measurement with a Si sample. A grating with 300 lines/mm was used alongside a laser power of ~ 30 mW and acquisition time of 45 s to acquire the spectra presented. Peaks present within a Raman shift range of 1200 $cm^{-1}$ to 3000 $cm^{-1}$ were identified and fitted with pseudo-Voigt peak profiles in OriginPro 8.5. As will be discussed in Section 5.5 the intensity, FWHM, and positions of these fitted peaks can provide information on strain, defect density, and the number of layers of the graphene, along with other properties.

## 5.3 Introduction to the Surface Morphology

Many features of the G/hBN surfaces are common to samples from all considered sources. Graphene monolayers are consistently observed on the hBN substrate including islands of relatively small lateral scales up to complete surface coverage. Moiré patterns have been observed across the deposited graphene surfaces, which shows that the graphene monolayers are in alignment with the hBN substrate. In addition to the graphene sheets carbon aggregates are observed as a result of growth from any of the sources [14–16]. As will be discussed in a later Section the composition of these aggregates appears to differ between sources, with a likely dependence on the size of the carbon clusters arriving on the surface during growth.

Figure 5.1 shows topography images exhibiting several features observed from the e-beam samples. In 5.1 a) a large (several microns) region of monolayer graphene has been punctuated with amorphous aggregate clusters, from which bilayer and multilayers have nucleated. The hexagonal moiré patterns

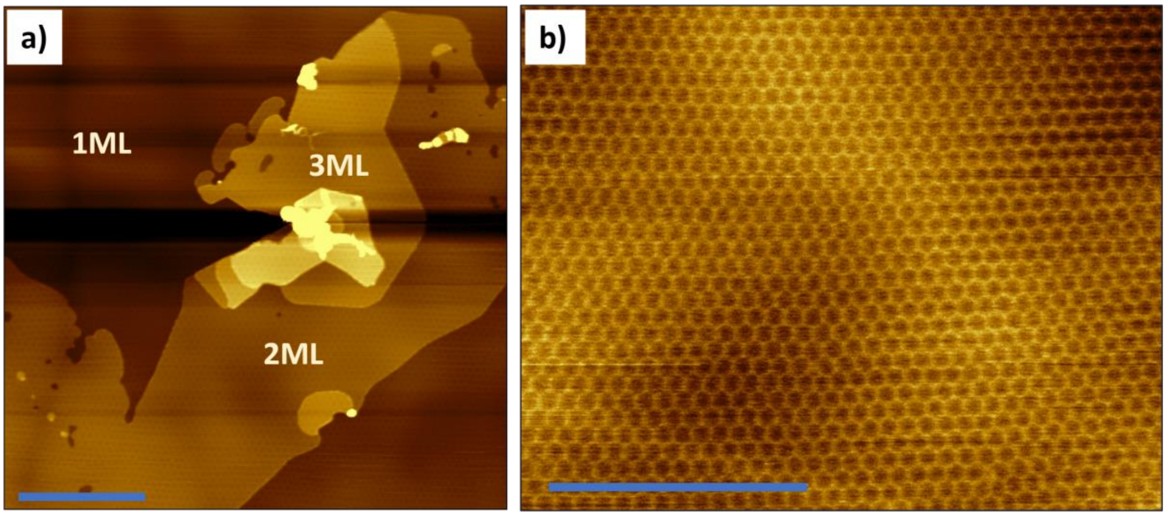

Figure 5.1 – a) to b) are tapping mode AFM images of the graphene surface grown on hBN flakes with scale bars of 250 nm and 200 nm, respectively. a) depicts graphene grown with a complete monolayer and sizeable bilayer presence. Unstrained and uniform moiré patterns can be seen to extend across all layers. An aggregate acts as a nucleation point for the formation of the multilayers. Image b) depicts a highly uniform unstrained moiré pattern over a large area. The moiré period is 14.0 ± 0.2 nm, implying a non-zero but small strain, common to many of the graphene sheets observed in this thesis.

on the graphene in 5.1 a) have periods of ~ 13.6 nm. This corresponds to aligned graphene on hBN where there is no angular misorientation between the lattices. This highly uniform moiré pattern is also identified in 5.1 b), a 500 nm square topography image from a different sample. In b) the period of the pattern is 14.0 nm, consistent with the presence of minimal, but non-zero, strain in the graphene lattice. Strain accumulated in the graphene lattice can be identified by comparing the observed moiré pattern, $\lambda_s$, to the expected maximum period of $\lambda_0$ = 13.6 nm, with the following equation,

$$\frac{\Delta a}{a} = \frac{\delta a}{a}\frac{\Delta\lambda}{\lambda_s} \tag{5.1}$$

Where $a$ is the graphene lattice constant, $\Delta a/a$ is the fractional strain accumulated in the lattice, and $\Delta\lambda$ is defined as $\lambda_s - \lambda_0$. The $\delta a/a$ term encompasses the relative difference in the lattice constants of graphene and HBN prior to strain, or 1.8%.

Figure 5.2 presents tapping-mode AFM images of graphene surfaces showing features likely arising from the presence of high strain in the grown surfaces. Figures 5.2 a) and b) depict the topography and phase images, respectively, of a region of the G/hBN surface in which two graphene sheets are separated by the formation of a crack in the graphene. Moiré periods on either side of the crack, more easily identified in the phase image in b), exhibit distinct periods and orientations. A changing strain distribution likely contributes to the changing directions of the moiré lattice on the left of the crack, though on a smaller scale the strain appears isotropic. Image c) provides an example of a highly strained moiré pattern. The period of the observed moiré pattern is around 40 nm, corresponding to significant strain in the graphene lattice. The distribution of strain through the lattice in this region is non-uniform, with the period of the pattern varying with orientation and position in the region. Moiré patterns with periods greater than 13.6 nm are observed on all graphene sheets present on these samples. The previously described MBE carbon sources also produced graphene sheets with moiré periods greater than 13.6 nm.

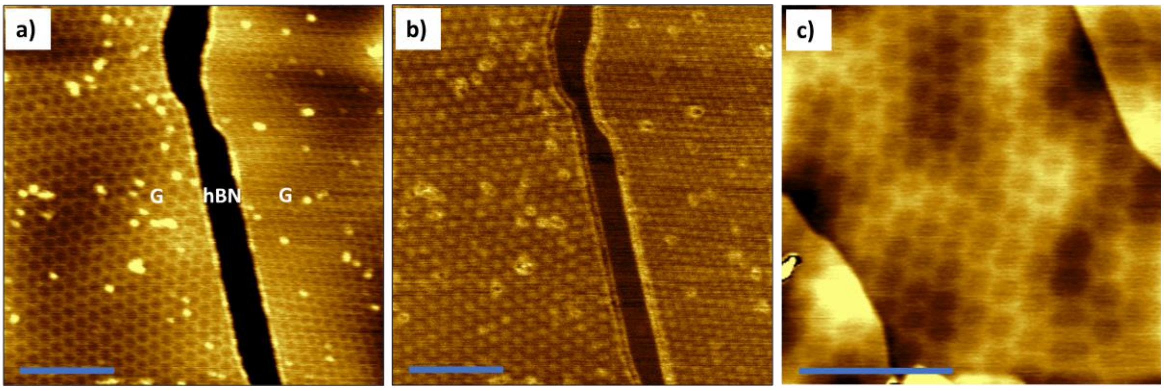

Figure 5.2 – Three tapping-mode AFM images depicting regions of the G/hBN surface exhibiting high or anisotropic strain. Images a) and b) are topography and phase images with scale bars of 100 nm of the same region in which a crack in the graphene monolayer has formed. On either side of the crack, which exposes the hBN substrate, the strains of the graphene monolayer differ and therefore so do the moiré periods. In the topographic image c), with a scale bar of 200 nm, a highly strained moiré pattern is shown. The period of the moiré pattern is ~40 nm. The strain is non-uniform with the orientation and period of the pattern changing across the image. The period varies between 36.8 nm and 49.1 nm.

Wrinkles on the hBN flakes are observed, at scales on the order of 100 nm. On $SiO_2$ substrates temperature regimes in which strain is transferred or otherwise between the substrate and the hBN flakes has been shown to lead to accumulated compressive strain in hBN flakes during a thermal cycle, leading to wrinkle formation [71]. The formation of these wrinkles in the hBN flakes is commonly observed on sapphire substrates, such as the those used here [15]. In addition to the wrinkles, extensive chains of carbon aggregates are identified, extending vertically to over 100 nm from the terraces.

Despite the similarities of the graphene and boron nitride lattices many of the interesting properties of the vertical heterostructures of the two materials arise as a result of their differences. Different lattice parameters lead to moiré patterns as already described, and the introduction of point defects. Differences in thermal expansion coefficients have been proposed to introduce strain in the surface, leading to wrinkles, cracks, and extended moiré patterns [15].

### 5.4 AFM Observations of the Graphene Sheets

Sheets of graphene grown on hBN commonly exhibit a moiré period of ~13.6 nm originating from the lattice mismatch between the two lattices, oriented with zero twist angle. As described by Woods et al. a highly oriented heterostructure of graphene and hBN may occupy one of two distinct phases, the incommensurate and commensurate states [57]. The states impact the stacking modes of the lattices locally. For samples in the incommensurate state the stacking of the two lattices varies across the surface. Bulk boron nitride favours the AA' stacking mode, as described in Chapter 2, in which any two layers are positioned with each atom in a layer lying directly below and above atoms in the adjacent layers and elemental site occupancy alternated between the two layers. Thus, adjacent hBN layers differ by alternating between the two constituent atomic species present at the A or B lattice sites. The alternation of site occupancy minimises the distance between B and N atoms. This stacking mode differs from AB, in which adjacent layers differ by an offset of one bond length, which acts to increase the distances between atoms in adjacent layers.

The differences in lattice constants between graphene and hBN prevent the perfect alignment of a specific stacking order over long distances. Instead, the surface undergoes a transition between an AA-like and AB-like stacking mode over the period of the moiré superlattice. This does not apply for the commensurate surface, which can be expected in the case of zero twist angle and pinning of the lattices. In commensurate regions the strained graphene lattice matches lattice constants with the hBN substrate lattice over a small scale. This lattice matching leads to stacking in either the AA or AB mode. The strain generated by the changes in the graphene lattice is accumulated into small regions of highly compressed graphene. The result appears similar to the moiré pattern. The differences in strain of the lattice-matched and strain-accumulated regions will lead to broadening of the Raman 2D peak over the commensurate regions, when compared to incommensurate samples.

Pinning of adjacent layers of 2D materials is very common, preventing the layers from moving relative to each other to release strain or conform on larger scales. As a result of pinning to the hBN substrate

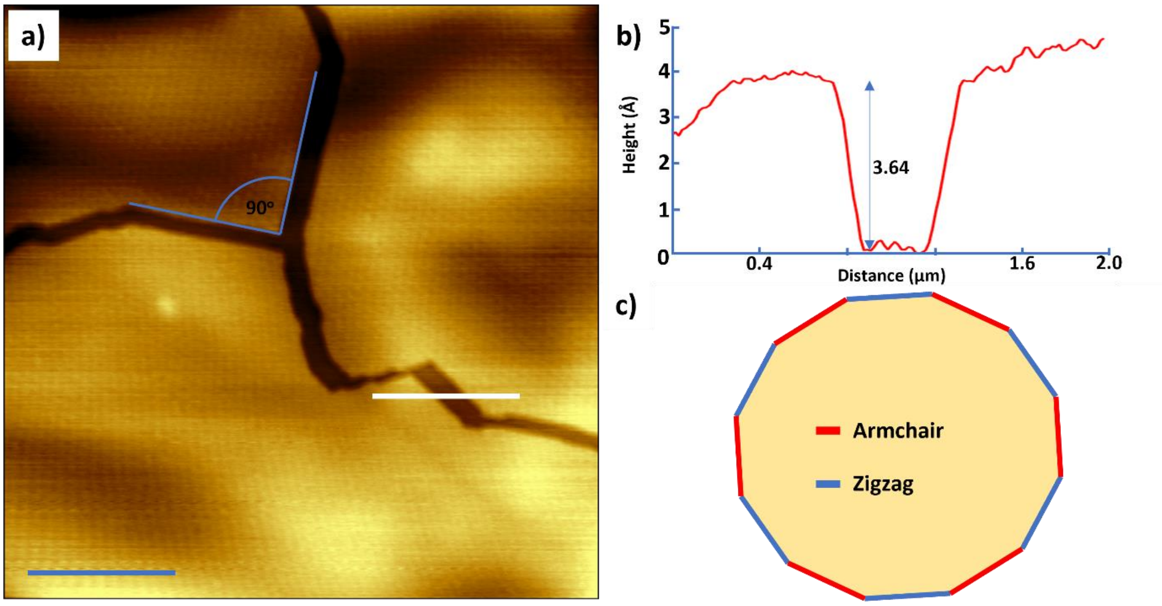

Figure 5.3 – a) shows a topographic AFM image of three graphene domains that have separated by the formation of a crack in the graphene layer. These cracks are believed to form to release strain accumulated by the cooling of the surface post-growth. The scale bar represents 200 nm, and a profile taken across the exposed hBN is shown in b). The edges of the graphene domains tend to follow crystallographic directions, identified in c) as armchair and zigzag which can be transitioned between by a rotation of the edge direction relative to the lattice of 30°.

and the differences in thermal expansion during cooling post-growth, the graphene surface may accumulate significant strain. On samples produced from the three sources the presence of aggregates is consistently a feature, and it has been proposed that these aggregates, or the defects on which they may form, may provide the pinning sites. This strain results in an increase in the average graphene lattice constant, leading to moiré periods greater than 13.6 nm. Cracks observed in the graphene layer may arise as a result of strain release as the material cools post-growth. An example of one of these cracks is shown in Figure 5.3 a), where the break in the graphene has revealed the underlying hBN substrate. Cracks such as these were observed on samples with large moiré periods and extend several microns across the terraces of monolayer graphene sheets. As shown in Figure 5.3 a) these cracks follow crystallographically significant directions of the relaxed graphene lattices, that is the armchair or zigzag directions, with directional changes of the crack following multiples of 30°.

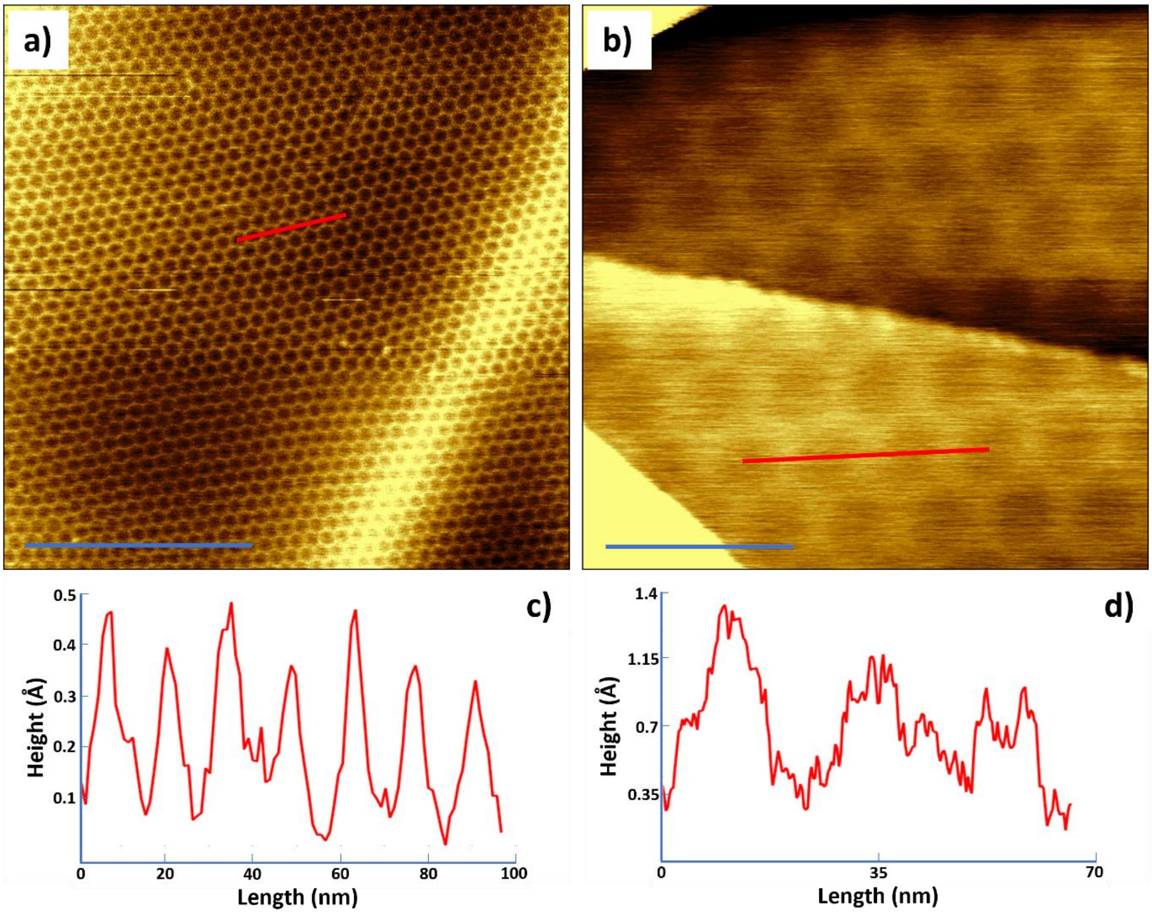

Figure 5.4 – a) and b) show topographic images of unstrained and strained moiré patterns found on the G/hBN samples. Scale bars on the images are 200 nm and 50 nm, respectively. The periods of the moiré patterns are exhibited in the profiles shown in c) and d). In a) the moiré pattern varies over 14 ± 1 nm on average, with a slight anisotropy in direction between a minimum of 13.8 nm and a maximum of 14.5 nm, with an observed wrinkle in the right of the image not appearing to impact the observed pattern. Similarly in b) the moiré period varies from 20.8 nm to 22.5 nm over the three distinct directions. Notably the pattern here is consistent across the bilayer monolayer and bilayer graphene, which is expected for zero twisting angle between the graphene layers.

Where cracks do not form the highly strained surface can be identified by the moiré periods, with periods above 13.6 nm, and sometimes exhibiting aperiodicity consistent with anisotropic strain. Figures 5.4 a) and b) depict an unstrained and strained surface, respectively. The periods of the two moiré periods being 14 and 22 nm are consistent with strains of 0.0 % and 1.1 % in the graphene lattice. The moiré pattern is unaffected as it transitions between the monolayer and the bilayer

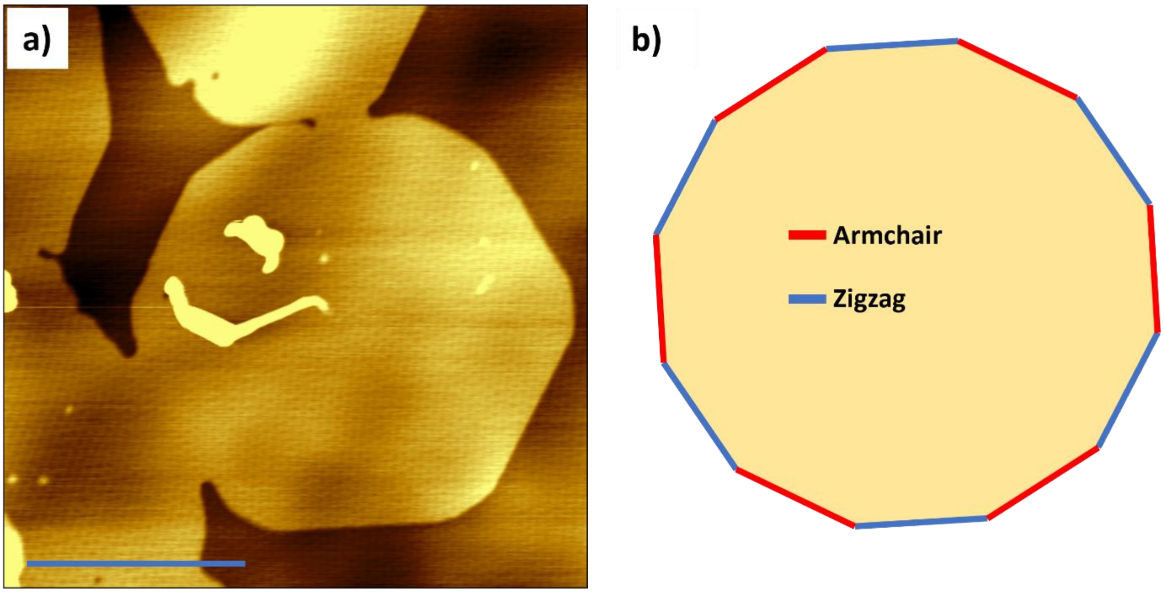

Figure 5.5 – Incomplete bilayers of graphene grown upon complete monolayers of graphene were observed on some samples. Image a) is an AFM topography image with a scale bar of 300 nm, which depicts a bilayer domain that has merged with other bilayer domains at some edges during growth. The edges of this central domain conform to the dodecagonal shape expected from a graphene domain with edges following the armchair and zigzag directions of the lattice.

regions of the image in b). A non-zero twisting angle between the graphene layers leads to the introduction of a second moiré with a much smaller period, which has, in previous works, been seen to reduce the visibility of the hBN/G pattern. Instead, here we observe that the moiré patterns are generally unaffected by the presence of the bilayer or trilayer, such as in Figure 5.5 a). As a result, we can conclude that all multilayers are aligned to a very high degree with the underlying graphene monolayer. For unstrained aligned moiré patterns exhibiting 13.6 nm periods the Z edge of the moiré pattern is aligned with the Z edge of the underlying lattice.

As described by Cosma et al. defects observed in the moiré pattern translate to defects in the underlying lattices [147]. This is because, assuming that both lattices producing the moiré pattern are mostly defect-free, any defect in either lattice is magnified because of the in-plane dislocation of all nearby sites relative to their position without the defect. Defects can be expected to have formed in the surfaces analysed here for several reasons. Growth of material from hBN steps will inherently result in defect formation due to the lattice mismatch between the two materials. Defects should also

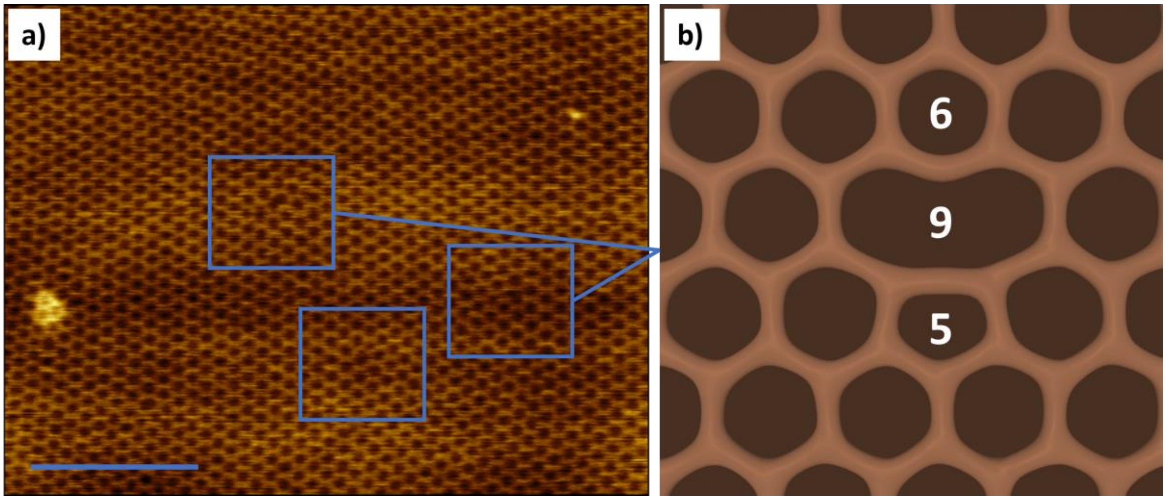

Figure 5.6 – In a) a large continuous graphene monolayer is depicted exhibiting multiple instances of single vacancy defects in the moiré pattern over a 1 $\mu m^2$ area. Several of these defects are identified within the blue squares and associated with the lattice model presented in b). These defects are characterised by a missing carbon atom and a reconstruction around the defect site. These defects may act to reduce some of the strain present in the lattice, such as that arising from the templating of grown graphene material over the slightly larger hBN lattice. The printed numbers represent the sum of carbon atoms contributing to the ring.

be expected to arise from the interaction between neighbouring domains of the epitaxial material during growth, arising from imperfect merging where rotational misalignment is present. In Figure 5.6 a) a large continuous monolayer of graphene, on the order of 1 µm, is depicted on which several defects are observed. Those highlighted are instances of single vacancy defects, in which a single unoccupied site in the honeycomb lattice results in a 9-membered ring, and a neighbouring 5-membered ring. In a surface exhibiting distortion the presence of vacancy defects is expected. These defects are known to impact the strength and thermal conductivity of the graphene, in part due to the introduction of dangling bonds to the sheet [148].

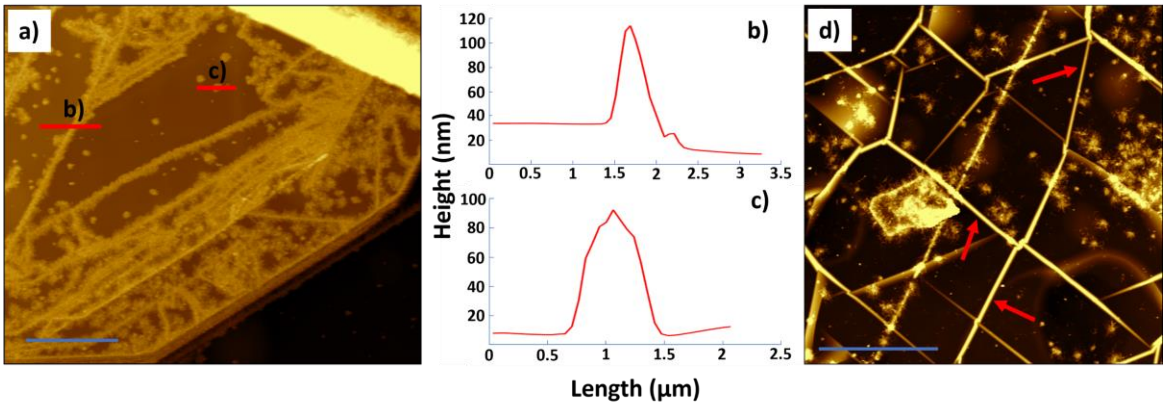

Figure 5.7 – Two distinct structures with heights on the order of tens of nanometres are observed on all samples presented here. Aggregate structures are shown in a) with the scales of chains of these aggregates and aggregate structures positioned on graphene terraces presented in b) and c) taken from the red profiles in a). The aggregate structures in image a) are ~ 85 ± 5 nm in scale and consist of most of the carbon accumulated on the hBN flakes during growth by volume. In d) the other distinct structure is exhibited. Red arrows highlight some of the many instances of wrinkles in the hBN flake, that criss-cross the surface. These wrinkles vary in vertical height significantly and are believed to arise from the heating of the hBN flakes.

### 5.5 Observations of the Grown Aggregate Structures on hBN Flakes

Two different large-scale structures, those taller than a few nanometres, are observed on the samples. Carbon aggregates with an unknown structural composition are observed to have formed over a significant fraction of the hBN surface. Secondly, wrinkles in the hBN susbtrate are observed to have formed, which is expected to be a result of the thermal cycling of the hBN flakes. The specifics of the aggregate composition are unknown, though they are formed during the carbon deposition. Aggregates exhibit height scales on the order of ~100 nm, as seen in the profiles of Figure 5.7. Single points of aggregate accumulation are observed on otherwise clear terraces and strings of aggregates are observed too, used here to define the edges of the terraces. Wrinkles in the hBN are also observed, separated by microns, with vertical scales on the order of 100 nm. Aggregate chains act as nucleation sites for the formation of multilayers of graphene upon the hBN substrate. Bilayers and above nucleated in this manner were laterally small on these samples, on the order of 200 – 300 nm, as seen in Figure 5.8. As aggregates have been previously observed to form early in the growth process, prior

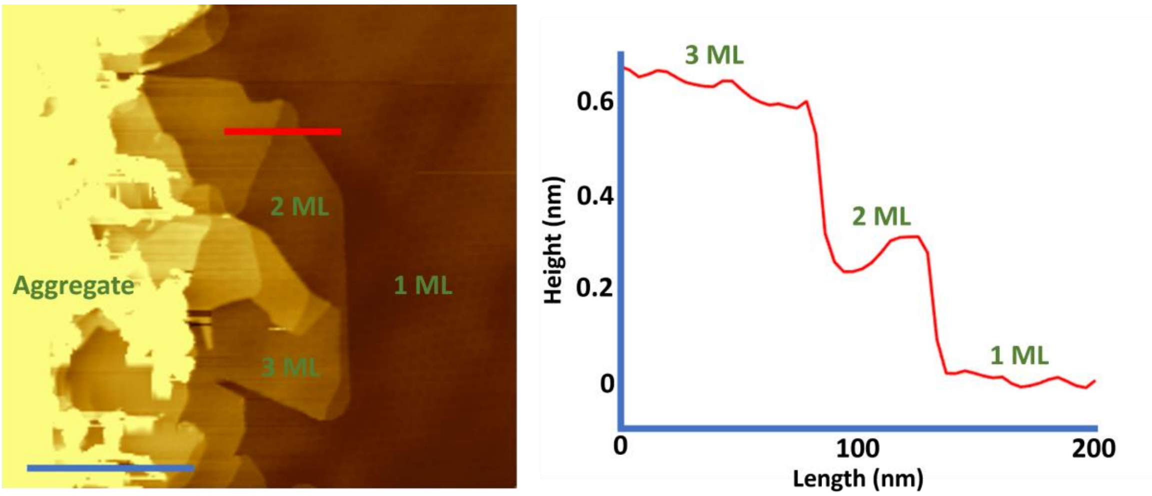

Figure 5.8 – An AFM height image presented of the edge of a graphene terrace with a scale bar of 300 nm. On the left edge of the image a chain of aggregates extends from the bottom to the top of the image, appearing bright and without feature due to the large scale compared to the adjacent few-layer material. A profile taken along the red line in the image is shown, on which the multilayers are identified. After a full growth cycles multilayers of material nucleated here exhibit domains around 250 nm in scale, much smaller than the several micron scale of the terrace.

to the formation of a complete graphene monolayer, the nucleation and growth rate of the multilayer graphene layers must be slower than the monolayer under these conditions.

The composition of the aggregates has previously been shown to differ between the two earlier carbon sources. The nature of the aggregates can be investigated with Raman spectroscopy, as will be shown in the next Section. Additional differences observed between those previous sources include the position of the aggregates as the growth front of the monolayers progress. It was observed that the aggregates were identified at the centres of the growing islands from the graphite filament sublimation source, likely acting as nucleation sites seeding the monolayer [16]. By comparison, the aggregates appeared at the edges of growth fronts from the atomic source. In both instances high concentrations of aggregate formation across the final terraces of the graphene monolayer are observed. This can be compared to the monolayer graphene terraces produced with the e-beam source. In this source relatively large regions, several hundred nanometres up to one or two microns, are largely free of aggregate presence, as seen in 5.4 a) and 5.6 a).

## 5.6 Raman Observations of the Monolayers and Aggregates

Raman spectra have been acquired from the surfaces of the hBN flakes after graphene growth. Monolayer graphene exhibits several peaks in the range of 1200 cm$^{-1}$ to 3000 cm$^{-1}$, with relative intensities, peak positions, and full width half maxima (FWHM) dependent on the defect density amongst other properties. Previous studies of the Raman spectrum of graphene and other graphitic materials have identified the peaks consistent with a pure, defect-free domain of monolayer graphene. As described in Chapter 3, these peaks are the G and 2D at 1600 cm$^{-1}$ and around 2700 cm$^{-1}$, with the 2D peak position depending on the frequency of the incident laser [127]. Where defects or edges are present the D peak at around 1350 cm$^{-1}$ is also observed with a position being dispersive with laser energy. On pure hBN the strongest peak is observed at 1370 cm$^{-1}$ close to that of the D peak of graphene/graphite and often obscured by it, with no other significant peaks observed in the 1200 cm$^{-1}$ to 3000 cm$^{-1}$ range considered here [131].

The relative intensities of the D and G peaks have been previously shown by Tuinstra and Koenig to provide a means for measuring the local defect concentration of a graphene sample [149]. Comparing samples with low disorder, such as smaller defect concentrations and larger domains, with those exhibiting high disorder material, such as greater defect and sp$^3$ site presence, shows that the Raman spectrum has undergone many changes [126]. As disorder increases a broadening of the D and G peaks occurs until distinct peaks cannot be resolved, and a broad low-intensity peak around 2700 cm$^{-1}$ is observed.

Figure 5.9 consists of Raman, optical, and AFM maps of overlapping regions on a single G/hBN flake. The Raman map has been presented by setting the colour dependent on the intensity of the D peak

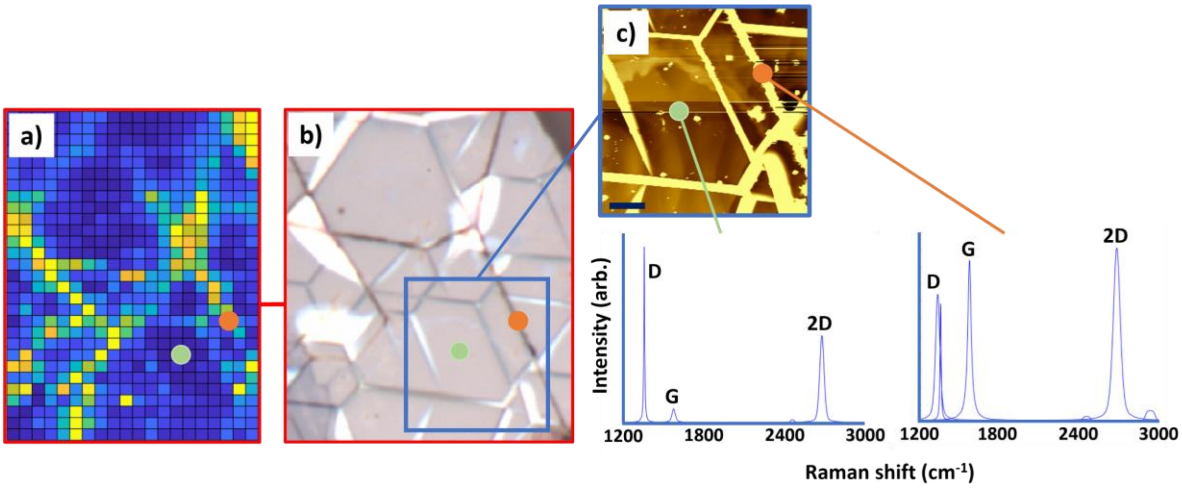

Figure 5.9 – A Raman map is presented in a) of a hBN flake, the optical image of which is shown in b). The map depicts the observed intensity of the D peak at each position and is 20 µm wide by 30 µm tall. An AFM image taken of the region identifies an aggregate string at the orange point of each image, and a terrace at the green position. The full fitted spectra obtained at these positions are presented, created with Voigt profiles. Namely, at the position of the aggregate string the intensity of the G peak is comparable with that of the D and 2D peaks, and the hBN peak is comparable with that of the D, allowing for splitting into the two individual peaks. Finally, higher intensity peaks are observed at 2456 cm$^{-1}$ and 2934 cm$^{-1}$ at the aggregate string position.

at each point, with blue corresponding to the lowest values. The 10 µm AFM image identifies the presence of aggregates on the flake, consistent with the increased intensity of the D peak seen in panel a). The spectra observed over the terrace and aggregate strings identified in panel c) are presented. Several differences between the two spectra can be observed and are discussed below. Firstly, the relative intensities of the D and G peak differ significantly. The relative intensities between the G and 2D peak also vary, in addition to the presence of a peak at 2950 cm$^{-1}$ on the aggregate spectrum. We will first consider the importance of these intensity variations, and then move the discussion onto FWHM and position changes between the spectra and the import of such.

Tuinstra and Koenig described the impact of the finite grains and defects of the monolayer on the relative intensities of the D and G peaks, $I(D)/I(G)$ [149]. Lucchese confirmed this relation for a 514 nm excitation source, finding that $I(D)/I(G)$ is approximately equal to $145/L_D^2$ where $L_D$ is the average inter-defect distance [150]. However, this relation will break down where when $L_D$ is smaller than the average travel distance of an e-h pair before phonon scattering, estimated at ~3.5 nm, or when domains are small [126]. As described by Ferrari and Basko for crystal sizes or inter-defect distances on the order of ~3 nm the relation changes and *I(D)/I(G)* becomes negatively dependent upon the defect concentration [126]. As well as the inversion of the *I(D)/I(G)* this regime exhibits changes in the position of the G peak, specifically a downshift from around 1600 cm$^{-1}$ towards 1510 cm$^{-1}$. As this downshift is not observed for the G peak of the aggregate spectrum shown in Figure 5.9 this implies that the low defect-density domain is being observed in this spectrum.

The relative intensities of the G and 2D peak, *I(G)/I(2D)* are a key signifier of the presence of monolayer graphene [127]. The position, intensity, and FWHM of the 2D peak are known to depend upon the number of graphene layers due to splitting of the pi orbitals due to interlayer interactions [151]. These parameters can therefore be used as another metric to establish the presence of monolayer graphene, and the presence of multilayer graphene nucleated close to the aggregates as identified previously in this Chapter. By comparison with the work of Hao et al. the relative intensities of the G and 2D peaks on the terrace appears consistent with the single monolayer, whereas that at the aggregate position is closer to tri-layer or greater [151]. The FWHM of the fitted 2D Voigt profile on the terrace is equal to 38.1 ± 0.1 cm$^{-1}$, between the estimate for the monolayer and bilayer. When the same spectrum is fitted to a Lorentzian profile the measure of quality of the fit, the reduced chi squared value, is greater, signifying a worse fit. The FWHM of the Lorentzian fit, 33.4 ± 0.2 cm$^{-1}$, is closer to the expected value for the monolayer and corresponds to the fit used by Hao et al. It should be noted that the improved quality of the Voigt fit is likely due to the presence of three components to the 2D peak. The positions of these component peaks have previously been shown to depend on the surface strain, observed as the period of the moiré pattern between the graphene and hBN [15]. As such, the spectrum is consistent with the presence of a moiré period of ~ 14 nm, or unstrained, aligned, graphene on hBN. Comparatively, the FWHM at the aggregate position is 61.6 cm$^{-1}$, corresponding to 4-layer graphene. Both spectra exhibit 2D peak positions around 2685 cm$^{-1}$, consistent with other spectra taken from the sample, equivalent to that expected of the single-monolayer. This may arise due to the relatively small scale of the multilayer material about the aggregate position.

In Albar et al. the FWHM of the G peak was interpreted as a metric for establishing the composition of aggregates of G on hBN [16]. Graphitic aggregates exhibit G-peak FWHM of ~35 cm$^{-1}$, compared to 76 cm$^{-1}$ FWHM from the amorphous C aggregates. The Voigt-fitted G peaks observed on samples grown with the e-beam source exhibit FWHMs 30 and 38 cm$^{-1}$, consistent with an assigned graphitic aggregate composition.

### 5.7 Summary

In this Chapter analysis of surface features from the deposition of graphene on hBN flakes was presented. Comparisons were made between these samples, deposited with the use of an e-beam sublimation source for the carbon material, and previous samples making use of two earlier sources relying on other sublimation mechanisms. E-beam source samples produced large monolayer domains of graphene rotationally aligned with the hBN substrate were observed exhibiting moiré periods at or above 13.6 nm. Moiré periods above 13.6 nm were assigned to the presence of strain in the graphene surface post growth as a result of cooling and differences in the thermal expansion coefficients of the graphene and hBN. Cracks in the graphene layer were observed, revealing the hBN flake beneath, and aligned with the armchair and zigzag directions of the aligned and unstrained lattice. The cracks are assumed to arise as a tension release mechanism for the acquired strain.

Chains of graphitic aggregates were observed to form on the surface, extending up to ~ 100 nm vertically from the surface. Raman comparisons between monolayer graphene material and that of the aggregates showed few differences, which provokes several possible interpretations. More research is required to separate the Raman spectra of the multilayers present around the aggregates from that of the aggregates themselves.

Prior sources, as discussed in Chapter 2, were too unstable for the reliable production of graphene on the small scales necessary for integration into lateral heterostructures as described in the subsequent Chapter. The stability of the e-beam source and the quality of the monolayer graphene sheets produced provide a pathway for the production of lateral G/hBN heterostructures from MBE. In the following Chapters this source will be used in the production of lateral G/hBN heterostructures on HOPG substrates. These structures will be presented, alongside the influence on the production of supramolecular networks. Without this e-beam source these following studies would not have been possible.

# Chapter 6: hBN/G/hBN Heterostructures Grown by MBE

## 6. Overview

2D lateral heterostructures exhibit the potential for low-dimensional electronic devices with a superior performance to vertical heterostructures. In Chapter 2 recent studies of the properties and production of lateral heterostructures of TMDCs were discussed. The unique semi-metallic properties of graphene and its inherently 2D nature have resulted in multiple studies of the integration of graphene into planar structures. The similar lattice of hBN to graphene leads to the possible production of high-quality lateral heterostructures with clean interfaces. Under optimal growth conditions the similarity of the lattices of hBN and graphene results in low defect density hBN/G heterojunctions and minimal 3D growth, as was demonstrated for hBN on graphite in Chapter 4.

In the previous Chapter we demonstrated the production of domains of hBN of varying sizes on graphite with high temperature molecular beam epitaxy (HT-MBE). The resulting hBN domains exhibited facetted grain edges following crystallographically significant directions, which is beneficial for the production of quality 2D interfaces. Earlier work at Nottingham has established the production of graphene on bulk hBN flakes with MBE [15,16]. A natural progression of this work was then to grow hBN and G heterojunctions by alternating the growth of hBN and G with HT-MBE on a common substrate. Successive growth cycles of G and hBN on HOPG have been carried out and in this Chapter an analysis of the resulting surface is presented. The process used to produce the samples is presented in 6.1. The morphology of the surfaces has been analysed with AFM as described in 6.2. Following this

**Table of Samples**

| Sample Name | Temp ($^{o}$C) | Time (mins) | Material Deposited |
|---|---|---|---|
| I | 1390 | 90 | hBN |
| II | 1390 | 1 | G |
| III | 1390 | 10 | hBN |
| IV | 1390 | 90 / 1 / 10 | hBN/G/hBN |

Table 6.1 – This table contains a list of all samples from which data has been presented. Samples I to III are the same substrate after the first, second, and third depositions, respectively. The growth conditions differ between III and IV due to the intentional removal of the system in III after each growth stage for imaging, and the purely vacuum conditions between growth cycles for sample IV.

discussion, features of the heterostructure domains, and the distinct ribbons of 2D materials, are separately presented in Sections 6.3, through to 6.6. The production of lateral heterostructures of graphene/hBN in other studies is discussed in Section 6.7.

### 6.1 Summary of the Production Process

Graphene and hBN were grown on HOPG substrates using the epitaxial systems described in Chapter 3. HOPG substrates were cleaned prior to entry into the system in the same manner as previously described, followed by introduction to the chamber for the first hBN deposition. From this point the growth procedures for the samples from which data is presented in this Chapter differ from the process described previously. The first sample produced, labelled as I, was allowed to cool to room temperature after a first hBN growth cycle using a substrate temperature of 1390$^{o}$C and a growth time of one and a half hours. Images of the sample surface were obtained with AFM and the sample was subsequently loaded into the graphene deposition chamber. The current to the carbon e-beam source was not varied between samples as described in Chapter 5.1. This decision was made to the relatively small quantity of material being deposited, however it should be noted that this may have resulted in slightly different graphene deposition rates between the two graphene depositions used here. Graphene growth was carried out at 1390°C for 1 minute, to form the sample, labelled II, before removal, imaging, and replacement into the hBN chamber for a further cycle of growth. The second cycle of hBN growth was carried out at 1390°C for 10 minutes (sample III), and AFM images acquired after removal from the vacuum system. In this manner three sets of images were acquired from the same substrate at different stages during the production of the heterostructure. For comparison another sample, IV, was produced using the same growth cycles as for I-III, though without any removal to atmosphere between growths. A comparison of images of these sample provides information about the effects of atmospheric exposure during the growth cycle. The growth conditions of the four datasets are presented in Table 6.1.

## 6.2 AFM Methodology

As in Chapter 4 conductive and tapping mode AFM have been used to investigate the surface morphology of the produced samples. Images acquired using the topography and phase channels obtained with tapping mode allow for the identification of large scale (100 nm – 15 µm) surface features and provide the necessary information for distinguishing the two materials. The conductive mode images were taken on scales from 5 nm to 1 µm, and images taken at the lower end of that range reveal the lattice period of the surface.

Profiles taken over the surface sometimes exhibit differences in the apparent height of a monolayer. Lateral precision in AFM can be limited for topographically-high surface structures by the sharpness of the tip, but the uncertainties in vertical precision are less commonly discussed in the literature. As discussed in Chapter 4, the apparent differences in the monolayer heights arise from material-dependent probe-surface interactions which can be modified by properties such as the elastic constant or friction coefficients of the surface [137]. Changes in these properties and others result in variations in the equilibrium tip position under the constant force conditions used in contact-mode

AFM. In tapping-mode AFM choice of cantilever and operational parameters have also been shown to impact the apparent height of islands on the surface [152–154]. These interactions modify the apparent vertical height of the surface at each point, but do not impact the lateral uncertainty of the measurements. This phenomenon prevents accurate measurements of multilayer thicknesses as discussed in the previous Chapter. Presented images still provide valuable measurements of the width of the 2D epilayer bands, identification of monolayer height steps, and readings of the morphology of the surface.

### 6.3 Morphology of the Lateral Heterostructures

Samples produced by the successive depositions of boron/nitrogen and carbon exhibit adjacent domains of monolayer growth. Lateral heterojunctions consisting of two monolayer hBN sheets connected by a graphene strip have been grown on samples III and IV. Morphologies of the samples were identified with AFM images, the features of which are shown in this Section.

Figure 6.1 depicts the successive cycles of the growth of one sample with AFM images selected to show the monolayer sheets. The initial hBN growth carried out on the HOPG substrate resulted in hexagonal growth consistent with the findings in Chapter 4, as shown in Figure 6.1 a). These large hexagonal domains follow the armchair direction of the underlying graphite lattice. In image b) the

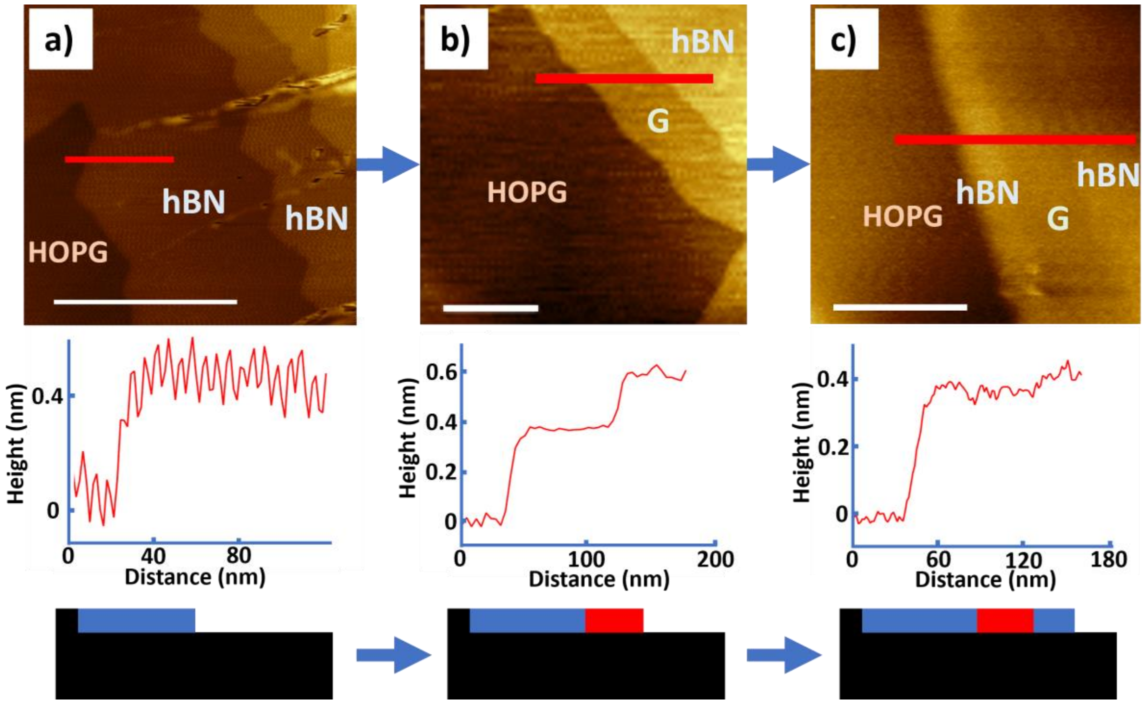

Figure 6.1 – Three AFM topography images have been obtained from the sample datasets I, II, and III and are shown in a), b), and c) respectively. The images, with scale bars of 200 nm, 100 nm, and 100 nm respectively, have been presented to convey the observed changes in the monolayers after each growth stage. Profiles taken along the red line in each image are presented below. The profiles have been taken over the successive heterostructure development, and show that the structure is confined to the monolayer. As established in Chapter 4 and seen in a), the substrate growth temperature used in the production of these samples results in hexagonal hBN growth. In b) the graphene epilayer is seen to follow the edge direction of the hBN monolayer, but undergoes a transtion to a different direction at corners in the hBN domain. Diagrams presented beneath the profiles show a simple model of the surface at the stage of growth in the image above. In these diagrams the graphite substrate is represented in black and the graphene and hBN monolayers in blue and red, respectively.

hBN growth can be observed to have templated the growth of a graphene epilayer with a constant average sheet width over the sample and an edge direction parallel to that of the hBN growth. In c) a final hBN monolayer has grown laterally from the graphene strip. The properties of the ribbons and the heterojunction are covered in later Sections in greater detail.

The growth processes of samples III and IV are distinct due to the repeated removal of III from the vacuum system between growth cycles and the lack of this removal for IV. Images of heterojunctions on these samples are presented in Figure 6.2 with profiles presented below. Broadly the two surfaces are very similar, with no aggregate formation at the lateral interfaces formed by the second and third growth cycles. The second growth cycle hBN sheet widths are similar between samples III and IV, and are identified as 25 ± 3 nm and 33 ± 2 nm, respectively. As identified by the profiles in Figure 6.2 the graphene sheet width between the two samples appears to differ. In sample III the width of the graphene sheet was 57 ± 4 nm and from sample IV the graphene sheet width was 25 ± 2 nm. The

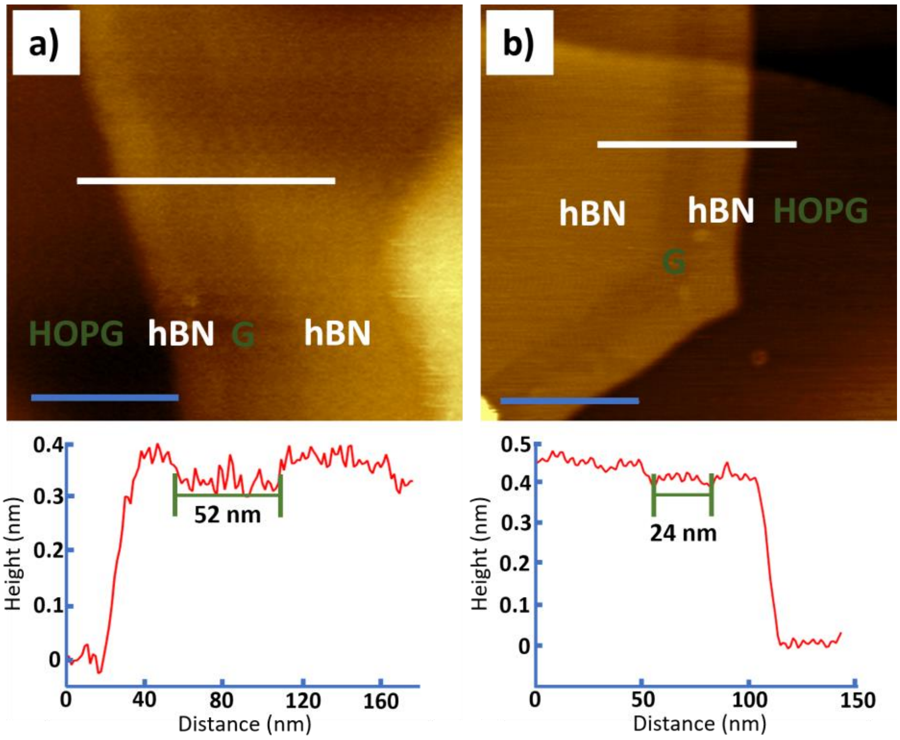

Figure 6.2 – Topography images taken of samples III and IV with tapping mode AFM are presented with scale bars of 500 nm to compare the surfaces. These samples differ as III was removed from the vacuum between each growth stage, whereas IV remained in vacuum until all growths were completed. Aggregates were not observed to have formed at the lateral interfaces formed by the second and third growth cycles, such as the interface between the graphene strip and the second hBN monolayer growth. As has been identified in the profiles beneath the images, sample III exhibits an ~50% greater graphene epilayer width than IV. This is likely due to the small growth times used in production and the possibility for error in the estimate of material deposited.

differences in sheet widths could arise from differences in the deposition rate of the carbon between samples. The source current was not raised between successive carbon depositions to counter for the loss of deposition rate that arises, as was described in Chapter 5.1, as only a small quantity of source material was sublimated. As a result, small changes in the deposition rate from sample to sample may be expected. Removal of the sample from the system does not appear to result in a reduction in the quality of the deposited material or impact the formation of the clean heterojunctions.

As shown in Figure 6.3, in some instances second-layer islands of hBN are found after the first growth cycle. Where this has occurred, there is the potential, after subsequent growth cycles, to compare the rates of growth on hBN and HOPG. In Figure 6.3 a) a 750 nm square AFM image is presented in which two hBN monolayers have grown in the first growth stage as necessary for comparison. The colour contrast of images b) and c) has been normalised to highlight the second and first monolayers, respectively. The first and second monolayers are also labelled in b) as 1ML and 2ML, respectively.

The graphene epilayer does not exhibit any changes between nucleation on the HOPG or hBN monolayer substrates. The sheet widths of both graphene ribbons are the same, within experimental error, and measured to be 25 ± 2 nm, the value measured elsewhere on the sample, and the external edge direction remains parallel to the edge of the hBN monolayer. Unlike the graphene ribbon the width of the second hBN growth does differ substantially between the two surfaces. The average sheet width of the hBN layer grown on an underlying hBN layer was measured to be 20 ± 1 nm, substantially smaller than that of the hBN grown directly on the graphite substrate, 34 ± 1 nm. This substrate

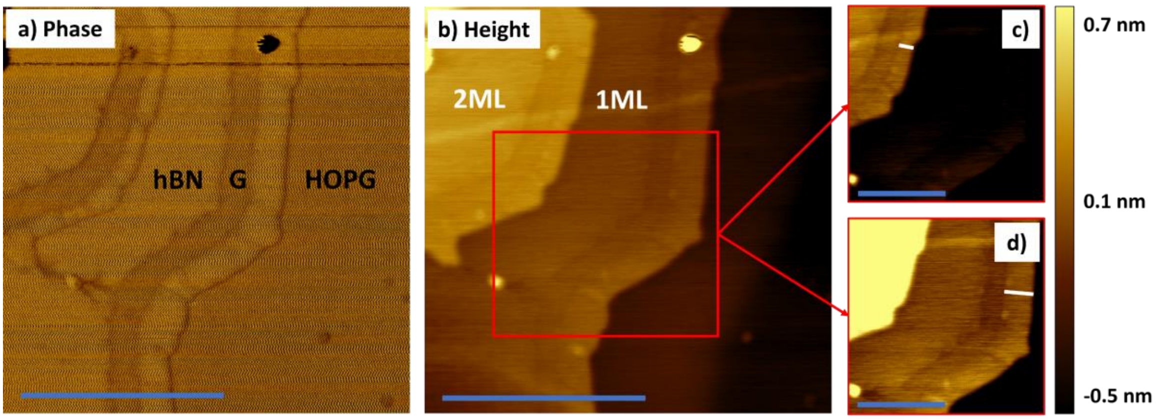

Figure 6.3 – Images a) and b) are phase and topography AFM images exhibiting a region consisting of two layers of the lateral heterostructure with scale bars of 200 nm. Image a) has been provided to identify the presence of the hBN, graphene and HOPG within the region. A contrast bar to the right provides a scale to measure differences in the height of the surfaces and shows that b) covers two monolayers with some aggregate presence. On the top left of the image a bilayer island of hBN has provided a nucleation point for a graphene epilayer on an underlying hBN layer. Growth over the graphite substrate versus that of the hBN monolayer can be compared by looking at images b) and c). In these images, with scale bars of 100 nm, no differences in the graphene layer are observed. Significant differences in the width of the encapsulating hBN epilayer are found and are identified with white lines in b) and c) and are measured at 20 ± 1 nm and 34 ± 1 nm on average, respectively.

dependence on the hBN growth may arise from one or several sources, such as a greater surface binding energy of the HOPG over the hBN surface to one or both hBN constituents.

To summarize, successive growths of hBN, G, and hBN on a HOPG substrate resulted in lateral heterojunctions of hBN/G/hBN. The G growth and the subsequent hBN growth form lateral heterointerfaces at the edges of pre-existing islands of previous growths with no independent nucleation on terraces. Comparison of samples III and IV show no significant differences between samples grown with or without removal from the vacuum system between growth cycles. AFM of the resulting structure shows no difference between the heterojunctions grown on a hBN monolayer compared to those on the HOPG substrate, but for a reduction in the sheet width of the hBN ribbon formed from the third growth cycle.

### 6.4 Surface Features after the Carbon Deposition

Carbon deposited on the surface after the first hBN deposition accumulated as monolayer growth and as amorphous aggregates. It may additionally have incorporated into the BN aggregate structures. All observed monolayer growth was seen to have nucleated from the edges of the hBN monolayers deposited in the first stage of growth. The graphene ribbons exhibit highly consistent thickness around the hBN domains and follow the contours of the hBN epilayers to a high degree. The carbon aggregates formed on the hBN monolayer, running perpendicular to the graphite steps.

Energetic particles in an epitaxial growth system can damage and etch surfaces. The nitrogen precursor was directed onto the surface as a plasma. These energised particles could result in the stripping of carbon from the graphene ribbons during the growth of the final hBN ribbons, resulting in a reduced graphene sheet width. Figure 6.4 a) and b) compare images of samples II and III, that is pre-

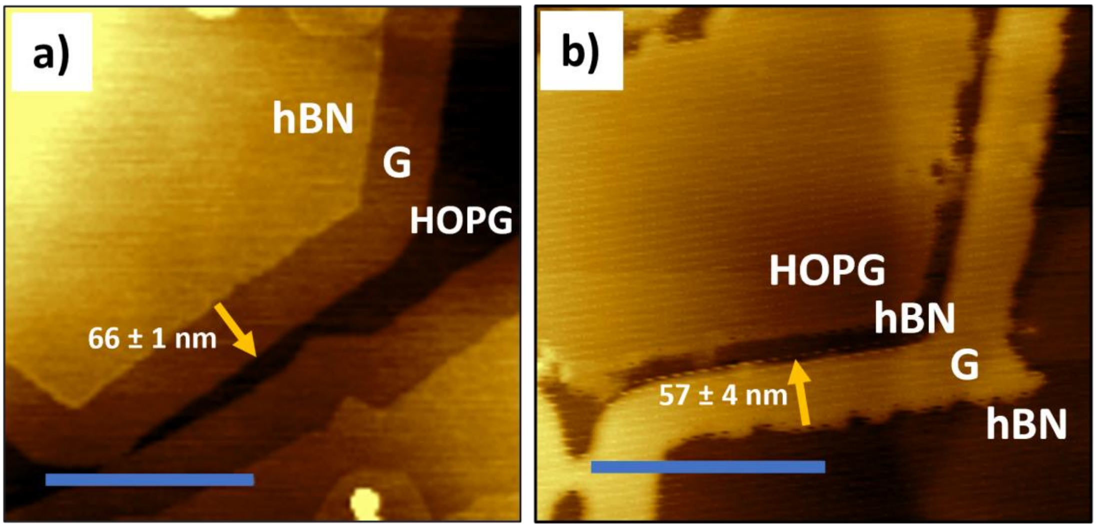

Figure 6.4 – Two topography images taken of the surface of II and III with scale bars of 200 nm. The selected images show that the thickness of the graphene ribbon has reduced during the growth of the final hBN layer. The light colouring of the graphene strip and HOPG in image b) arise from accumulation of contaminants observed on samples after several weeks of exposure to atmosphere. Contamination of the hBN is not observed. After the graphene ribbon was grown an average graphene sheet width of 66 ± 1 nm was obtained from a) and other images. As is labelled on b) an average graphene sheet width of 57 ± 4 nm was measured after the final hBN growth.

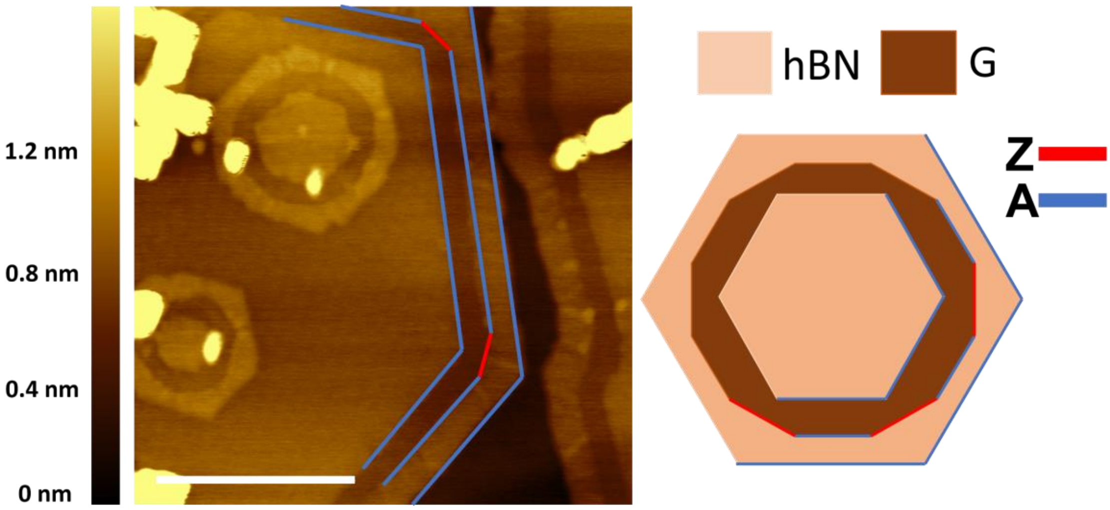

Figure 6.5 – On the left is shown a tapping-mode image from the surface of IV with a scale bar of 200 nm. The image exhibits two instances where the hBN/G/hBN structure has nucleated on top of an underlying hBN layer. Blue and red lines annotated onto the image are displaying the direction of the edge of the epilayers, where blue edges are armchair-oriented, and red are zigzag. The diagram to the right of the image displays the preferred edges of the epilayers and the resulting island shape. This island shape compares favourably with the second-layer islands observed on the left of the AFM image.

and post-growth of the final hBN layer. The graphene ribbons and the direction of growth are identified by blue arrows in images a) and b). The average sheet width of the graphene ribbons taken from images of these two samples show a width reduction of ~14% after hBN growth. This may arise from etching of the graphene ribbon or chemical modification of the edges during the growth of the hBN epilayer. Should the removal of material from the graphene monolayer be due to damage from ionised particles one would expect holes or heavy defect presence in the remaining graphene. This is inconsistent with the appearance of the graphene as can be seen in the images of Fig. 6.4 b) and Fig. 6.5 the graphene strips. Incorporation of boron nitride into the graphene ribbon during the growth may also result in an apparent reduction of the G sheet width in AFM images, though this is not expected to occur due to a lack of phase mixing in these growth conditions [155].

The orientation of the edges of 2D materials can result in very different electronic properties or chemical functionalization [25,156]. For example, nanoribbons of graphene with armchair or zigzag external edges exhibit differing band gaps and the presence of spin-polarized edge states in the case of the zigzag edge [157]. Figure 6.5 shows a tapping-mode image of sample IV accompanied by a diagram highlighting the direction of the edges identified from the image. The hBN monolayer was observed to exhibit armchair-aligned growth at the substrate growth temperatures used. The graphene ribbons follow the crystallographically-significant armchair and zigzag directions. Over the majority of the hBN domain edges the graphene ribbons follow the armchair direction. The outer edge of the graphene ribbons transitions to the zigzag direction at corners of the hBN domains. The resulting thickness of the graphene ribbon is 25 ± 2 nm on sample IV as previously described. The behaviour remains consistent where two hBN domains lie in proximity.

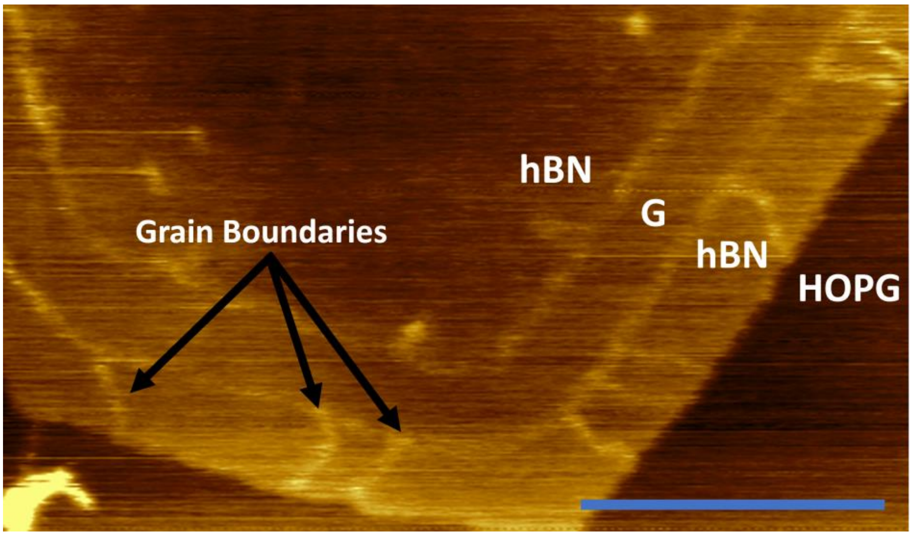

Figure 6.6 – A topography AFM image of the edge of a domain from sample IV is presented. The scale bar is 100 nm and the image is annotated to identify the materials of the epilayers and the grain boundaries visible in the presented structure. The grain boundaries are highlighted to show the relatively high presence of these boundaries on the outer hBN epilayer compared to the lack of boundaries on the hBN domain originating from the first growth cycle.

### 6.5 Properties of the Second hBN Ribbon

The second hBN growth cycle results in a thin, monolayer hBN ribbon extending laterally from the graphene epilayers present on the surface. In this regard the final hBN growth behaves similarly to the first in that the 2D growth requires graphitic steps for nucleation sites. Sheet width and other morphological differences exist between the results of the two hBN growth cycles, namely the prevalence of grain boundaries and lack of interfacial BN aggregates on material from the second hBN growth cycle.

Figure 6.6 presents a topography image from a hBN/HOPG sample. Grain boundaries are visible as lines of increased height. Compared to the hBN domain at the top of the image, from which the two epilayers have subsequently grown, there is a very high concentration of domain boundaries on the second hBN growth. These images show the high density of domains occurring in the early stages of the first hBN growth. Some of these domains are entirely enclosed by aligned neighbours, resulting in a relatively small number of large domains as the growth progresses. As shown in the images of Figure 6.7 enclosed domains arise in wider hBN sheets where an initially high density of grains has been reduced as the growth progresses by the presence of faster growing neighbouring domains. Some of the grain boundaries on the external hBN ribbons of samples III and IV should be expected to form small, enclosed domains with longer growth times. With this considered the density of hBN grain boundaries on HOPG from the second growth cycle is 15 ± 7 boundaries/μm$^{-1}$, higher than that the 11 ± 2 boundaries/μm$^{-1}$ observed in the single hBN monolayer growth of other samples, implying a higher nucleation rate of hBN along the graphene ribbons than from the HOPG steps.

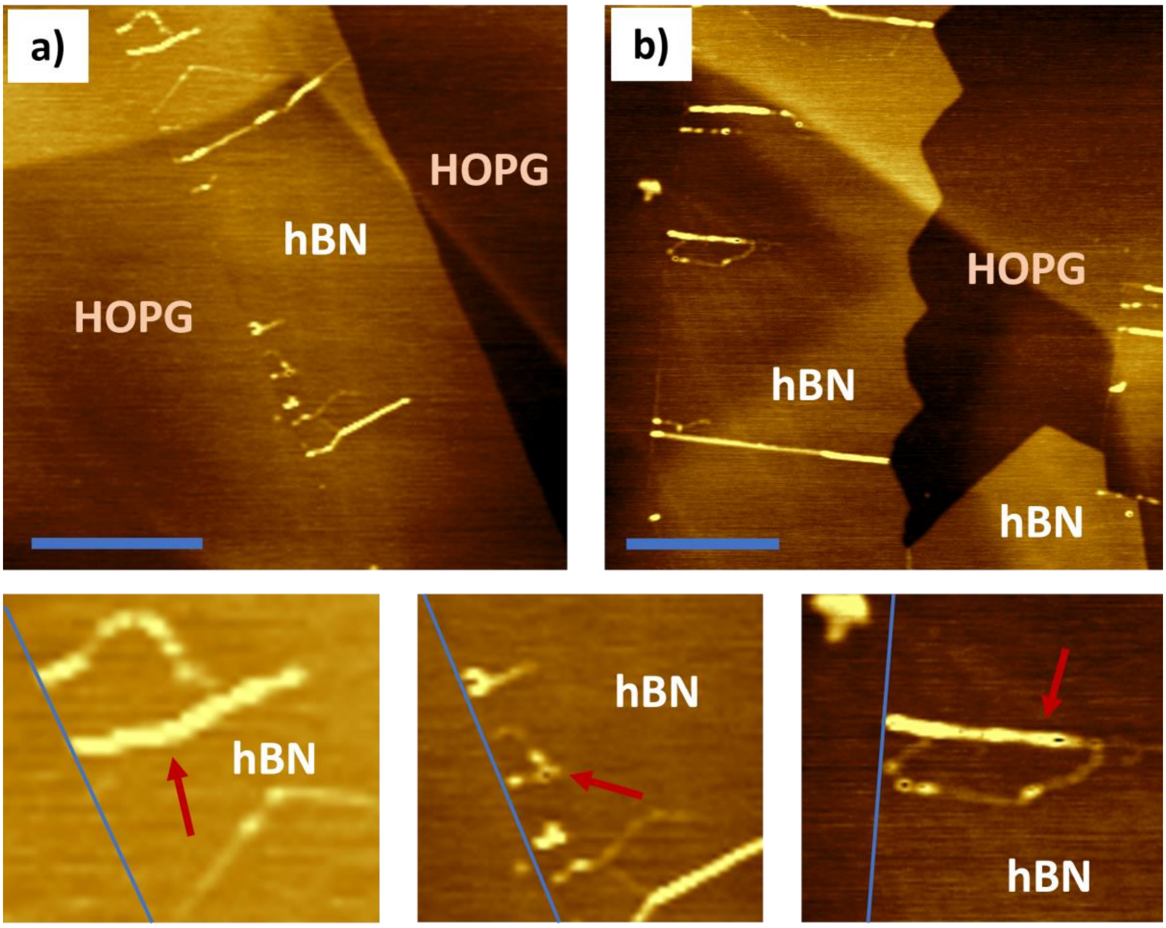

Figure 6.7 – Two tapping-mode AFM images presented from a hBN/HOPG growth with a longer growth time. The images are a) and b) are from two separate regions of the same sample. Differences are observed in the density of grain boundaries close to the HOPG step and close to the edge of the hBN growth. Some domains are enclosed as growth continues, leading to a reduction in the grain boundary density nearer to the growth edge. The three images presented beneath are zoomed in regions of the images above, highlighting the positions of the enclosed domains. Blue lines are provided to identify the position of the HOPG step.

### 6.6 Aggregate Formation and Growth over Multiple Growth Cycles

Amorphous carbon and BN aggregates were observed on all samples discussed here. As observed in Chapter 4 on samples of hBN/HOPG, the BN aggregates have formed chains of material along steps on the graphite surface. BN aggregate structures are observed on all samples, forming after the first hBN growth and retained after subsequent depositions. The exact material composition of the BN aggregates is unknown and the volume of the aggregates varied between growth cycles, during which the composition may have altered.

Amorphous carbon aggregates were observed to have formed on grain boundaries of the hBN monolayer during the graphene growth cycle. Figure 6.8 shows AFM images from samples II and IV to compare BN grain boundaries from the first hBN growth cycle before and after the additional growth cycles. Profiles from the two images highlight a significant increase in the height of the boundary,

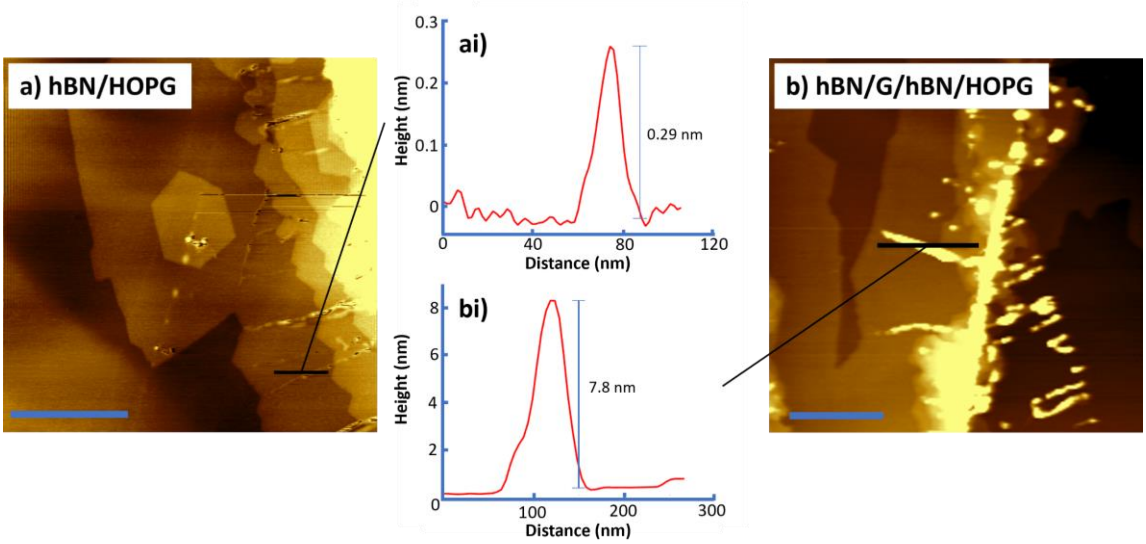

Figure 6.8 – Images a) and b) display tapping-mode AFM images with scale bars of 250 nm. The image in a) was taken from sample II and image b) from sample IV. The images have been selected to compare hBN grain boundaries before and after the second and third growth cycles. Profiles across a grain boundary from each image are presented in ai) and bi). The profile in ai) shows a grain boundary height of ~0.3 nm. In comparison, bi) shows a height of 7.8 nm, more consistent with the height of the amorphous BN aggregates across HOPG steps than with the prior grain boundary. The carbon deposition is believed to have formed carbon aggregates on the grain boundaries of the hBN domains produced in the first growth cycle.

signalling the presence of additional material. The height of the grain boundary observed on sample IV in Figure 6.8 b) is more consistent with the heights of BN aggregate material on the HOPG steps than that of the hBN grain boundaries. This is explained by the formation of carbon aggregates on hBN grain boundaries during subsequent growth cycles.

As discussed in Chapter 4, the grain boundary of adjacent hBN domains grown on a HOPG substrate likely consists of 5|7 or 4|8 defects. The energy cost of these pairs and the resulting reduction in stability of the monolayer at the grain boundaries introduces the possibility for 3D structure formation such as that observed here.

## 6.7 Discussion of G/hBN Lateral Heterostructures Produced with MBE and CVD

CVD-grown lateral heterostructures of graphene and hBN have been produced by other groups with a variety of substrates and growth processes. As a result of different production processes and substrates, the investigated samples exhibit distinct surface morphologies, limiting direct comparisons. Common substrates for CVD production of graphene/hBN heterostructures include Ni(111) and Cu(111), which have previously proven effective for the growth of graphene and hBN separately [158–161].

Successive deposition of carbon and hBN is one of the most common methods for the CVD production of lateral heterostructures [70,159,162,163]. In Wei et al. (2020) islands of hBN were deposited on a Ni(111) substrate and were subsequently surrounded by a monolayer of graphene [159]. The order of deposition of the graphene or hBN monolayers were shown to significantly impact the alignment of the domains of the two materials. With significant misalignment the interfaces between the domains will exhibit a greater defect concentration and clean merging between neighbouring domains cannot occur. As such growth of the second deposited layer should proceed by attachment from existing domains to encourage alignment, with steps taken to reduce independent nucleation on terraces for the second growth cycle. This was achieved in Wei et al. by the deposition of hBN prior to graphene [159]. It was also noted by Kim et al. (2013) that the temperatures necessary for the deposition of graphene are high enough that significant etching of the deposited hBN material can occur on some substrates [70,163]. For the MBE-produced samples investigated in this thesis all monolayer growth was observed to form by attachment to previous monolayer depositions and steps in the HOPG substrate. Successive depositions of carbon and boron/nitrogen onto HOPG with HT-MBE resulted in monolayer lateral heterojunctions of hBN/G/hBN. Thin ribbons of graphene and hBN have been grown and encircle large hBN domains, nucleating along the edges of the 2D epilayers formed in the previous growth cycles.

Strong alignment between domains is also known to depend upon the choice of substrate, with a greater likelihood of alignment where the lattice parameters of the substrate and grown material are similar. As such production of graphene/hBN heterostructures on a hBN substrate was carried out by Liu et al. (2013) [72]. This was achieved by etching a hBN film with argon ion etching, with few-layer graphene grown to fill the etched pits in the hBN. As a result of the process atomically sharp lateral interfaces are produced with the etching process allowing for the formation of designed lateral features, such as those necessary for electronic devices. The study did not aim to produce monolayer graphene or features smaller in scale than 100 nm, so the possibility of smaller, monolayer devices has not been demonstrated. The heterostructure production method presented here provide a means to control the scale of features to a much finer degree, down to a few to 10s of nanometres. This is, in effect, exchanged for the very high degree of control at the larger scales provided by the etching process, pointing to potentially distinct use cases for the two methods.

The width of the lateral interface between the graphene and hBN can be controlled by the CVD growth process, with finite interface widths meaning regions where the hexagons of hBN or graphene incorporate atoms of C or B/N respectively [160,164]. This mixing region between the two different material monolayers are dependent on the presence of growth constituents left over from the previous growth cycle during the subsequent growth. For example, fragments of the borazine constituent left on the surface after hBN growth will mix with the C species deposited for the graphene growth to produce a mixed hBN/graphene alloy at the interface between the two materials. This arises from the chemical equilibrium within the CVD system during growth, though processes have been developed to mitigate or control the formation of the mixed alloy region [164].

In Liu et al. (2014) the researchers explore the deposition of hBN/G lateral heterostructures with a thin, zigzag boundary [162]. This was achieved by deposition on an Ir(111) substrate with successive depositions of the precursors. By producing material with a consistent edge direction further study can be carried out to explore the electronic properties of the ribbons of the heterostructure. Graphene ribbons with zigzag boundaries are known to exhibit semi-metallic properties with a non-zero magnetic moment. In the results presented above, the hBN growths exhibit edges following the armchair orientation of the atomic lattices. The graphene ribbons were observed to follow the hBN edge from which they are nucleated and transition to a zigzag orientation at corners of the hBN domain.

The two highly distinct processes resulting from direct deposition of hBN/G onto metallic substrates, and the growth of graphene from etched hBN result in entirely different morphologies comprised of lateral heterostructures of G/hBN. These heterostructures in turn differ from the MBE-produced samples studied in this work, resulting in distinct applications as the field of lateral heterostructure production progresses.

# Chapter 7 – Growth of CA.M/PTCDI on G/hBN Heterostructures

## 7. Introduction

Molecular self-assembly is a process by which spontaneous aggregation of molecules to form coherent supramolecular networks, either in solution or on a substrate, is observed. The structures are bonded via non-covalent interactions, such as the hydrogen bonding observed in the CA.M structure [165]. Ongoing studies vary the environment and molecular precursors to explore the generated nanostructures [166]. The growth of supramolecular networks depends heavily on the choice of molecule to deposit and the substrate. Monolayer depositions of these structures may benefit the production of ultrathin electronic or optical devices with reliable, cheap, and quick deposition methods. Single monolayers consisting of a hexagonal network of cyanuric acid-melamine (CA.M) have previously been deposited on black phosphorus (bP) and hexagonal boron nitride (hBN) [112,167]. These monolayers were shown to form a hexagonal lattice with adjacent sites occupied by alternately by CA and M molecules. The monolayers were observed to inhibit the degradation of a bP surface during exposure to atmosphere. PTCDI has also been deposited on hBN substrates, which were shown to influence the photoluminescence spectra of the molecules when compared to in solution. In this Chapter depositions of these molecular structures have been performed on graphite substrates and hBN/graphite heterostructures. The formation of the monolayer structures of CA.M and PTCDI was identified and the influence of the presence of hBN on the graphite surface, with its differing bonding structure and interaction with solvents, is expected to modify the deposition of molecular layers.

The morphology of the resulting heterostructures were investigated primarily with AFM. Photoluminescence spectra are shown where the spectral peaks are resolved. In Section 7.2 the deposition processes for the CA.M and PTCDI layers are described. This is followed by an overview of the analysis methods in 7.3, with more details available in Chapter 3. Sections 7.4 and 7.5 discuss the resulting structures present on the graphite and hBN/graphite surfaces, with comparison made to depositions on hBN where appropriate. An overall summary of the results is provided in Section 7.6.

## 7.1 Deposition Processes for CA.M and PTCDI

Graphite and hBN/HOPG substrates were cleaned prior to molecular deposition. The hBN/HOPG substrates referred to were produced with MBE and exhibit features such as those described in Chapter 4. The graphite substates, consisting of 1 $cm^2$ HOPG chips, were initially exfoliated to remove an outer layer of graphite and any accompanying contaminants. The HOPG substrates were then cleaned by toluene immersion and dried with $N_2$ as described in Chapter 3.2. This was followed by heating the HOPG substrates in a tube furnace at 300°C for 4 hours, a process that was also carried out for the hBN/HOPG substrates. This was necessary for both sets of substrates as the graphene surface was observed to accumulate a contaminant layer over time, which may have impacted on any depositions.

After these cleaning processes were complete the substrates were considered ready for molecular deposition. CA.M layers were deposited by immersion as described in Chapter 3, with immersion times varied between 30s and 60s. Immersion times of 60s were established by Korolkov et al. to result in a complete monolayer on exfoliated hBN flakes [167]. The lower immersion times were expected to result in partial monolayers of the CA.M structure. Given the formation of triangular islands of CA.M for partial coverage on hBN flakes, a lower immersion time was intended to aid in the identification of the CA.M on the HOPG substrates.

PTCDI depositions were carried out by sublimation in the dedicated vacuum system described in Chapter 3. For each of the samples discussed here a quantity of PTCDI material corresponding to 0.3

ML was deposited. Due to the presence of CA.M on some of the measured substrates the temperature of the substrate during PTCDI deposition was limited to 50°C as higher temperatures were observed to remove the CA.M layer from the surface.

The selection of samples exhibited in this Chapter involve deposition of combinations of CA.M and PTCDI on HOPG and hBN/HOPG as described above.

### 7.2 AFM and PL

Atomic force microscopy (AFM) measurements were taken on the surfaces of all samples presented in this Chapter. Tapping-mode and contact-mode AFM images were obtained on scales ranging from 100 nm up to several microns. Topographic and phase images were analysed with the Gwyddion open-source program to identify the presence of the supramolecular structures and their morphologies. Contact-mode AFM can be used to brush aside material from a position on the substrate. This process can be used to identify the thickness of the layer at a position on the surface. The tip is brought close to the surface and force applied until material is displaced by the tip. Due to the relative weakness of the binding of some molecular layers on the surface, the graphite surface is relatively unaffected by the passage of the tip, while the molecular layer can be moved. This results in a distinct feature on the surface in which material has accumulated at the edges of the square imaged region along the edges perpendicular to the motion of the tip. Rotating the image plane by 90° for a subsequent scan can then reveal the thickness of the layer on the graphite substrate.

All topography images are presented with scale bars or profiles to aid in identification of the height of surface features. The absolute values for phase images cannot be simply interpreted, so scale bars for these images are not included for the sake of simplicity.

In addition to the AFM data, photoluminescence (PL) spectra were obtained from each sample. Spectra were obtained with the laser system described in Chapter 3 with acquisition times of 5s with measured wavelength ranges from 475 nm to 1100 nm. For molecules deposited on graphite substrates the resulting spectra will exhibit no peaks in the PL spectra. This occurs due to quenching of the luminescence resulting from the migration of excitons in the molecules into the neighbouring graphite [168]. For the majority of samples presented here this quenching was sufficient to eliminate all peaks in the luminescence spectrum. By separating the luminescent molecules from the graphite it has previously been shown that the impact of the graphite in quenching the molecules can be reduced [168].

## 7.3 Surface Features of CA.M and PTCDI on HOPG Substrates

A comparison can be performed between the morphology of deposited CA.M and PTCDI layers deposited on the HOPG and hBN/HOPG substrates. Depositions on hBN flakes exfoliated onto silicon chips have previously shown that the lattice of the hBN substrate has some influence on the growth of PTCDI islands [169]. Islands of PTCDI deposited by sublimation onto the hBN were found to orient primarily along nine directions separated by $20^{o}$, consistent with some preferred orientations impacted by the underlying lattice. CA.M structures form on hBN with the growth of triangular monolayer islands with island edges misoriented from the lattice by $3 \pm 1^{o}$ [167]. This is also true for the formation of the CA.M structure on HOPG substrates as demonstrated by Zhang et al., who found that a moiré period for CA.M on graphite consistent with a misorientation of $1.4^{o}$ between the two lattices [111].

The alignment of islands of deposited material is preferable for the formation of complete monolayers with minimal defect presence. Misalignment is conducive to the production of grain boundaries as islands expand into each other, as was described for hBN material in Chapter 5. Initial depositions of the CA.M and PTCDI layers onto clean HOPG substrates exhibit similar, yet distinct, morphologies to those observed on hBN substrates. Figures 7.1 a) and b) depict CA.M and PTCDI depositions carried out on HOPG substrates with methods identical to that used for the hBN substrate [167,169]. For the deposition of the PTCDI the substrate temperature was held at $50^{o}$C during growth. PTCDI islands shown in Fig. 7.1 b) are needle-like with a definite preferred direction, similar to that observed on

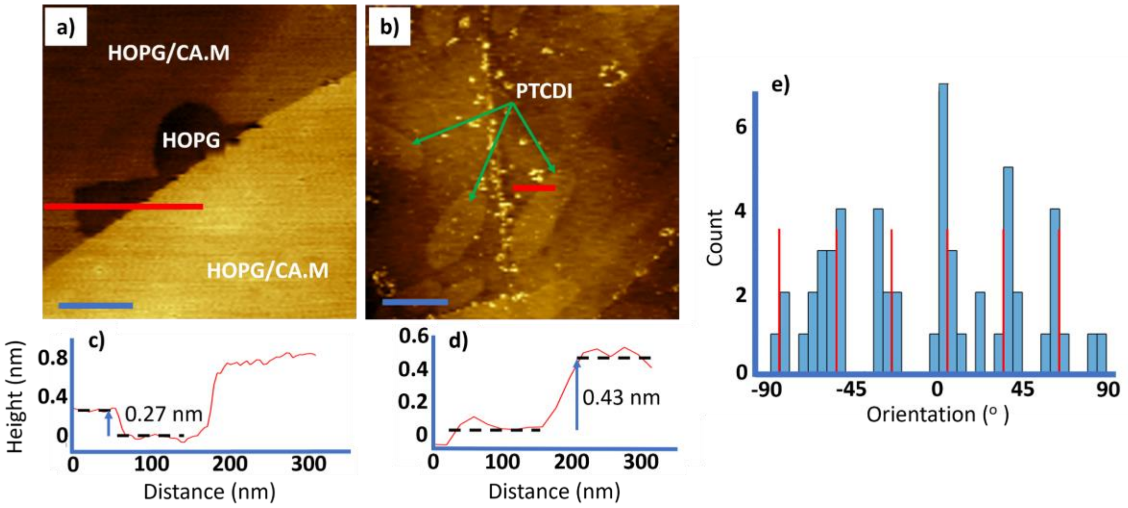

Figure 7.1 – Images a) and b) are topography images, obtained with tapping-mode AFM, of HOPG substrates on which a CA.M or PTCDI deposition has been performed, respectively. Scale bars for these images are 100 nm and 500 nm, respectively. The CA.M and PTCDI monolayers are identified by the height difference measured between the monolayer and the graphite surface, as depicted in the profiles shown in c) and d). Orientations of the PTCDI islands relative to the vertical axis of a larger image of this region were collated and a histogram of these orientations is presented in e). A non-uniform distribution of orientations is obtained, which conforms approximately with six peaks separated by 30°. This can be explained by the hexagonal symmetry of the graphite lattice, implying the substrate has had some influence on the formation of the PTCDI islands.

hBN. On hBN substrates the ratio of the minor to major island dimensions were consistently found to be 0.15 ± 0.06 independent of the growth substrate temperature [169]. The islands observed of PTCDI observed on HOPG instead exhibit a minor to major ratio of 0.37 ± 0.07. The PTCDI islands on HOPG additionally exhibit a different distribution of orientations to that previously observed on hBN. Islands on hBN were found, in the doctoral thesis of Dr James Kerfoot, to prefer one of nine directions, each separated by approximately 20° [169]. On graphite, as presented in Fig. 7.1 e) six dominant orientations are observed. These six orientations, separated by ~30° could correspond to crystallographically significant directions of the underlying graphite lattice. In addition to the monolayer islands of PTCDI, some aggregate material has accumulated on the graphite around steps on the surface, seen in Fig. 7.1 b) as bright spots in the image. The intended coverage of the deposition, with the average thickness of deposited material measured by QCM, was for 0.3ML of PTCDI. The measured monolayer coverage was ~15%, with some of the remaining material accumulating into the aggregate structures. The CA.M deposition, an image of which is present in Fig. 7.1 a), appears to have deposited a near-complete monolayer of the CA.M network with an immersion time of 60 s, comparable to that expected from a deposition onto a hBN substrate. In Fig. 7.1 a) a profile has been taken covering two steps in the surface, which has been displayed in Fig. 7.1 c). The step on the left, between the CA.M monolayer and the exposed HOPG, was found to have a height of 0.27 ± 0.03 nm. The step on the right, leading up to the bright region in the image, is believed to cross onto a step in the HOPG with a complete CA.M monolayer. The height of this step was measured at 0.73 ± 0.03 nm, which is consistent with a bilayer step in the graphite with a CA.M monolayer grown above it.

Depositions of PTCDI on CA.M on hBN substrates were carried out by Kerfoot et al. [170]. On the hBN substrate a PTCDI deposition onto the CA.M layer results in the formation of needle-like islands oriented along three directions oriented with 60$^{o}$ angular separations. The photoluminescence spectrum of the resulting CA.M/PTCDI structure on the hBN surface differs from that of PTCDI deposited directly onto hBN. Namely, the 0-0 transition peak is shifted by ~0.045 eV due to the presence of the CA.M layer. This shift could be understood as caused by one of several mechanisms, as described by Dr James Kerfoot in his doctoral thesis. The presence of the CA.M layer on the hBN may change the polarizability of the substrate, or changes in the refractive index of the substrate could lead to a reduction in the screening of on-surface transition dipole moments. As was described earlier the luminescent spectral response of the PTCDI is expected to be quenched by the HOPG such that the 0-0 peak and potential shift would not be observed.

In Figure 7.2 a topographic AFM image and associated analyses from the successive depositions of CA.M and PTCDI onto a HOPG substrate are presented. The CA.M layer was deposited by immersion in a solution of cyanuric acid and melamine, described in Section 7.2, with an immersion time of 60s and a resulting monolayer coverage of ~90%. The PTCDI was deposited with an intended coverage of

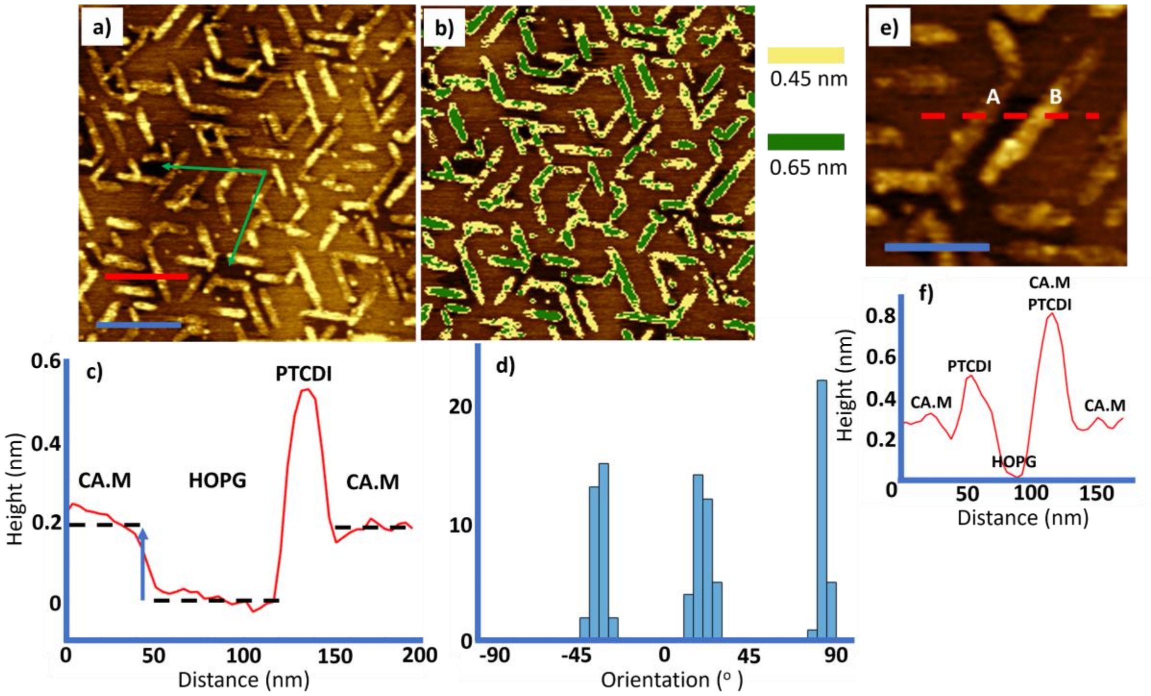

Figure 7.2 – A topography image is presented in a) with a scale bar of 200 nm of the surface of a graphite substrate on which CA.M and PTCDI have been deposited. The CA.M monolayer has covered the majority of the surface. Green arrows point to darker regions, believed to be exposed HOPG. The needle-like islands of PTCDI have deposited both directly onto the HOPG substrate and onto the CA.M surface, which is highlighted in b). In image b) material with a height of 0.45 nm above the HOPG plane has been coloured yellow, while that with a height of 0.65 nm is shown in green. From this can be seen that the height of the PTCDI islands appears to vary by the observed height of the CA.M layer. A profile is presented in c) taken along the red line in a) showing the different heights of the materials on the surface. The orientations of the islands relative to the vertical have been collated and presented in a histogram, presented in d), showing that the PTCDI aligns are highly aligned along three directions. The image in e) and corresponding profile in f) are provided to show an island of PTCDI on HOPG and one on CA.M directly adjacent. In the topography image the former appears darker, and it is confirmed to lie directly on HOPG using the profile in f).

0.3ML, as measured with a QCM during growth. The coverage measured with AFM comes to 27%, comparable with the intended deposition. Needle-like islands of PTCDI have formed on the HOPG and CA.M surfaces, which are highlighted in yellow and green in Fig. 7.2 b). The height of these islands on the surface varies between and often along the islands, as has been identified by the coloration in Fig 7.2 b) with the yellow regions reaching heights of 0.45 nm and the green of 0.65 nm. As this difference in height is equal to the thickness of the CA.M monolayer identified by the profile in Fig 7.2 c) this is assigned to PTCDI islands residing directly on the HOPG, or on the CA.M monolayer, respectively. Due to the near complete monolayer presence of the CA.M the growth of the PTCDI on and off the CA.M monolayers may arise from displacement of the CA.M molecules as a result of a greater affinity for the HOPG substrate for the PTCDI than that of the CA.M layer during the growth process.

In Fig. 7.2 d) the orientations of the PTCDI islands in a) have been collated and presented as a histogram. The orientations of the islands are observed to align along three dominant directions, separated by rotations of $60^{o}$. This distribution is consistent with a strong influence of the CA.M network on the accumulating PTCDI islands during growth. Whether the PTCDI material is aligned with armchair or zigzag orientations of the HOPG or the CA.M lattices cannot be inferred from the data. However, comparison to the depositions of the separate materials on the HOPG substrate shows that the presence of the CA.M monolayer has caused a reduction in the number of preferred orientations of the islands from six to three. This reduction is significant as it implies the selection of a single preferred crystallographic direction for the PTCDI islands, influenced by the CA.M network. The aspect ratio of the islands is also altered by the CA.M monolayer, measured at 0.28 ± 0.05, whether the material has deposited on the CA.M monolayer or adjacent to it, as depicted in Fig. 7.2 b). Comparing Figures 7.1 b) and 7.2 a) the presence of the CA.M layer encourages a more uniform distribution of the PTCDI material. That is the aggregates of PTCDI material are not observed in the AFM images when CA.M is present, and the observed coverage of 0.27 ML is much closer to the deposited quantity of material than the 0.15 ML observed in the absence of the CA.M layer.

### 7.4 Deposition of the CA.M and PTCDI Monolayers on HOPG/hBN Substrates

With the demonstration of hBN monolayer formation on HOPG via MBE, as described in Chapter 4, it has become possible to investigate the deposition of these molecular layers on epitaxial combinations of HOPG and hBN. Differing chemical properties of the graphite and hBN lattices, such as the

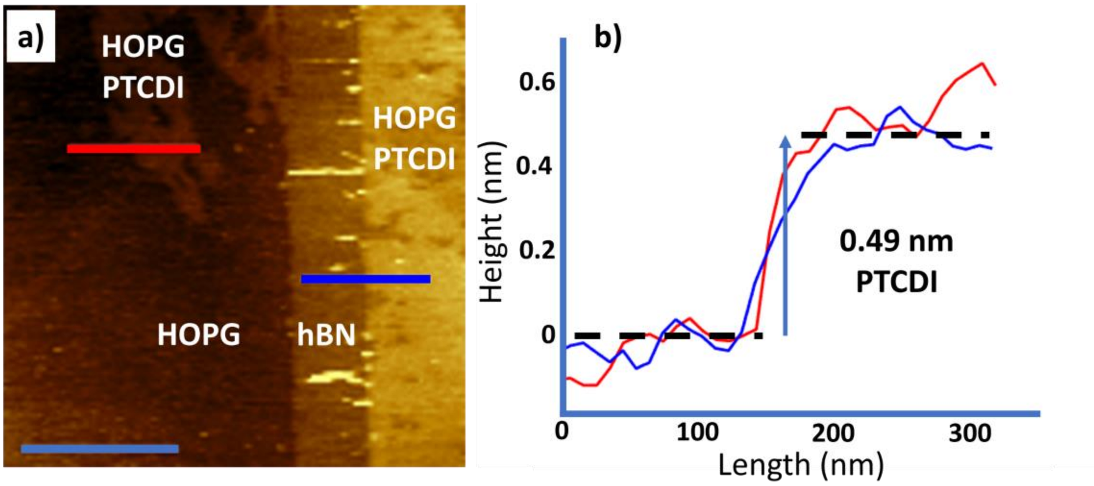

Figure 7.3 – A topographic images of the surfaces of hBN/HOPG substrates after a PTCDI deposition. In the image in a) the scale bar represents 400 nm and PTCDI material appears to have deposited in a less structured form to that observed previously on HOPG. The PTCDI material is not observed to have grown on the hBN monolayer, preferentially forming solely on the HOPG where it has been indicated by the profiles. A hBN monolayer running vertically down the centre of the image does not appear to have accumulated any material during the PTCDI deposition. Two profiles from a) are presented in b) showing that the height of the deposited molecular layer is consistent with the previously identified height of the PTCDI monolayer as was also seen in Fig. 7.2.

polarization of interlayer orbitals, can be expected to result in changes to the accumulation of the deposited molecules. For example, the surface of graphite is known to be hydrophilic when clean, but quick to accumulate a thin layer of hydrocarbon material upon exposure to ambient air, rendering the surface hydrophobic [171]. These properties will influence the deposition of molecules from solvents, such as the molecules of the CA.M network.

In Figures 7.3 and 7.4 the results of independent depositions of CA.M and PTCDI on separate hBN/HOPG substrates are presented. Observations of the surface after these depositions show significant changes to the behaviour of the growing molecular layers between the hBN and HOPG, and between these substrates and the pure HOPG substrates. In Figure 7.3 a) a topographic image of a PTCDI deposition on hBN/HOPG is depicted. The PTCDI material has only accumulated on the graphite surface. The material has not deposited in the needle-like islands previously observed, but has instead

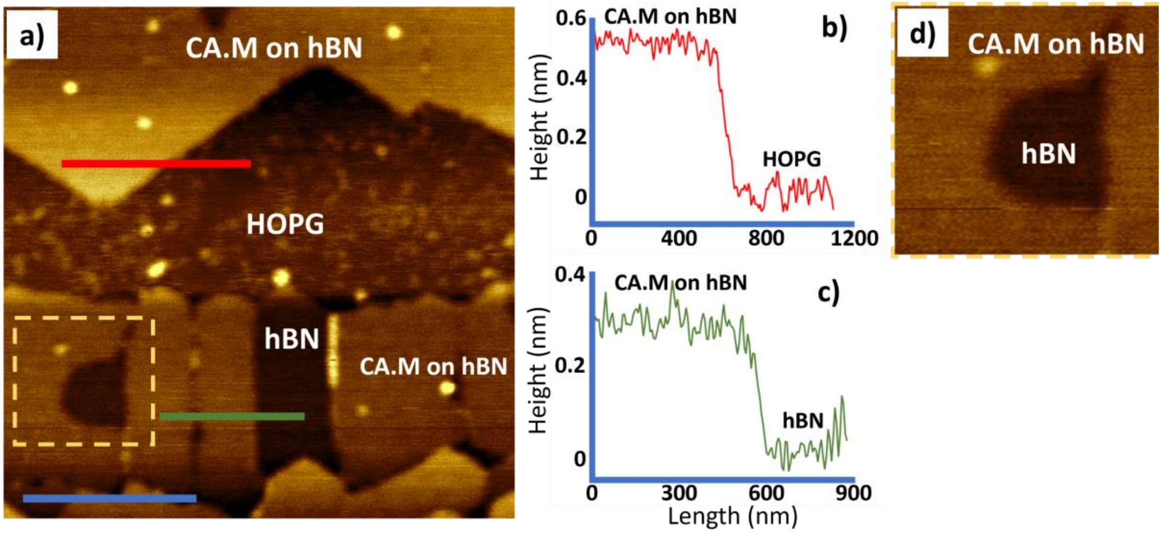

Figure 7.4 - A topographic image is presented from a hBN/HOPG surface after a CA.M immersion deposition of 60s with a scale bar of 200 nm. A monolayer of material is observed to have formed on the hBN surface, identified. Material has also deposited on the HOPG surface, though the layer is rougher with a RMS roughness of 56 ± 7 pm compared to 40 ± 6 pm for the material on the hBN. This surface roughness may be a result of the presence of amorphous CA.M material. Two profiles are depicted in b) and c) respectively. In b) step height from the CA.M/hBN surface onto the HOPG is shown. The height difference shows that the CA.M layer is terminating at the edge of the hBN. The profile in c) shows a step between a CA.M layer on hBN and the adjacent exposed hBN step. In d) the small region dictated by the yellow square in a) has been enlarged to highlight positions on the hBN surface with and without the CA.M monolayer.

grown as large islands lacking in regular form. The height of the PTCDI layer is consistent across this surface and with the 0.35 nm height of the monolayer from previous depositions.

Figure 7.4 a) provides a topographic AFM image from the surface of a CA.M/hBN/HOPG sample. In Fig. 7.4 d) a region highlighted in yellow from the image in a) has been enlarged to show an area of the hBN monolayer on which the CA.M has deposited, with a hole in the CA.M layer exposing the hBN material beneath. As can be observed from this image the CA.M material has accumulated in a near-complete monolayer on the hBN epilayers. The profile shown in Fig. 7.4 c) shows the height of the accumulated monolayer is 0.30 ± 0.04 nm. The layer on the hBN differs from the material accumulated on the HOPG layer, which exhibits a relative increase in roughness from 40 ± 6 pm to 56 ± 7 pm compared to the CA.M material on the hBN, implying the cyanuric acid and melamine molecules have deposited into an amorphous layer on the HOPG. The profile in Fig. 7.4 b) shows a height difference between the CA.M/hBN layer and the HOPG terrace of 0.53 ± 0.08 nm. As the hBN layer is of monolayer thickness and the thickness of the CA.M on the hBN has been identified as 0.30 nm this could imply that there is no material layer on the HOPG, which contradicts the conclusion drawn from the roughness of the HOPG surface. For both CA.M and PTCDI depositions on the hBN/HOPG substrates the accumulation of the growing layers has differed from that on HOPG substrates. The lack of PTCDI material on the hBN surface shows a greater affinity for the HOPG substrate and that molecules of PTCDI have thermal energy great enough to migrate from the hBN onto the HOPG during growth. The deposition of CA.M on the hBN monolayer has resulted in a complete monolayer separated by a single monolayer of hBN from the HOPG. As identified by the thickness of the hBN and CA.M material step onto the HOPG terrace it does not appear that any CA.M material has accumulated on the HOPG. Preferential accumulation of CA.M onto the hBN of the hBN/HOPG substrate, despite formation of a monolayer on the HOPG substrate, may arise due to differences in the relative hydrophilicities of hBN and graphite, or from migration of deposited molecules. Greater hydrophilicity of hBN during the immersion deposition encourages contact of the depositing molecules to the hBN layer, which could result in the lack of material observed on the graphite. The hydrophilicities of these surfaces are known to vary as a result of ambient exposure, so the relative hydrophilicities are not simply obtained [172,173]. Alternatively, migration of the CA and M molecules before accumulation into the network, and an energetic preference for the hBN substrate, could achieve the same effect.

Successive depositions of CA.M and PTCDI onto the same hBN/HOPG substrate show regular growth of the molecular monolayers of both networks on the hBN epilayers. As seen in Figure 7.5 a) needle-like islands of PTCDI are observed on the hBN surface, while these islands are not present on the exposed HOPG. As noted previously, without the CA.M layer no PTCDI accumulation was observed on the hBN monolayers, so it appears that the presence of the CA.M monolayer has influenced the deposition of the PTCDI onto this surface. The orientations of these PTCDI islands have been collated, as previously, and are shown in Fig. 7.5 c). The results show three dominant peaks in the island orientations relative to the vertical, separated by $60^o$ rotations. This orientation distribution is identical to that of PTCDI templated by CA.M on HOPG. It therefore appears that whether the PTCDI is deposited directly onto a HOPG or hBN/HOPG surface the islands can be templated by the presence of an adjacent CA.M monolayer. In addition, the presence of the CA.M monolayer on the hBN of the hBN/HOPG substrate promotes the growth of the PTCDI monolayer islands, where the PTCDI islands would not otherwise have accumulated. Profiles taken across PTCDI islands in these samples show that some material has deposited directly upon the hBN, and some atop the CA.M layer, similarly to

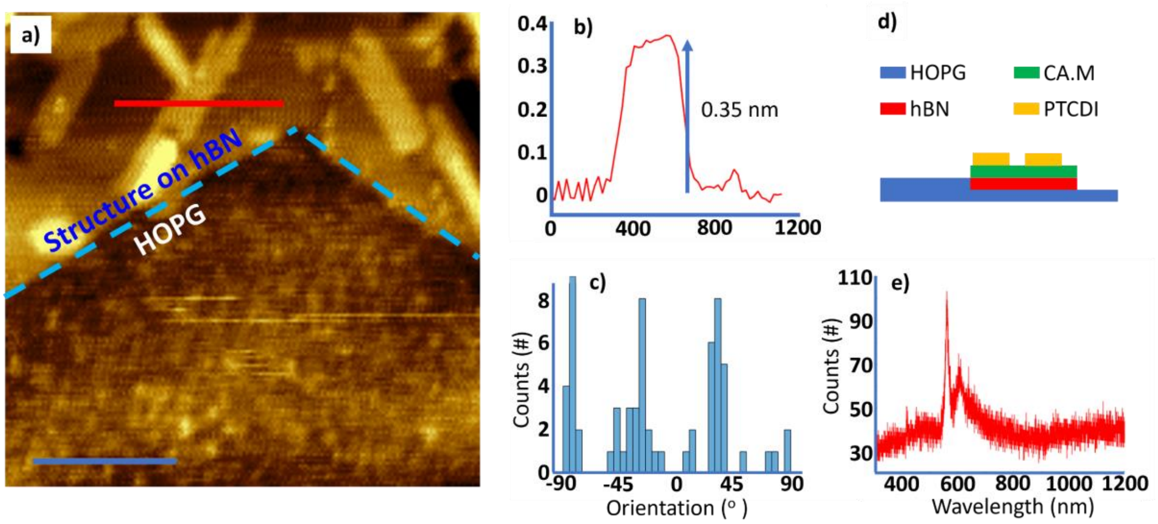

Figure 7.5 – A topographic image and analysed data from the surface of a hBN/HOPG sample on which CA.M and PTCDI have been deposited is presented. In the image presented in a) a hBN step on which the two molecular layers have accumulated is shown with an exposed HOPG terrace beneath it, with a scale bar of 100 nm. hBN epilayers grown extending from HOPG steps now exhibit a near-complete monolayer of CA.M and thin islands of PTCDI. A profile from this image is shown in b), taken across a PTCDI island on the hBN layer. The height of the layer is comparable with PTCDI that has accumulated adjacent to the CA.M layer, as opposed to atop it. The histogram in c) shows three prominent peaks in the collated orientations of the PTCDI islands. These peaks separated by 60° are consistent with the influence of the CA.M layer as noted before, though on a hBN monolayer rather than HOPG substrate. The diagram in d) is presented to show the current understanding of the structure on the surface after the final deposition. The material accumulated on the HOPG is not presented as the composition is unknown. In e) a PL spectrum from the surface is presented with non-zero observed intensity for two of the expected peaks from a PTCDI monolayer. The peak intensity is weak compared to the background noise of the system, likely as a result of the remaining quenching from the HOPG material.

the behaviour of the deposition of the two molecules on the HOPG substrate. Previously, it was observed that the nearby HOPG substrate encouraged migration of the PTCDI molecules away from the hBN, which has been remedied by the deposition of CA.M prior to the deposition of the PTCDI.

In Figure 7.5 e) the results of a PL measurement of the surface are presented. All of the previous samples presented here exhibited no luminescence peaks in the investigated wavelength range. The intensity of the PL spectra is still much weaker than that observed from monolayer PTCDI deposited on a hBN substrate. This is consistent with a reduction in the strength of the quenching from the HOPG surface. Kasry et al. have established the separation dependence of the quenching effect from graphene on molecular fluorophores [168]. The metallic nature of graphite, as opposed to the semi-metallic nature of graphene, means the results of this study are not one-to-one transferable to this work. Yet, a dependence of the quenching on the separation of the PTCDI from the graphite surface remains a feasible explanation for the increased intensity of the PL spectra from this sample. The dominant peak of the PTCDI PL spectrum is at 2.214 eV on hBN and is attributed to the 0-0 transition [169]. Previous studies have observed a blue-shift of this peak for PTCDI on CA.M/hBN of 0.045 eV. The peak observed in Fig. 7.5 e) corresponds to 2.212 eV, closer to that of PTCDI deposited directly on hBN that that on CA.M. The heights of PTCDI islands atop the hBN epilayers show that some islands have formed atop CA.M and some adjacent to it.

### 7.5 Summary

Growth of CA.M and PTCDI molecular monolayers on HOPG substrates has been performed. PTCDI islands similar in appearance to that observed on hBN substrates were observed, with a small change in the aspect ratio of the islands. Differences in the growth of CA.M and PTCDI molecular monolayers on graphite surfaces dependent on the prior growth of hBN were observed. The presence of the hBN epilayers encouraged formation of CA.M monolayers on the hBN, while PTCDI islands appear to have migrated to the HOPG surface during growth. Successive growth of CA.M and PTCDI on the hBN/HOPG substrates has been shown to result in a vertical heterostructure of CA.M/PTCDI on the hBN epilayers. This results in a reduction of the quenching of the photoluminescence spectrum, implying the potential for control of the photo-emissive properties of the PTCDI with control of the hBN thickness. CA.M has been shown to be necessary for the accumulation of the PTCDI islands on the hBN.

Further studies on the depositions of these molecules in the formation of supramolecular networks incorporated into van der Waals heterostructures should evaluate the changing impact of graphite-induced quenching as the thickness of the separating layer is increased.

# Chapter 8 – Summary

## 8.1 Summary of Work

The growth of monolayers of van der Waals materials is of current interest as a means of producing electrical and optical components on scales down to the monolayer. hBN and graphene have previously been identified as excellent candidates due to their differing electronic properties and similar lattices. In this thesis the growth of these materials and the formation of lateral heterostructures of the same were investigated. Proving the successful production of these heterostructures using MBE opens the possibility for further lateral heterostructure studies in future works.

In Chapter 4 an investigation into the high-temperature molecular beam epitaxy (HT-MBE) growth of hBN on a graphite surface was produced. Samples of hBN on HOPG substrates were grown with a range of substrate temperatures and growth times. The morphology of the hBN/G surfaces were analysed with tapping-mode and conductive-mode AFM. Any dependency of the properties of the hBN monolayers and BN aggregates on substrate temperature and growth times were investigated and suggestions for optimal growth properties identified.

Higher growth temperatures were shown to reduce aggregate formation and sheet growth. Minimal aggregate formation was observed on hBN/G samples produced at 1390$^{o}$C with non-trivial hBN sheet presence. The morphology of the hBN domains was observed to depend upon growth temperature, with an observed transition between triangular and hexagonal islands of hBN with increased substrate growth temperatures from 1080$^{o}$C to 1390$^{o}$C. The island shapes arise from the dominance of certain edge directions during the growth, with zigzag edges leading triangular islands and armchair to hexagonal. The transition between island shapes was hypothesised to depend on the relative prevalence of the B and N constituent material, which may vary with substrate temperature during growth. Different height steps on the graphite surface were observed to exhibit markedly different hBN sheet growth, with increased aggregate formation at multilayer steps and an associated increase in the presence of hBN sheets nucleated from the upper half of the step. The temperature-dependent MBE growth of hBN shows that edge direction of islands can be selected for. Simultaneous control over the presence of aggregates via an increase in temperature shows a path towards the fabrication of complete monolayer hBN material on the HOPG substrate.

In Chapter 5 a new source of carbon for the HT-MBE of graphene was investigated with comparisons made to earlier sources. The two earlier sources separately consisted of a sealed Ta tube filled with powdered carbon through which atomic carbon migrates before emission and a simple graphite filament which underwent Joule heating to produce the carbon beam. In this Chapter a carbon source, which operated with an e-beam directed into a crucible filled with carbon to produce a beam of material, was considered as an alternative for the reliable production of monolayer graphene.

This source was observed to produce reliable results of complete monolayer coverage of graphene on the hBN surface. Aggregate material was primarily clustered on cracks in the hBN substrate flakes, leaving hundreds of nanometres to micron-scale clean sheets of graphene. Moiré periods greater than the 13.9 nm unstrained maximum were observed in some of the resulting material. This was assigned as accumulated strain that may have accrued due to the different thermal expansion coefficients of hBN and G during the cooling after growth. This was observed in only some areas of the samples possibly due to the necessity for nearby pinning sites, the role here filled by aggregate clusters, or due to loss of strain by the formation of cracks in the monolayer. Carbon aggregate material was analysed with Raman spectroscopy and has been assigned to a graphitic composition as opposed to an amorphous composition, similar to the aggregates produced by the graphite filament source. The consistency of the produced graphene was identified as sufficient to begin studies on the production of lateral heterostructures comprising MBE-grown graphene and hBN. The accumulation and retention of strain post-growth is of potential interest as a result of the hypothetical opening of a bandgap in the material. The subsequent formation of electrodes on the surface in future would allow for the investigation of the non-uniform strain distributions and the impact on band structure.

Following on from the previous Chapter 2D lateral heterostructures of graphene and hBN were investigated. The similarities of the two lattices were expected to result in low defect density heterojunctions and minimal 3D growth. The deposited lateral heterostructures compare favourably with similar structures produced by CVD in previous studies. For example, subsequent ribbon growths were shown to nucleate from previous ribbons, a property favourable for minimising the formation of defects at interfaces. As the substrate temperature selected for the hBN growth was that considered preferable for minimising aggregate growth in Chapter 4 all hBN material was form with armchair edges, leading to hexagonal islands. Graphene islands were observed to show edge directions following that of the hBN material from which they nucleated, with zigzag edges forming at corners of the hBN hexagons.

The demonstrated multistep fabrication of alternating 2D materials on the HOPG substrate provides a pathway for the controlled fabrication of more complex hBN/G heterostructures, such as a periodic, lateral hBN/G superlattice. Small period lateral superlattices of G/hBN have been predicted to exhibit high thermoelectric conversion efficiencies, while remaining compact for potential 2D devices.

Depositions of supramolecular monolayers have previously been carried out on the hBN surface. Molecules such as PTCDI have been shown to form reliable structures templated by the hBN lattice and exhibiting a distinct photoluminescent spectrum. A graphite substrate was selected for this thesis to investigate the changes in the growth morphology arising from differing surface properties.

Islands of PTCDI were seen to form on graphite in a similar manner to that observed on hBN substrates. The minor/major dimension ratio of the islands was seen to be greater than that on hBN, and the PL spectrum of the molecules could not be observed. This was a result of the strong quenching effect of the graphite substrate on nearby fluorophores arising from its metallic properties. Growth of a CA.M/PTCDI vertical heterostructure was shown on the HOPG/hBN substrates produced in Chapter 6.

The separation of the PTCDI from the graphite reduced the intensity of the graphite-induced quenching and increased the intensity of the PL spectra, with a non-zero 0-0 peak observed from the PTCDI.

Van der Waals heterostructures consisting primarily of hBN, monolayer graphene, and graphite, were investigated. The growth of G and hBN with MBE on substrates of hBN and HOPG, respectively, were carried out and the resulting monolayers were studied primarily with AFM. The reliability and quality of the growth processes were investigated and some suggestions made for the formation of lateral heterostructures of these materials. Depositions of CA.M and PTCDI supramolecular networks were also carried out and show morphologies similar to those on hBN flakes for the hBN on graphite surfaces.

## 8.2 Future Work

Control of hBN edge direction as identified in Chapter 4, and the fabrication of edge aligned graphene in Chapter 6 provide the means to explore graphene nanoribbons with selected edge direction and controllable width. Other works on the edge states of graphene nanoribbons have shown that clean hBN interfaces preserve many of the interesting properties of zigzag edge, and this work shows that nanometre-scale orientation of the edges can be controlled by the growth system. However, the quality of the graphene ribbons must be more precisely determined, as it is known that perfect zigzag ribbons without misorientation along the length of the ribbon, are difficult to produce. To allow for strict comparison with theoretical study atomic resolution of the interface should be obtained, such as may be available from low-temperature STM study. Further to this the transport and paramagnetic properties of these ribbons should be established. To accomplish this transfer of the top layer of the grown G/hBN heterostructure from HOPG to an insulating substrate is necessary, or the alternative growth onto some insulating substrate.

Lateral heterostructures of graphene and hBN have been demonstrated to grow when alternating the material deposition. The formation of an enclosed ribbon of graphene via G/hBN and hBN/G interfaces shows the potential for the fabrication of 2D superlattices with controllable geometry. The fabrication of a G/hBN superlattice thermoelectric (TE) device requires fabrication, transfer, and measurement. With the possibility of fabrication shown the next step in the process requires a methodology for the transfer of produced material to an insulating surface and the subsequent fabrication of electrodes. A first attempt at this might rely on a polymer-based transfer using materials such as PMMA to selectively lift the uppermost layer. However, a polymer-free transfer method would be preferred.

Quenched molecules see use in detectors where the observation of emissions with fluorescence microscopy can inform on the state of the fluorescent system. Here, it was observed that the quenching of PTCDI molecules was mitigated by separation from a graphite substrate by the presence of a bilayer structure of monolayer hBN and CA.M. This could see potential as a metric for the measurement of contaminant accumulation of graphitic surfaces, though further study on the impact of separation on fluorescent intensity via the growth of hBN or CA.M multilayers will be necessary to identify the cause of the dependency.

# Appendix I – XPS of hBN on HOPG Samples

| Sample Temp (°C) | B (1s) % | C (1s) % | N (1s) % | O (1s) % | Si (2p) % | B:N Ratio |
|---|---|---|---|---|---|---|
| 1250 | 0.64 | 97.52 | 0.73 | 1.02 | 0.09 | 0.88 |
| 1250 | 2.23 | 94.01 | 2.91 | 0.77 | 0.07 | 0.77 |
| 1250 | 3.62 | 90.21 | 4.84 | 1.15 | 0.18 | 0.75 |
| 1080 | 2.15 | 94.59 | 2.67 | 0.54 | 0.06 | 0.81 |
| 1390 | 0.69 | 97.49 | 0.90 | 0.89 | 0.04 | 0.77 |
| 1520 | 0.30 | 97.78 | 0.56 | 1.22 | 0.06 | 0.54 |

Table 1 – X-ray photoelectron spectroscopy data taken from the samples presented in Chapter 4 is presented as the fractions of each sample consisting of the identified elements. Data was taken at the surface of each sample, where the large terraces of exposed HOPG can be seen by the large C percentage.

Wide-scan XPS surveys of the hBN/HOPG samples were obtained to identify any chemical contamination of the surface. Displayed here are the atomic percentages corresponding to the most significant constituent elements. Predominantly, the responses correspond to the expected surface of boron (1s) – nitride (1s) at a roughly 1:1 ratio and to a high carbon (1s) content. A B/N ratio ~0.8 on average is explained as an error introduced in the method used to obtain the atomic percentages. The sensitivity factors used to establish the percentages were taken from bulk hBN. In the bulk the photoelectrons sample different depths due to their different kinetic energies. In the thin films produced here the lack of depth sampling leads to a bias towards the lower kinetic energy peaks in the final percentages. Some contamination from oxygen (1s) and a small presence of silicon (2p) are also identified.

To obtain these measurement hBN samples were mounted on standard sample bars with copper clips and analysed with a Kratos AXIS ULTRA with a mono-chromated Al kα X-ray source (1486.6eV) operated at a 10 mA emission current and 12 kV anode potential (120 W). Wide scans at pass energy 80 eV and high-resolution scans at pass energy 20 eV were acquired on each sample at three positions. The analysis area was approximately 300 × 700 $\mu m^2$. The analysis chamber pressure was lower than 8 × 10-9 Torr. The peak areas in the wide scan data can be used to calculate the elemental atomic

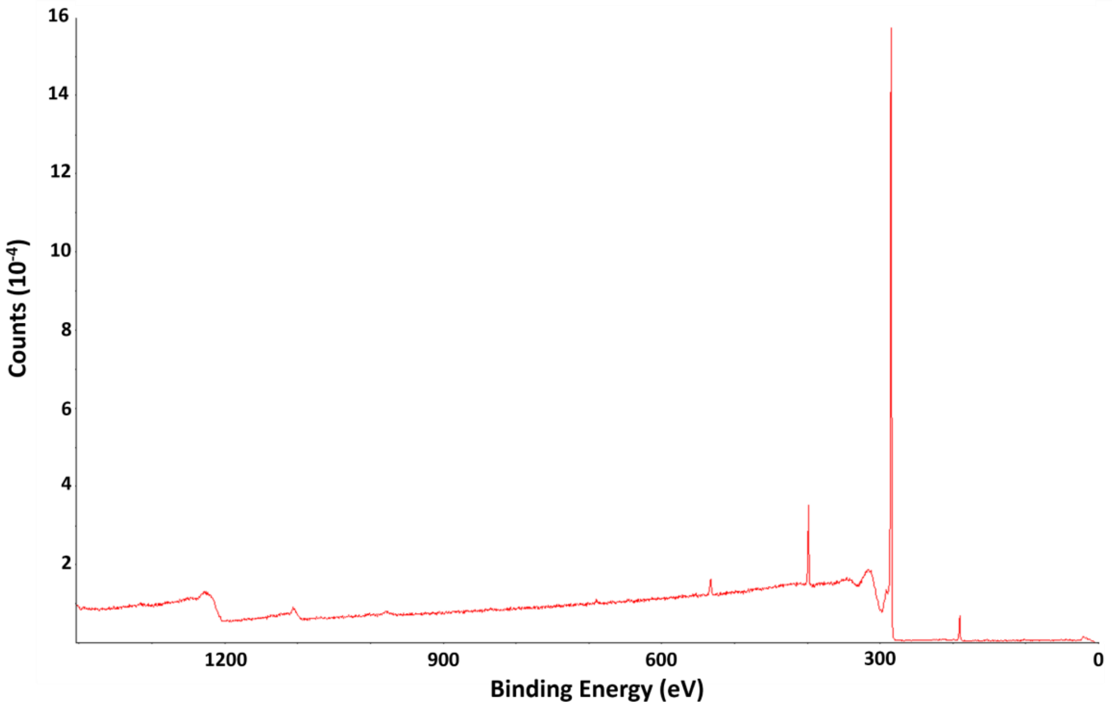

Figure A1.1 – A wide scan spectrum from the surface of sample III as defined in Chapter 4.1. Peaks in the spectrum correspond to the binding energy of electron orbitals specific to elements present near or on the surface of the sample. The peak at 284.8 eV corresponds to the 1s carbon orbital and has been used to calibrate the spectrum. The dominance of this peak in the spectrum arises due to the high prevalence of C-C bonds in the graphite surface. The remaining peaks correspond to B, N, O and Si elements present in the surface.

percentages using Kratos relative sensitivity factors (RSFs), with no applied charge correction. Data processing was carried out using 2 CASAXPS software (www.casaxps.com) with Kratos sensitivity factors (RSFs) to determine atomic percentages values from the peak areas.

Figure A1.1 exhibits a wide scan spectrum of the Sample III as defined in Chapter 4.1. Several peaks can be observed in the spectrum corresponding to the elements C, B, O, N and Si. The dominant peak observed at ~285 eV is that of the C 1s orbital in an sp2 hybrid-rich environment. A significant background response observed to the left of this peak in the spectrum is a result of inelastic scattering of electrons ejected from predominantly these C 1s orbitals.

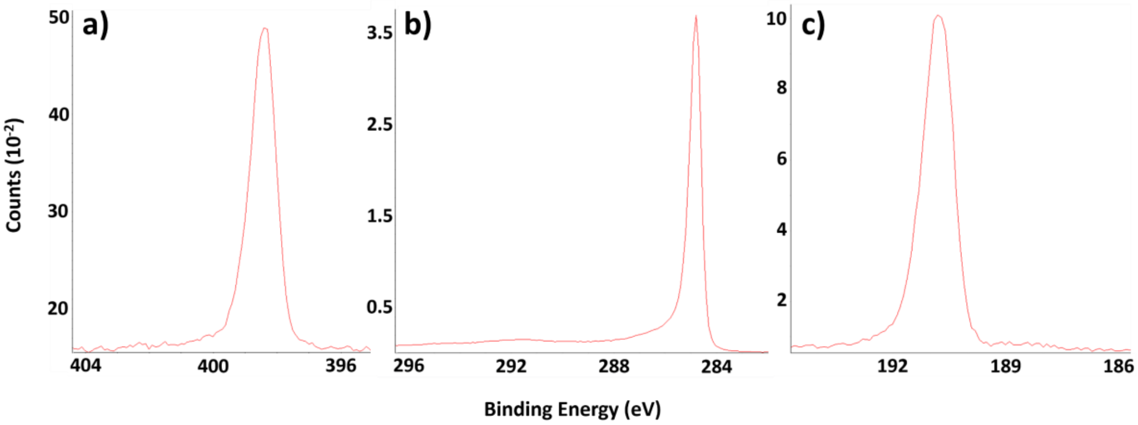

Figure A1.2 – Three intensity versus binding energy spectra are presented showing peaks corresponding to the N 1s, C 1s, and B 1s orbitals, respectively. The positions of the peaks are 398.1 eV, 284.5 eV, and 190.5 eV, respectively, though the C 1s orbital was set to this value as was expected during calibration of the spectra.

In addition to the wide scans higher resolution scans of the spectrum around N 1s, C 1s, and B 1s peaks were obtained. Three of these scans, all corresponding to sample III, are presented in Figure A1.2. The N 1s peak, as shown in A1.2 a), is observed at a position of 398.1 eV, which is expected for N in a boron-rich environment. In A1.2 c) the B 1s peak is observed at 190.5 eV, the position expected for B in an N-rich environment. As a result we concluded that the sub-monolayer of material grown on our graphite samples was boron nitride. Figure A1.2 b) covers the range of C 1s binding energies exhibited by carbon atoms bonded with sp2 and sp3 hybridized orbitals, that is 284.5 eV to 291.4 eV. A low intensity peak at 291.4 eV may be present in the data, though the intensity is such that it is inseparable from the background noise with any reasonable accuracy.

# Appendix II – List of Publications

- **Wrigley J**, et al. Epitaxy of boron nitride monolayers for graphene-based lateral heterostructures. 2D Mater. 2021 8 (3) 034001
- Thomas J, **Wrigley J**, et al. Step-Flow Growth of Graphene-Boron Nitride Lateral Heterostructures by Molecular Beam Epitaxy. *2D Mater.* 2020 7 (3) 035014
- Davies A, **Wrigley J**, et al. Lattice-Matched Epitaxial Graphene Grown on Boron Nitride. *Nano Lett.* 2018 18 (1) 498-504
- Amin S, **Wrigley J**, et al. Redox-active hierarchical assemblies of hybrid polyoxometalate nanostructures at carbon surfaces. *Inorg. Chem. Front.* 2022 9 1777-1784
- Peluso L, **Wrigley J**, et al. Sub-Molecular Resolution Imaging of P3HT:PCBM Nanostructured Films by Atomic Force Microscopy: Implications for Organic Solar Cells. *App. Nano Mater.* (Accepted for publication: 31/05/22)

# Bibliography

1. Cai Z, Liu B, Zou X, Cheng H-M. Chemical Vapor Deposition Growth and Applications of Two-Dimensional Materials and Their Heterostructures. *Chem Rev*. 2018 **118** (13) 6091–133.

2. Yang X, Yan M. Removing contaminants from transferred CVD graphene. *Nano Res*. 2020 **13** (3) 599–610.

3. Muñoz R, Gómez-Aleixandre C. Review of CVD Synthesis of Graphene. *Chem Vap Depos*. 2013 **19** (10-11–12) 297–322.

4. Chen B, Huang H, Ma X, Huang L, Zhang Z, Peng L-M. How good can CVD-grown monolayer graphene be? *Nanoscale*. 2014 **6** (24) 15255–61.

5. Gannett W, Regan W, Watanabe K, Taniguchi T, Crommie MF, Zettl A. Boron nitride substrates for high mobility chemical vapor deposited graphene. *Appl Phys Lett*. 2011 **98** (24) 242105.

6. Khan MH, Liu HK, et al. Few-atomic-layered hexagonal boron nitride: CVD growth, characterization, and applications. *Mater Today*. 2017 **20** (10) 611–28.

7. Tsai CL, Kobayashi Y, Akasaka T, Kasu M. Molecular beam epitaxial growth of hexagonal boron nitride on Ni(111) substrate. *J Cryst Growth*. 2009 **311** (10) 3054–7.

8. Laleyan DA, Mengle K, Zhao S, Wang Y, Kioupakis E, Mi Z. Effect of growth temperature on the structural and optical properties of few-layer hexagonal boron nitride by molecular beam epitaxy. *Opt Express*. 2018 **26** (18) 23031.

9. Garcia JM, Wurstbauer U, et al. Graphene growth on h-BN by molecular beam epitaxy. *Solid State Commun*. 2012 **152** (12) 975–8.

10. Zheng R, Xu Z, et al. Low-temperature growth of graphene on iron substrate by molecular beam epitaxy. *Thin Solid Films*. 2017 **627** 39–43.

11. Lin M-Y, Guo W-C, et al. Low-temperature grown graphene films by using molecular beam epitaxy. *Appl Phys Lett*. 2012 **101** (22) 221911.

12. Cheng T, Summerfield A, et al. High-Temperature Molecular Beam Epitaxy of Hexagonal Boron Nitride with High Active Nitrogen Fluxes. *Materials (Basel)*. 2018 **11** (7) 1119.

13. Cho Y-J, Summerfield A, et al. Hexagonal Boron Nitride Tunnel Barriers Grown on Graphite by High Temperature Molecular Beam Epitaxy. *Sci Rep*. 2016 **6** (1) 34474.

14. Davies A, Albar JD, et al. Lattice-Matched Epitaxial Graphene Grown on Boron Nitride. *Nano Lett*. 2018 **18** (1) 498–504.

15. Summerfield A, Davies A, et al. Strain-Engineered Graphene Grown on Hexagonal Boron Nitride by Molecular Beam Epitaxy. *Sci Rep*. 2016 **6** (1) 22440.

16. Albar JD, Summerfield A, et al. An atomic carbon source for high temperature molecular beam epitaxy of graphene. *Sci Rep*. 2017 **7** (1) 6598.

17. Spano FC. The spectral signatures of frenkel polarons in H- And J-aggregates. *Acc Chem Res*. 2010 **43** (3) 429–39.

18. Watanabe K, Taniguchi T, Kanda H. Direct-bandgap properties and evidence for ultraviolet lasing of hexagonal boron nitride single crystal. *Nat Mater*. 2004 **3** (6) 404–9.

19. Cassabois G, Valvin P, Gil B. Hexagonal boron nitride is an indirect bandgap semiconductor. *Nat Photonics*. 2016 **10** (4) 262–6.

20. Wallace PR. The Band Theory of Graphite. *Phys Rev*. 1947 **71** (9) 622–34.

21. Novoselov KS, Geim AK, et al. Electric Field Effect in Atomically Thin Carbon Films. *Science*. 2004 **306** (5696) 666–9.

22. Zhang Y, Tang T-T, et al. Direct observation of a widely tunable bandgap in bilayer graphene. *Nature*. 2009 **459** (7248) 820–3.

23. Wallbank JR, Mucha-Kruczyński M, Chen X, Fal'ko VI. Moiré superlattice effects in graphene/boron-nitride van der Waals heterostructures. *Ann Phys*. 2015 **527** (5–6) 359–76.

24. Artyukhov VI, Liu Y, Yakobson BI. Equilibrium at the edge and atomistic mechanisms of graphene growth. *Proc Natl Acad Sci*. 2012 **109** (38) 15136–40.

25. Nakada K, Fujita M, Dresselhaus G, Dresselhaus MS. Edge state in graphene ribbons: Nanometer size effect and edge shape dependence. *Phys Rev B*. 1996 **54** (24) 17954–61.

26. Wakabayashi K. Electronic and Magnetic Properties of Nanographites. *Carbon Based Magn An Overv Magn Met Free Carbon-based Compd Mater*. 2006 **59** (12) 279–304.

27. Ma F, Guo Z, Xu K, Chu PK. First-principle study of energy band structure of armchair graphene nanoribbons. *Solid State Commun*. 2012 **152** (13) 1089–93.

28. Wakabayashi K, Takane Y, Sigrist M. Perfectly Conducting Channel and Universality Crossover in Disordered Graphene Nanoribbons. *Phys Rev Lett*. 2007 **99** (3) 036601.

29. Pisani L, Chan JA, Montanari B, Harrison NM. Electronic structure and magnetic properties of graphitic ribbons. *Phys Rev B*. 2007 **75** (6) 064418.

30. Wei Z, Wang D, et al. Nanoscale Tunable Reduction of Graphene Oxide for Graphene Electronics. *Science*. 2010 **328** (5984) 1373–6.

31. Rodríguez-Manzo JA, Qi ZJ, Crook A, Ahn J-H, Johnson ATC, Drndić M. In Situ Transmission Electron Microscopy Modulation of Transport in Graphene Nanoribbons. *ACS Nano*. 2016 **10** (4) 4004–10.

32. Magda GZ, Jin X, et al. Room-temperature magnetic order on zigzag edges of narrow graphene nanoribbons. *Nature*. 2014 **514** (7524) 608–11.

33. Shinde DB, Majumder M, Pillai VK. Counter-ion Dependent, Longitudinal Unzipping of Multi-Walled Carbon Nanotubes to Highly Conductive and Transparent Graphene Nanoribbons. *Sci*

*Rep*. 2015 **4** (1) 4363.

34. Campos LC, Manfrinato VR, Sanchez-Yamagishi JD, Kong J, Jarillo-Herrero P. Anisotropic Etching and Nanoribbon Formation in Single-Layer Graphene. *Nano Lett*. 2009 **9** (7) 2600–4.

35. Gong Y, Long M, et al. Electronic transport properties of graphene nanoribbon arrays fabricated by unzipping aligned nanotubes. *Phys Rev B*. 2013 **87** (16) 165404.

36. Celis A, Nair MN, et al. Graphene nanoribbons: fabrication, properties and devices. *J Phys D Appl Phys*. 2016 **49** (14) 143001.

37. Wang D, Tian H, Yang Y, Xie D, Ren T-L, Zhang Y. Scalable and Direct Growth of Graphene Micro Ribbons on Dielectric Substrates. *Sci Rep*. 2013 **3** (1) 1348.

38. Kato T, Hatakeyama R. Site- and alignment-controlled growth of graphene nanoribbons from nickel nanobars. *Nat Nanotechnol*. 2012 **7** (10) 651–6.

39. Elias C, Valvin P, et al. Direct band-gap crossover in epitaxial monolayer boron nitride. *Nat Commun*. 2019 **10** (1) 2639.

40. Wang X, Hossain M, Wei Z, Xie L. Growth of two-dimensional materials on hexagonal boron nitride ( h -BN). *Nanotechnology*. 2019 **30** (3) 034003.

41. Han X, Lin J, Liu J, Wang N, Pan D. Effects of Hexagonal Boron Nitride Encapsulation on the Electronic Structure of Few-Layer MoS 2. *J Phys Chem C*. 2019 **123** (23) 14797–802.

42. Yankowitz M, Xue J, LeRoy BJ. Graphene on hexagonal boron nitride. *J Phys Condens Matter*. 2014 **26** (30) 303201.

43. Liu L, Park J, et al. Heteroepitaxial Growth of Two-Dimensional Hexagonal Boron Nitride Templated by Graphene Edges. *Science*. 2014 **343** (6167) 163–7.

44. Dean CR, Young AF, et al. Boron nitride substrates for high-quality graphene electronics. *Nat Nanotechnol*. 2010 **5** (10) 722–6.

45. Meric I, Dean C, Young A, Hone J, Kim P, Shepard KL. Graphene field-effect transistors based on boron nitride gate dielectrics. *In*: *2010 International Electron Devices Meeting*. *IEEE*; 2010. p. 23.2.1-23.2.4.

46. Novoselov KS, Mishchenko A, Carvalho A, Castro Neto AH. 2D materials and van der Waals heterostructures. *Science*. 2016 **353** (6298) aac9439.

47. Mayorov AS, Gorbachev R V., et al. Micrometer-Scale Ballistic Transport in Encapsulated Graphene at Room Temperature. *Nano Lett*. 2011 **11** (6) 2396–9.

48. Chen X, Wu Y, et al. High-quality sandwiched black phosphorus heterostructure and its quantum oscillations. *Nat Commun*. 2015 **6** (1) 7315.

49. Li Z, Wang Y, et al. Effect of airborne contaminants on the wettability of supported graphene and graphite. *Nat Mater*. 2013 **12** (10) 925–31.

50. Jiang HX, Lin JY. Hexagonal boron nitride for deep ultraviolet photonic devices. *Semicond Sci Technol*. 2014 **29** (8) 084003.

51. Song S-B, Yoon S, et al. Deep-ultraviolet electroluminescence and photocurrent generation in graphene/hBN/graphene heterostructures. *Nat Commun*. 2021 **12** (1) 7134.

52. Liu Y, Bhowmick S, Yakobson BI. BN White Graphene with “Colorful” Edges: The Energies and Morphology. *Nano Lett*. 2011 **11** (8) 3113–6.

53. Zhang Z, Liu Y, Yang Y, Yakobson BI. Growth Mechanism and Morphology of Hexagonal Boron Nitride. *Nano Lett*. 2016 **16** (2) 1398–403.

54. Liu Y, Dobrinsky A, Yakobson BI. Graphene Edge from Armchair to Zigzag: The Origins of Nanotube Chirality? *Phys Rev Lett*. 2010 **105** (23) 235502.

55. Yankowitz M, Xue J, et al. Emergence of superlattice Dirac points in graphene on hexagonal boron nitride. *Nat Phys*. 2012 **8** (5) 382–6.

56. Finney NR, Yankowitz M, et al. Tunable crystal symmetry in graphene–boron nitride heterostructures with coexisting moiré superlattices. *Nat Nanotechnol*. 2019 **14** (11) 1029–34.

57. Woods CR, Britnell L, et al. Commensurate–incommensurate transition in graphene on hexagonal boron nitride. *Nat Phys*. 2014 **10** (6) 451–6.

58. Linas S, Magnin Y, et al. Interplay between Raman shift and thermal expansion in graphene: Temperature-dependent measurements and analysis of substrate corrections. *Phys Rev B*. 2015 **91** (7) 075426.

59. Pletikosić I, Kralj M, et al. Dirac Cones and Minigaps for Graphene on Ir(111). *Phys Rev Lett*. 2009 **102** (5) 056808.

60. Sahu S, Rout GC. Band gap opening in graphene: a short theoretical study. *Int Nano Lett*. 2017 **7** (2) 81–9.

61. Giovannetti G, Khomyakov PA, Brocks G, Kelly PJ, van den Brink J. Substrate-induced band gap in graphene on hexagonal boron nitride: Ab initio density functional calculations. *Phys Rev B*. 2007 **76** (7) 073103.

62. Wang J, Ma F, Sun M. Graphene, hexagonal boron nitride, and their heterostructures: properties and applications. *RSC Adv*. 2017 **7** (27) 16801–22.

63. Wang J, Cao S, Sun P, Ding Y, Li Y, Ma F. Optical advantages of graphene on the boron nitride in visible and SW-NIR regions. *RSC Adv*. 2016 **6** (112) 111345–9.

64. Chen X, Qiu Y, et al. In-Plane Mosaic Potential Growth of Large-Area 2D Layered Semiconductors MoS 2 –MoSe 2 Lateral Heterostructures and Photodetector Application. *ACS Appl Mater Interfaces*. 2017 **9** (2) 1684–91.

65. Duan X, Wang C, et al. Lateral epitaxial growth of two-dimensional layered semiconductor

heterojunctions. *Nat Nanotechnol*. 2014 **9** (12) 1024–30.

66. Han GH, Rodríguez-Manzo JA, et al. Continuous Growth of Hexagonal Graphene and Boron Nitride In-Plane Heterostructures by Atmospheric Pressure Chemical Vapor Deposition. *ACS Nano*. 2013 **7** (11) 10129–38.

67. Fiori G, Betti A, Bruzzone S, Iannaccone G. Lateral graphene-hBCN heterostructures as a platform for fully two-dimensional transistors. *ACS Nano*. 2012 **6** (3) 2642–8.

68. Kim G, Ma KY, et al. Blue emission at atomically sharp 1D heterojunctions between graphene and h-BN. *Nat Commun*. 2020 **11** (1) 5359.

69. Li Q, Liu M, Zhang Y, Liu Z. Hexagonal Boron Nitride-Graphene Heterostructures: Synthesis and Interfacial Properties. *Small*. 2016 **12** (1) 32–50.

70. Sutter P, Huang Y, Sutter E. Nanoscale Integration of Two-Dimensional Materials by Lateral Heteroepitaxy. *Nano Lett*. 2014 **14** (8) 4846–51.

71. Androulidakis C, Galiotis C. Thermomechanical behaviour of hexagonal boron nitride at elevated temperatures. *2D Mater*. 2020 **7** (4) 045011.

72. Liu Z, Ma L, et al. In-plane heterostructures of graphene and hexagonal boron nitride with controlled domain sizes. *Nat Nanotechnol*. 2013 **8** (2) 119–24.

73. Zhu T, Ertekin E. Phonon transport on two-dimensional graphene/boron nitride superlattices. *Phys Rev B*. 2014 **90** (19) 195209.

74. Zhou Z, Liu H, Fan D, Cao G. Designing graphene/hexagonal boron nitride superlattice monolayer with high thermoelectric performance. 2019. arXiv: 1905.12992

75. Kınacı A, Haskins JB, Sevik C, Çağın T. Thermal conductivity of BN-C nanostructures. *Phys Rev B*. 2012 **86** (11) 115410.

76. Zhang X, Liu C, et al. High ZT 2D Thermoelectrics by Design: Strong Interlayer Vibration and

Complete Band-Extrema Alignment. *Adv Funct Mater*. 2020 **30** (22) 2001200.

77. Tang S, Wang H, et al. Precisely aligned graphene grown on hexagonal boron nitride by catalyst free chemical vapor deposition. *Sci Rep*. 2013 **3** (1) 2666.

78. Venables JA. Introduction to Surface and Thin Film Processes [Internet]. *Cambridge University Press*; 2000.

79. Paton KR, Varrla E, et al. Scalable production of large quantities of defect-free few-layer graphene by shear exfoliation in liquids. *Nat Mater*. 2014 **13** (6) 624–30.

80. Xu Y, Cao H, Xue Y, Li B, Cai W. Liquid-Phase Exfoliation of Graphene: An Overview on Exfoliation Media, Techniques, and Challenges. *Nanomaterials*. 2018 **8** (11) 942.

81. Siegel G, Grzybowski G, Prusnick T, Snure M. Single process CVD growth of hBN/Graphene heterostructures on copper thin films. *J Mater Res*. 2018 **33** (24) 4233–40.

82. Habib MR, Liang T, Yu X, Pi X, Liu Y, Xu M. A review of theoretical study of graphene chemical vapor deposition synthesis on metals: nucleation, growth, and the role of hydrogen and oxygen. *Reports Prog Phys*. 2018 **81** (3) 036501.

83. Liu W, Li H, Xu C, Khatami Y, Banerjee K. Synthesis of high-quality monolayer and bilayer graphene on copper using chemical vapor deposition. *Carbon N Y*. 2011 **49** (13) 4122–30.

84. Guermoune A, Chari T, et al. Chemical vapor deposition synthesis of graphene on copper with methanol, ethanol, and propanol precursors. *Carbon N Y*. 2011 **49** (13) 4204–10.

85. Song X, Gao J, et al. Chemical vapor deposition growth of large-scale hexagonal boron nitride with controllable orientation. *Nano Res*. 2015 **8** (10) 3164–76.

86. Li X, Cai W, et al. Large-Area Synthesis of High-Quality and Uniform Graphene Films on Copper Foils. *Science*. 2009 **324** (5932) 1312–4.

87. Arjmandi-Tash H, Kalita D, et al. Large scale graphene/h-BN heterostructures obtained by

direct CVD growth of graphene using high-yield proximity-catalytic process. *J Phys Mater*. 2018 **1** (1) 015003.

88. Uchida Y, Kawahara K, Fukamachi S, Ago H. Chemical Vapor Deposition Growth of Uniform Multilayer Hexagonal Boron Nitride Driven by Structural Transformation of a Metal Thin Film. *ACS Appl Electron Mater*. 2020 **2** (10) 3270–8.

89. Joshi S, Ecija D, et al. Boron Nitride on Cu(111): An Electronically Corrugated Monolayer. *Nano Lett*. 2012 **12** (11) 5821–8.

90. Petrović M, Hoegen MH, Meyer zu Heringdorf F-J. Equilibrium shape of single-layer hexagonal boron nitride islands on iridium. *Sci Rep*. 2019 **9** (1) 19553.

91. Kim KK, Hsu A, et al. Synthesis of Monolayer Hexagonal Boron Nitride on Cu Foil Using Chemical Vapor Deposition. *Nano Lett*. 2012 **12** (1) 161–6.

92. Chen T-A, Chuu C-P, et al. Wafer-scale single-crystal hexagonal boron nitride monolayers on Cu (111). *Nature*. 2020 **579** (7798) 219–23.

93. Liu H, You CY, et al. Synthesis of hexagonal boron nitrides by chemical vapor deposition and their use as single photon emitters. *Nano Mater Sci*. 2021 **3** (3) 291–312.

94. Wang L, Xu X, et al. Epitaxial growth of a 100-square-centimetre single-crystal hexagonal boron nitride monolayer on copper. *Nature*. 2019 **570** (7759) 91–5.

95. Yang Y, Fu Q, et al. Creating a Nanospace under an h-BN Cover for Adlayer Growth on Nickel(111). *ACS Nano*. 2015 **9** (12) 11589–98.

96. Page R, Casamento J, Cho Y, Rouvimov S, Xing HG, Jena D. Rotationally aligned hexagonal boron nitride on sapphire by high-temperature molecular beam epitaxy. *Phys Rev Mater*. 2019 **3** (6) 064001.

97. Chen X, Tan C, et al. Growth of hexagonal boron nitride films on silicon substrates by low-

pressure chemical vapor deposition. *J Mater Sci Mater Electron*. 2021 **32** (3) 3713–9.

98. Tay RY, Tsang SH, et al. Direct growth of nanocrystalline hexagonal boron nitride films on dielectric substrates. *Appl Phys Lett*. 2015 **106** (10) 101901.

99. Arai H, Inoue T, Xiang R, Maruyama S, Chiashi S. Non-catalytic heteroepitaxial growth of aligned, large-sized hexagonal boron nitride single-crystals on graphite. *Nanoscale*. 2020 **12** (18) 10399–406.

100. Farrow RFC. Molecular Beam Epitaxy - Applications to Key Materials. *William Andrew Publishing/Noyes*; 1995.

101. Pierucci D, Zribi J, et al. Van der Waals epitaxy of two-dimensional single-layer h-BN on graphite by molecular beam epitaxy: Electronic properties and band structure. *Appl Phys Lett*. 2018 **112** (25) 253102.

102. Vuong TQP, Cassabois G, et al. Deep ultraviolet emission in hexagonal boron nitride grown by high-temperature molecular beam epitaxy. *2D Mater*. 2017 **4** (2) 021023.

103. Moreau E, Godey S, et al. Graphene growth by molecular beam epitaxy on the carbon-face of SiC. *Appl Phys Lett*. 2010 **97** (24) 241907.

104. Cheng TS, Davies A, et al. High temperature MBE of graphene on sapphire and hexagonal boron nitride flakes on sapphire. *J Vac Sci Technol B*. 2016 **34** (2) 02L101.

105. Emtsev K V., Bostwick A, et al. Towards wafer-size graphene layers by atmospheric pressure graphitization of silicon carbide. *Nat Mater*. 2009 **8** (3) 203–7.

106. Charrier A, Coati A, et al. Solid-state decomposition of silicon carbide for growing ultra-thin heteroepitaxial graphite films. *J Appl Phys*. 2002 **92** (5) 2479–84.

107. de Heer WA, Berger C, et al. Large area and structured epitaxial graphene produced by confinement controlled sublimation of silicon carbide. *Proc Natl Acad Sci*. 2011 **108** (41)

16900–5.

108. Forti S, Emtsev K V., Coletti C, Zakharov AA, Riedl C, Starke U. Large-area homogeneous quasifree standing epitaxial graphene on SiC(0001): Electronic and structural characterization. *Phys Rev B*. 2011 **84** (12) 125449.

109. Whitesides GM, Mathias JP, Seto CT. Molecular Self-Assembly and Nanochemistry: a Chemical Strategy for the Synthesis of Nanostructures. *Science*. 1991 **254** (5036) 1312–9.

110. Mehra N, Jeske M, et al. Hydrogen-Bond Driven Self-Assembly of Two-Dimensional Supramolecular Melamine-Cyanuric Acid Crystals and Its Self-Alignment in Polymer Composites for Enhanced Thermal Conduction. *ACS Appl Polym Mater*. 2019 **1** (6) 1291–300.

111. Zhang H-M, Pei Z-K, et al. Preparing Self-Assembled Monolayers of Cyanuric Acid and Melamine Complex on HOPG Surfaces. *J Phys Chem C*. 2009 **113** (31) 13940–6.

112. Korolkov V V., Timokhin IG, et al. Supramolecular networks stabilise and functionalise black phosphorus. *Nat Commun*. 2017 **8** (1) 1385.

113. Huang Y, Qiao J, et al. Interaction of Black Phosphorus with Oxygen and Water. *Chem Mater*. 2016 **28** (22) 8330–9.

114. Novoselov KS, Jiang D, et al. Two-dimensional atomic crystals. *Proc Natl Acad Sci*. 2005 **102** (30) 10451–3.

115. Yi M, Shen Z. A review on mechanical exfoliation for the scalable production of graphene. *J Mater Chem A*. 2015 **3** (22) 11700–15.

116. Bohr J. Adhesive tape exfoliation: Why it works for graphene. *EPL (Europhysics Lett*. 2015 **109** (5) 58004.

117. Wang X, Zhao M, Nolte DD. Optical contrast and clarity of graphene on an arbitrary substrate. *Appl Phys Lett*. 2009 **95** (8) 081102.

118. Ahn Y, Kim J, Ganorkar S, Kim Y-H, Kim S-I. Thermal annealing of graphene to remove polymer residues. *Mater Express*. 2016 **6** (1) 69–76.

119. Valeur B, Berberan-Santos MN. Molecular Fluorescence [Internet]. 2nd ed. Weinheim, Germany: *Wiley*; 2012.

120. Pelant I, Valenta J. Luminescence Spectroscopy of Semiconductors [Internet]. *Oxford University Press*; 2012.

121. Lakowitz JR. Principles of Fluorescence Spectroscopy. 2nd ed. New York: *Springer Science and Business Media LLC*; 1999.

122. Chen Z, Berciaud S, Nuckolls C, Heinz TF, Brus LE. Energy Transfer from Individual Semiconductor Nanocrystals to Graphene. *ACS Nano*. 2010 **4** (5) 2964–8.

123. Persson BNJ, Lang ND. Electron-hole-pair quenching of excited states near a metal. *Phys Rev B*. 1982 **26** (10) 5409–15.

124. Vandenabeele P. Practical Raman Spectroscopy : An Introduction. 1st ed. Ghent: *John Wiley & Sons, Ltd*; 2013.

125. Kawashima Y, Katagiri G. Fundamentals, overtones, and combinations in the Raman spectrum of graphite. *Phys Rev B*. 1995 **52** (14) 10053–9.

126. Ferrari AC, Basko DM. Raman spectroscopy as a versatile tool for studying the properties of graphene. *Nat Nanotechnol*. 2013 **8** (4) 235–46.

127. Malard LM, Pimenta MA, Dresselhaus G, Dresselhaus MS. Raman spectroscopy in graphene. *Phys Rep*. 2009 **473** (5–6) 51–87.

128. Bayle M, Reckinger N, et al. Determining the number of layers in few-layer graphene by combining Raman spectroscopy and optical contrast. *J Raman Spectrosc*. 2018 **49** (1) 36–45.

129. Das A, Pisana S, et al. Monitoring dopants by Raman scattering in an electrochemically top-

gated graphene transistor. *Nat Nanotechnol*. 2008 **3** (4) 210–5.

130. Frank O, Tsoukleri G, et al. Development of a universal stress sensor for graphene and carbon fibres. *Nat Commun*. 2011 **2** (1).

131. Babich IL. Raman spectrum of hexagonal boron nitride. *Theor Exp Chem*. 1974 **8** (5) 594–5.

132. Yang L, Champness NR. Chapter 1. Surface Self-assembly of Functional Supramolecular Networks. *In*: *Monographs in Supramolecular Chemistry*. 2017. p. 1–36.

133. Bombis C, Kalashnyk N, Xu W, Laegsgaard E, Besenbacher F, Linderoth TR. Hydrogen-Bonded Molecular Networks of Melamine and Cyanuric Acid on Thin Films of NaCl on Au(111). *Small*. 2009 **5** (19) 2177–82.

134. Magonov SN, Elings V, Whangbo M-H. Phase imaging and stiffness in tapping-mode atomic force microscopy. *Surf Sci*. 1997 **375** (2–3) L385–91.

135. García R, San Paulo A. Attractive and repulsive tip-sample interaction regimes in tapping-mode atomic force microscopy. *Phys Rev B*. 1999 **60** (7) 4961–7.

136. Nečas D, Klapetek P. Gwyddion: an open-source software for SPM data analysis. *Open Phys*. 2012 **10** (1) 181–8.

137. Lai C-Y, Santos S, Chiesa M. General interpretation and theory of apparent height in dynamic atomic force microscopy. *RSC Adv*. 2015 **5** (97) 80069–75.

138. Santos S, Barcons V, Christenson HK, Font J, Thomson NH. The Intrinsic Resolution Limit in the Atomic Force Microscope: Implications for Heights of Nano-Scale Features. Gruverman A, editor. *PLoS One*. 2011 **6** (8) e23821.

139. Nakhaie S, Wofford JM, et al. Synthesis of atomically thin hexagonal boron nitride films on nickel foils by molecular beam epitaxy. *Appl Phys Lett*. 2015 **106** (21) 213108.

140. Celis A, Nair MN, et al. Graphene nanoribbons: fabrication, properties and devices. *J Phys D*

*Appl Phys*. 2016 **49** (14) 143001.

141. Wang Y, Nieman R, Minton TK, Guo H. Insights into adsorption, diffusion, and reactions of atomic nitrogen on a highly oriented pyrolytic graphite surface. *J Chem Phys*. 2021 **154** (7) 074708.

142. Liu J, Wang C, Liang T, Lai W. Interaction of boron with graphite: A van der Waals density functional study. *Appl Surf Sci*. 2016 **379** 402–10.

143. Nakada K, Ishii A. Migration of adatom adsorption on graphene using DFT calculation. *Solid State Commun*. 2011 **151** (1) 13–6.

144. Zhong X, Yap YK, Pandey R, Karna SP. First-principles study of strain-induced modulation of energy gaps of graphene/BN and BN bilayers. *Phys Rev B*. 2011 **83** (19) 193403.

145. Liu Y, Zou X, Yakobson BI. Dislocations and Grain Boundaries in Two-Dimensional Boron Nitride. *ACS Nano*. 2012 **6** (8) 7053–8.

146. Acik M, Chabal YJ. Nature of Graphene Edges: A Review. *Jpn J Appl Phys*. 2011 **50** (7) 070101.

147. Cosma DA, Wallbank JR, Cheianov V, Fal'Ko VI. Moiré pattern as a magnifying glass for strain and dislocations in van der Waals heterostructures. *Faraday Discuss*. 2014 **173** 137–43.

148. Rajasekaran G, Narayanan P, Parashar A. Effect of Point and Line Defects on Mechanical and Thermal Properties of Graphene: A Review. *Crit Rev Solid State Mater Sci*. 2016 **41** (1) 47–71.

149. Tuinstra F, Koenig JL. Raman Spectrum of Graphite. *J Chem Phys*. 1970 **53** (3) 1126–30.

150. Lucchese MM, Stavale F, et al. Quantifying ion-induced defects and Raman relaxation length in graphene. *Carbon N Y*. 2010 **48** (5) 1592–7.

151. Hao Y, Wang Y, et al. Probing Layer Number and Stacking Order of Few-Layer Graphene by Raman Spectroscopy. *Small*. 2010 **6** (2) 195–200.

152. Li J, Wang C, et al. Friction Coefficients Derived from Apparent Height Variations in Contact Mode Atomic Force Microscopy Images. *Langmuir*. 1999 **15** (22) 7662–9.

153. Moreno-Herrero F, Colchero J, Baró AM. DNA height in scanning force microscopy. *Ultramicroscopy*. 2003 **96** (2) 167–74.

154. Verdaguer A, Santos S, Sauthier G, Segura JJ, Chiesa M, Fraxedas J. Water-mediated height artifacts in dynamic atomic force microscopy. *Phys Chem Chem Phys*. 2012 **14** (46) 16080.

155. Lu J, Zhang K, et al. Order–disorder transition in a two-dimensional boron–carbon–nitride alloy. *Nat Commun*. 2013 **4** (1) 2681.

156. Radovic LR, Bockrath B. On the Chemical Nature of Graphene Edges: Origin of Stability and Potential for Magnetism in Carbon Materials. *J Am Chem Soc*. 2005 **127** (16) 5917–27.

157. Kimouche A, Ervasti MM, et al. Ultra-narrow metallic armchair graphene nanoribbons. *Nat Commun*. 2015 **6** (1) 10177.

158. Makino R, Mizuno S, Kageshima H, Hibino H. Controlled CVD growth of lateral and vertical graphene/h-BN heterostructures. *Appl Phys Express*. 2020 **13** (6) 065007.

159. Wei W, Pan J, et al. Dynamic observation of in-plane h-BN/graphene heterostructures growth on Ni(111). *Nano Res*. 2020 **13** (7) 1789–94.

160. Ci L, Song L, et al. Atomic layers of hybridized boron nitride and graphene domains. *Nat Mater*. 2010 **9** (5) 430–5.

161. Levendorf MP, Kim C-J, et al. Graphene and boron nitride lateral heterostructures for atomically thin circuitry. *Nature*. 2012 **488** (7413) 627–32.

162. Liu M, Li Y, et al. Quasi-Freestanding Monolayer Heterostructure of Graphene and Hexagonal Boron Nitride on Ir(111) with a Zigzag Boundary. *Nano Lett*. 2014 **14** (11) 6342–7.

163. Kim SM, Hsu A, et al. Synthesis of patched or stacked graphene and hBN flakes: A route to

hybrid structure discovery. *Nano Lett*. 2013 **13** (3) 933–41.

164. Petrović M, Horn-von Hoegen M, Meyer zu Heringdorf F-J. Lateral heterostructures of hexagonal boron nitride and graphene: BCN alloy formation and microstructuring mechanism. *Appl Surf Sci*. 2018 **455** (April) 1086–94.

165. Roy B, Bairi P, Nandi AK. Supramolecular assembly of melamine and its derivatives: nanostructures to functional materials. *RSC Adv*. 2014 **4** (4) 1708–34.

166. Huie JC. Guided molecular self-assembly: a review of recent efforts. *Smart Mater Struct*. 2003 **12** (2) 264–71.

167. Korolkov V V., Baldoni M, Watanabe K, Taniguchi T, Besley E, Beton PH. Supramolecular heterostructures formed by sequential epitaxial deposition of two-dimensional hydrogen-bonded arrays. *Nat Chem*. 2017 **9** (12) 1191–7.

168. Kasry A, Ardakani AA, Tulevski GS, Menges B, Copel M, Vyklicky L. Highly Efficient Fluorescence Quenching with Graphene. *J Phys Chem C*. 2012 **116** (4) 2858–62.

169. Kerfoot J. The growth and fluorescence of organic monolayers and heterostructures, PhD Thesis, *University of Nottingham,* Nottingham, UK 2018 (July). http://eprints.nottingham.ac.uk/50673/

170. Kerfoot J, Korolkov V V., et al. Substrate-induced shifts and screening in the fluorescence spectra of supramolecular adsorbed organic monolayers. *J Chem Phys*. 2018 **149** (5).

171. Kozbial A, Zhou F, Li Z, Liu H, Li L. Are Graphitic Surfaces Hydrophobic? *Acc Chem Res*. 2016 **49** (12) 2765–73.

172. Ohto T, Tada H, Nagata Y. Structure and dynamics of water at water–graphene and water–hexagonal boron-nitride sheet interfaces revealed by ab initio sum-frequency generation spectroscopy. *Phys Chem Chem Phys*. 2018 **20** (18) 12979–85.

173. Kozbial A, Li Z, et al. Understanding the intrinsic water wettability of graphite. *Carbon N Y*. 2014 **74** 218–25.